

EVALUATION OF CRUSHING IN GRANULAR MATERIALS USING THE DISCRETE ELEMENT  
METHOD AND FRACTAL THEORY

by

Sebastian Lobo-Guerrero

B.S. in Civil Engineering, Universidad de Los Andes, 2002

M.S. in Civil Engineering, University of Pittsburgh, 2002

Submitted to the Graduate Faculty of  
the School of Engineering in partial fulfillment  
of the requirements for the degree of  
Doctor of Philosophy

University of Pittsburgh

2006

UNIVERSITY OF PITTSBURGH  
SCHOOL OF ENGINEERING

This dissertation was presented  
by

Sebastian Lobo-Guerrero

It was defended on  
February 21st, 2006  
and approved by

Jeen-Shang Lin, Associate Professor, Department of Civil and Environmental Engineering

Ian Nettleship, Associate Professor, Department of Materials Science and Engineering

Julie M. Vandebossche, Assistant Professor, Department of Civil and Environmental Engineering

Dissertation Director: Luis E. Vallejo, Professor, Department of Civil and Environmental Engineering

## ABSTRACT

### EVALUATION OF CRUSHING IN GRANULAR MATERIALS USING THE DISCRETE ELEMENT METHOD AND FRACTAL THEORY

Sebastian Lobo-Guerrero, PhD

University of Pittsburgh, 2006

Granular materials forming part of embankments, foundations, pavement structures, and rail track structures are subjected to both static and dynamic loads. As a result of these loads particle breakage may occur. Particle breakage causes settlements and a reduction in the hydraulic conductivity of the granular material. Moreover, the elastic modulus and the shear strength of the granular material are also negatively affected. Granular crushing is a detrimental phenomenon that deserves to be studied in order to understand its causes, consequences, and ways to avoid it. Laboratory tests conducted on a weak granular material (sugar) and computer simulations (in the form of the Discrete Element Method, DEM) were used to visualize, analyze, and understand the evolution of crushing in granular materials. The original DEM was modified to include the possibility of particle fragmentation. A tensile failure criterion developed by the author was programmed and incorporated into a commercial DEM code (PFC<sup>2D</sup>). The breakage model was also used to study the evolution of crushing in practical geotechnical applications. Fractal theory was used to quantify the amount of crushing produced under different conditions of stress and strain. In particular, the fragmentation fractal dimension was used to describe the changes on the grain size distribution of the analyzed materials.

## TABLE OF CONTENTS

1.0	INTRODUCTION .....	1
2.0	PREVIOUS RESEARCH ON GRANULAR CRUSHING .....	3
2.1	FACTORS INFLUENCING CRUSHING .....	3
2.2	CONSEQUENCES OF CRUSHING .....	5
2.3	CURRENT METHODS FOR MEASURING CRUSHING .....	7
2.4	STATISTICS OF PARTICLE TENSILE STRENGTH.....	9
2.4.1	Calculating Weibull statistics for specimens of similar size.....	11
2.4.2	Calculating Weibull statistics for specimens of different sizes .....	12
2.4.3	Significance and typical values of the Weibull modulus “m” .....	13
2.4.4	An example of the application of Weibull statistics .....	13
3.0	LABORATORY TESTS USING A WEAK GRANULAR MATERIAL.....	18
3.1	SUGAR AS A WEAK GRANULAR MATERIAL.....	18
3.2	CONFINED UNIAXIAL COMPRESSION TESTS.....	19
3.2.1	Void ratio .....	19
3.2.2	Sieve analyses .....	20
3.2.3	Elastic modulus.....	23
3.3	DIRECT SHEAR TESTS.....	24
3.3.1	Mobilized friction coefficient .....	24
3.3.2	Photographic analysis .....	25
3.3.3	Sieve analyses .....	27
3.3.4	Volumetric changes .....	29

3.4	RING SHEAR TESTS .....	30
3.4.1	Mobilized friction coefficient .....	30
3.4.2	The evolution of crushing .....	31
3.5	CONCLUSIONS ABOUT THE LABORATORY RESULTS .....	34
4.0	DEM AND PARTICLE BREAKAGE CRITERION .....	36
4.1	THE DISCRETE ELEMENT METHOD .....	36
4.2	THE ROLE OF PARTICLE ROTATION: A DEM LIMITATION .....	39
4.3	ALLOWING PARTICLE BREAKAGE.....	40
4.3.1	Previous work .....	40
4.3.2	Breakage criterion.....	41
4.3.3	Fragmentation .....	43
4.3.4	Applying the breakage criterion.....	45
5.0	DEM SIMULATIONS OF THE LABORATORY TESTS.....	46
5.1	CONFINED UNIAXIAL COMPRESSION TEST .....	46
5.1.1	Configuration of the sample .....	46
5.1.2	Evolution of crushing: void ratio.....	47
5.1.3	Evolution of crushing: particle size distribution .....	50
5.1.4	Evolution of crushing: experimental validation of the concentration of crushing .....	51
5.2	DIRECT SHEAR TESTS .....	54
5.2.1	Configuration of the samples and sequence of the simulated direct shear tests .....	54
5.2.2	Crushing and porosity evolution .....	55
5.2.3	Evolution of the grain size distribution.....	59
5.2.4	Shear strength .....	60
5.3	RING SHEAR TESTS .....	63
5.3.1	Configuration of the samples .....	64

5.3.2	Evolution of porosity and friction coefficient of the sample composed by unbreakable particles.....	65
5.3.3	Evolution of crushing, porosity, and friction coefficient: sample composed by crushable particles, vertical force= $1 \times 10^5 \text{N}$ .....	67
5.3.4	Evolution of crushing, porosity, and shear strength: sample composed by crushable particles, vertical force= $1.5 \times 10^5 \text{N}$ .....	71
5.4	BIAXIAL TESTS .....	74
5.4.1	Configuration of the samples and sequence of the simulated biaxial tests .....	74
5.4.2	Isotropic compression .....	75
5.4.3	Shearing at $\sigma_3 = 1 \times 10^5 \text{ Pa}$ .....	78
5.4.4	Shearing at $\sigma_3 = 5 \times 10^5 \text{ Pa}$ .....	78
5.4.5	Shearing at $\sigma_3 = 10 \times 10^5 \text{ Pa}$ .....	83
5.4.6	Change on the internal friction angle.....	86
5.5	CONCLUSIONS FROM THE SIMULATED LABORATORY TESTS .....	87
6.0	PRACTICAL APPLICATIONS .....	90
6.1	DEM ANALYSIS OF CRUSHING AROUND DRIVEN PILES IN GRANULAR MATERIALS .....	90
6.1.1	Previous work .....	91
6.1.2	Configuration of the sample.....	91
6.1.3	Results using an unbreakable granular material .....	92
6.1.4	Results using a crushable granular material.....	95
6.1.5	Significance of the application.....	97
6.2	EFFECT OF CRUSHING ON THE BEARING CAPACITY OF FOOTINGS .....	98
6.2.1	Previous work .....	98
6.2.2	Configuration of the simulated material and testing procedure .....	99
6.2.3	Results of the simulation without crushing.....	101
6.2.4	Results of the simulation considering crushing .....	106

6.2.5	Discussion of the results and comparison with the theoretical bearing capacity equation.....	110
6.2.6	Significance of the application.....	112
6.3	ANALYSIS OF RAILTRACK BALLAST DEGRADATION DURING CYCLIC LOADING.....	112
6.3.1	Selection of railtrack ballast.....	113
6.3.2	Application of DEM to simulate ballast degradation during cyclic loading.....	114
6.3.3	Configuration of the simulated material and testing procedure .....	115
6.3.4	Results of the simulation without crushing.....	116
6.3.5	Results of the simulation considering crushing .....	119
6.3.6	Discussion of the results .....	123
6.4	DEGRADATION OF A GRANULAR BASE UNDER A FLEXIBLE PAVEMENT.....	124
6.4.1	Typical structure of a flexible pavement .....	124
6.4.2	Simulating a pavement section .....	125
6.4.3	Simulating the construction process and the application of the moving wheel .....	126
6.4.4	Results of the simulation.....	127
6.4.5	Application of the findings and limitations of the DEM simulation.....	132
7.0	CONCLUSIONS .....	133
	BIBLIOGRAPHY .....	134

## LIST OF FIGURES

Figure 2.1. Effect of crushing on the void ratio vs applied vertical stress curve .....	6
Figure 2.2. Different specimens coming from the same material (Modified from Ashby and Jones, 1998) .....	10
Figure 2.3 Calculation of the Weibull modulus: (a) based on survival probabilities, (b) based on a size- strength relationship. ....	12
Figure 2.4. Schematic description of the point load test .....	14
Figure 2.5. Characteristic tensile strength vs. specimen size .....	15
Figure 2.6. Photographs of the tested materials. ....	16
Figure 2.7. Survival probabilities: comparison between calculated and predicted values.....	17
Figure 3.1. Natural angle of repose of the sugar .....	19
Figure 3.2. Vertical stress vs. void ratio, confined uniaxial compression tests. ....	20
Figure 3.3 Particle size distributions after the compression tests. ....	21
Figure 3.4 Fragmentation fractal dimension, $\sigma_v = 1548$ kPa .....	22
Figure 3.5 Applied vertical stress vs fragmentation fractal dimension.....	22
Figure 3.6 Vertical stress, $\sigma_v$ , versus Young's Modulus of Elasticity, E.....	23
Figure 3.7 Horizontal deformation vs. friction coefficient .....	25
Figure 3.8 Samples subjected to an average vertical stress of 110 kPa. ....	26
Figure 3.9 Samples subjected to an average vertical stress of 225 kPa. ....	26
Figure 3.10 Particle size distribution, $\sigma_v = 110$ kPa. ....	27
Figure 3.11 Particle size distribution, $\sigma_v = 200$ kPa. ....	27
Figure 3.12 Particle size distribution, $\sigma_v = 225$ kPa. ....	28

Figure 3.13 Vertical deformation vs. horizontal deformation $\sigma_v=225\text{kPa}$ .....	29
Figure 3.14 Friction coefficient vs. horizontal deformation. ....	31
Figure 3.15. Particle size distribution of the samples after one revolution in the ring shear .....	31
Figure 3.16. Particle size distribution of the laboratory samples at $\sigma_v=296\text{ kPa}$ . ....	32
Figure 3.17 Fragmentation fractal dimensions of samples at $\sigma_v=296\text{ kPa}$ .....	33
Figure 3.18 Photograph of particles from the laboratory samples, $\sigma_v=296\text{ kPa}$ .....	34
Figure 4.1 Summary of the constitutive model of PFC <sup>2D</sup> (Figure from the User's guide volume of the Itasca PFC <sup>2D</sup> manuals) .....	38
Figure 4.2 Equivalent load configuration and idealization of the induced tensile stress .....	42
Figure 4.3 Fragments produced after a tensile failure of a real aggregate, a glass bead, and the idealized material.....	44
Figure 5.1 Crushing evolution, confined uniaxial compression test.....	49
Figure 5.2 Details of the pore structure at different values of vertical force .....	50
Figure 5.3 Evolution of the particle size distribution, confined uniaxial compression test .....	51
Figure 5.4 Void ratio vs applied vertical stress, sand ...(tests conducted by Vesga, L.F. at the University of Pittsburgh) .....	52
Figure 5.5 Layered analysis, sand, ...(tests conducted by Vesga, L.F. at the University of Pittsburgh).....	53
Figure 5.6 Porosity and crushing evolution of the simulated granular material (vertical force = $1.6 \times 10^4\text{ N}$ ) .....	56
Figure 5.7 Porosity and crushing evolution of the simulated granular material (vertical force = $3 \times 10^4\text{ N}$ ) .....	57
Figure 5.8 Evolution of the particle size distribution during the simulated direct shear test.....	60
Figure 5.9 Induced horizontal displacement vs. applied shear stress, vertical force= $1.6 \times 10^4\text{ N}$ .....	61
Figure 5.10 Induced horizontal displacement vs. applied shear stress, vertical force= $3 \times 10^4\text{ N}$ .....	62
Figure 5.11 Sample composed by unbreakable particles .....	66
Figure 5.12 Sample composed by breakable particles, vertical force= $1 \times 10^5\text{ N}$ .....	69
Figure 5.13 Evolution of the particle size distribution, vertical force: $1 \times 10^5\text{ N}$ .....	70
Figure 5.14 Evolution of the fragmentation fractal dimension, vertical force: $1 \times 10^5\text{ N}$ .....	70

Figure 5.15 Sample composed by breakable particles, vertical force= $1.5 \times 10^5 \text{N}$ .....	72
Figure 5.16 Evolution of the particle size distribution, vertical force: $1.5 \times 10^5 \text{N}$ .....	73
Figure 5.17 Evolution of the fragmentation fractal dimension, vertical force: $1.5 \times 10^5 \text{N}$ .....	73
Figure 5.18 Isotropic compression of the original sample .....	77
Figure 5.19 Evolution of granular crushing during the application of the deviator stress at $\sigma_3=5 \times 10^5 \text{ Pa}$ .	80
Figure 5.20 Details of the sample subjected to shearing at $\sigma_3=5 \times 10^5 \text{ Pa}$ .....	81
Figure 5.21 Evolution of the grain size distribution of the sample subjected to shearing at $\sigma_3=5 \times 10^5 \text{ Pa}$ .	82
Figure 5.22 Evolution of granular crushing during the application of the deviator stress at $\sigma_3=10 \times 10^5 \text{ Pa}$ .....	84
Figure 5.23 Details of the sample subjected to shearing at $\sigma_3=10 \times 10^5 \text{ Pa}$ .....	85
Figure 5.24 Evolution of the grain size distribution of the sample subjected to shearing at $\sigma_3=10 \times 10^5 \text{ Pa}$ . .....	86
Figure 5.25 Mohr circles and failure envelopes for each test .....	87
Figure 6.1 Penetration resistance, unbreakable granular material .....	94
Figure 6.2 Penetration resistance, crushable granular material.....	96
Figure 6.3. Crushed material at the tip and sides of pile at full penetration in Fig.6.2 .....	97
Figure 6.4. Initial configuration of the samples .....	100
Figure 6.5. Vertical displacement of the footing vs. applied vertical force; no crushing allowed.....	102
Figure 6.6 Uncrushable sample at the moment of failure, $dv=0.8\text{cm}$ . .....	104
Figure 6.7 Uncrushable sample at $dv=1.5\text{cm}$ .....	105
Figure 6.8 Vertical displacement of the footing vs. applied vertical force; crushing allowed.....	107
Figure 6.9 Velocity vectors of the particles at different moments of the simulation; crushing allowed...	109
Figure 6.10. Contact forces between particles; crushing allowed.....	110
Figure 6.11. Load cycles, uncrushable ballast .....	117
Figure 6.12. Permanent deformation of the ballast bed vs number of applied cycles, uncrushable ballast .....	118
Figure 6.13. Development of force chains, uncrushable ballast .....	119

Figure 6.14. Load cycles, crushable ballast .....	120
Figure 6.15 Permanent deformation of the ballast bed vs. number of applied cycles, crushable ballast..	121
Figure 6.16 Details of the unloaded sample after 200 cycles, crushable ballast.....	122
Figure 6.17 Forces developed inside the asphalt concrete layer and the granular base layer .....	128
Figure 6.18 Snap shots of the pavement section being subjected to a different number of completed passes of a moving wheel .....	130
Figure 6.19 Details of the base layer at N=16.....	131

## **PREFACE**

I would like to express my sincere appreciation to my advisor Dr. Luis E. Vallejo for his guidance and assistance at the different stages of this investigation. Professor Vallejo has been more than an academic advisor, he has been a mentor and a very good friend. The work described herein was supported by grant No.CMS-0301815 from the National Science Foundation, Washington, D.C. This support is gratefully acknowledged. I would like to thank all the people that work parallel to me at the Geotechnical laboratory of the University of Pittsburgh. Special thanks to Dr. Zamri Chik, Dr. Luis F. Vesga, Mr. Yohiro Yoshida, Mr. Kevin Hammer, and Mr. Dan Bliss.

## 1.0 INTRODUCTION

Granular materials forming part of embankments, foundations, pavement structures, and rail track structures are subjected to both static and dynamic loads. As a result of these loads particle breakage in the form of abrasion and total fragmentation may occur. Particle breakage causes settlements and a reduction in the hydraulic conductivity of the granular material. Moreover, the elastic properties and the shear strength could also be negatively affected. Consequently, granular crushing is a detrimental phenomenon that deserves to be studied in order to understand its causes, consequences, and ways to avoid it.

This research project had two main objectives: (a) to understand the effects of crushing on the behavior of granular materials, and (b) to visualize and analyze the evolution of crushing using the Discrete Element Method (DEM). This second objective was divided into three specific objectives: (i) to develop a particle breakage model, (ii) to simulate standard laboratory tests, and (iii) to simulate geotechnical situations where particle crushing is known to cause problems.

This dissertation is organized as follows: Chapter 2 is a literature review addressing four main aspects: factors influencing particle crushing, consequences of particle crushing, current methods for measuring crushing, and statistics of particle strength. Chapter 3 presents the results of laboratory tests developed by the author in order to understand how crushing affects the behavior of granular materials. Results of confined uniaxial compression tests, direct shear tests, and ring shear tests on a weak granular material (sugar) are presented. Chapter 4 introduces the Discrete Element Method and a particle breakage model developed by the author. Chapter 5 presents DEM simulations of the laboratory tests presented in Chapter 3 using the implemented particle breakage model. Chapter 6 presents some practical applications of the proposed model such as the analysis of particle crushing around driven piles in granular materials,

underneath shallow foundations, at the granular layers of pavement structures, and at the ballast bed of rail tracks. Finally, some conclusions are presented in Chapter 7.

## **2.0 PREVIOUS RESEARCH ON GRANULAR CRUSHING**

### **2.1 FACTORS INFLUENCING CRUSHING**

Based on laboratory tests, some general factors have been associated with the occurrence of crushing in granular materials:

a. Particle strength

Crushing is related to the strength of the particles [Hardin, 1985], [Lade et al., 1996], [MacDowell and Bolton, 1998], [Fedda, 2002].

b. Particle size

A uniform granular material composed by big particles presents more crushing than one composed by smaller particles of the same material [Lee and Farhoomand, 1967], [Hardin, 1985], [Hagerty et al., 1993], [Lade et al., 1996], [MacDowell and Bolton, 1998], [McDowell 2002]. Hardin [1985] and Lade et al. [1996] explain this based on the fact that bigger particles have a higher probability of having defects.

c. Angularity

Angular particles exhibit more crushing than rounded particles [Lee and Farhoomand, 1967], [Hagerty et al., 1993], [Lade et al., 1996]. Lade et al. [1996] explain this based on the fact that angular particles concentrate stresses.

d. Soil gradation

Uniform soils exhibit more crushing than well graded soils with the same maximum particle size [Lee and Farhoomand, 1967], [Lade et al., 1996], [Nakata et al., 2001a]. Lade et al. [1996] explain this based on the fact that increasing the number of contacts (the coordination number) around a particle causes a decrease on the average contact stress.

e. Density of the granular material

Crushing starts under a smaller compressive stress if the granular material is in a loose state rather than in a dense state [Hagerty et al., 1993], [MacDowell and Bolton, 1998], [Nakata et al., 2001b]. MacDowell and Bolton [1998] state that this is a consequence of having a granular material with a smaller average coordination number.

f. The degree of confinement of the particles

By using computer simulations and laboratory tests, Tsoungui et al. [1999] found that large grains surrounded by small grains in a granular media do not easily break since the small grains confine the large ones producing an hydrostatic state of stresses. The hydrostatic stress environment in the large particle increases with the crushing of the smaller particles since more surrounding particles are generated. Similar observations were reported by Mandl et al. [1977] when simulating cataclastic shearing of granular materials.

g. Creep

Under a constant load crushing continues with time in the form of creep [Terzaghi and Peck, 1948], [Lee and Farhoomand, 1967], [Lade et al., 1996], [Leung et al., 1996], [Takei et al., 2001], [Feda, 2002], [MacDowell and Khan, 2003]. Experiments conducted by Feda [2002], and MacDowell and Khan

[2003] have shown that the coefficient of secondary compression, which is referred as the creep coefficient, is stress dependent.

#### h. Compression and shearing

Bishop [1966] found that particle breakage occurs during the consolidation stages and the shearing stages of triaxial tests at high pressures. He noted that more crushing was produced during the shearing stage than during the consolidation stage. Mandl et al. [1977] found that the amount of crushing in samples subjected to a pure compressive stress was significantly smaller than the amount produced if the samples were also sheared.

#### i. Water effect

Crushing is accelerated by the addition of water to the crushable material [Lee and Farhoomand, 1967], [Miura and Yamanouchi, 1975], [Chavez and Alonso, 2003]. There are many possible explanations to this phenomenon such as softening of the mineral bonds due to wetting, expansion of the constitutive materials of the aggregates, and reduction in suction inside cracks due to saturation.

Most of the reported results were obtained using triaxial compression and uniaxial compression machines, mainly on glass beads, rock aggregates, and sands.

## **2.2 CONSEQUENCES OF CRUSHING**

Granular crushing changes the engineering properties of a granular material principally in three ways:

## 1. Reducing the volume of voids

Granular crushing produces a reduction in the volume of voids and the bulk volume of granular materials [Vallejo, 2003]. Previous research has shown that in granular materials a clear relationship exist between the void ratio of the material ( $e=V_v/V_s$ ) and the applied vertical stress in confined uniaxial tests [Terzaghi, 1948], [Hagerty et al., 1993], [Pestana and Whittle, 1995], [MacDowell and Bolton, 1998], [Nakata et al., 2001a] and isotropic compression tests [Coop, 1990], [Cheng et al., 2003]. Two different regions can be distinguished on a curve relating the applied stress and the void ratio of the granular material (  $\log(\sigma')$  vs  $e$  curve). Fig. 2.1 shows these two regions. The first region is mainly controlled by particle rearrangement and elastic deformation while the second region is mainly controlled by particle crushing, particle rearrangement, and elastic deformation. In this way, engineering parameters such as the compression index,  $C_c$ , are affected by the occurrence of crushing.

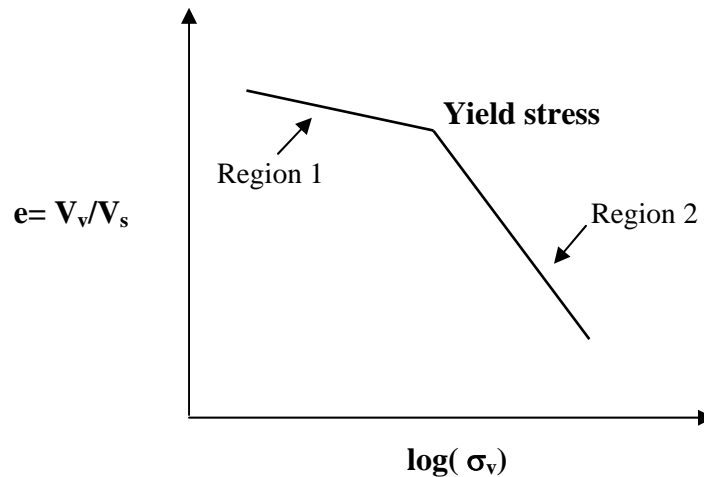


Figure 2.1. Effect of crushing on the void ratio vs applied vertical stress curve

## 2. Reducing the hydraulic conductivity

A reduction on the volume of voids causes a reduction on the hydraulic conductivity. Vallejo [2003] has shown that the hydraulic conductivity of a granular soil could be strongly reduced as a consequence of crushing. A reduction on the hydraulic conductivity is critical for a granular soil since its drainage capacity is affected. For example granular bases on pavement structures are designed to serve

different purposes, one of those is to drain the water out from the pavement structure, but if the original hydraulic conductivity is reduced this layer would not be able to perform this task. It is well known the serious consequences that are triggered on the pavement structure if water is retained inside, such as excessive deformation due to the reduction in the materials strength, stripping of the asphalt binder, etc.

### 3. Reducing the angle of shearing resistance

Granular materials undergoing crushing exhibit a non-linear Mohr-Coulomb failure envelope if the envelope is constructed with the peak values of shear resistance. Therefore, the angle of shearing resistance decreases as a consequence of particle crushing [Bishop, 1966], [Miura and O-Hara, 1979], [Bolton, 1986], [Fedda, 2002]. On the other hand, ring shear tests on carbonate sand presented by Coop et al. [2004] showed crushing without loss of residual angle of internal friction. It seems that crushable granular materials experience a reduction in the internal friction angle as a consequence of particle breakage prior to achieve a constant value of residual strength.

## 2.3 CURRENT METHODS FOR MEASURING CRUSHING

Several methods for quantifying crushing in granular materials have been developed through out the years. Most of these techniques rely on comparing the grain size distribution of the soil before and after granular crushing. Lee and Farhoomand [1967] defined the ratio between  $d_{15}$  before and after crushing as the relative crushing. Hagerty et al. [1993] used the ratio  $d_{50}/d_{50\text{uncrushed}}$  to illustrate how crushing evolves when increasing the applied stresses. In these expressions  $d_x$  represents the opening size of the sieve that X% by weight of the sample passed through. Lade et al. [1996] suggest the use of another crushing indicator referred as  $B_{10} = 1 - d_{10f}/d_{10i}$ , where  $d_{10f}$  and  $d_{10i}$  represent the effective sizes of the final and initial grain size distributions. They suggest this indicator since the effective size can be used in

order to estimate the hydraulic conductivity of the soil by using the Hazen's equation. Although this kind of descriptors are easy to calculate, they just give a general idea since only consider the grain size distribution curves at one point. Other efforts have gone further than this and relate crushing with the area between the two curves. For example Hardin [1985] proposed a method for quantifying crushing based on the area between the original grain size distribution curve of the soil and the grain size distribution curve after crushing. For this method in particular the use of numerical integration or a planimeter is required.

Fractal analysis can also be used in order to describe changes in grain size distribution. The fragmentation fractal dimension,  $D_f$ , can be calculated with the following equation [Turcotte, 1986]:

$$N(R>r) = Kr^{-D_f} \quad (2.1)$$

Where  $N(R>r)$  is the number of particles with a radius  $R$  (could be other linear dimension) greater than a given value  $r$ .  $K$  represents a constant and  $D_f$  is the fragmentation fractal dimension. However, Eq.(2.1) is not easy to use since the number of particles is not often known. An equivalent expression developed by Tyler and Wheatcraft [1992] can be used if the grain size distribution by weight of the soil is known:

$$\frac{M(R < r)}{M_T} = \left( \frac{r}{r_L} \right)^{3-D_f} \quad (2.2)$$

Where  $M(R<r)$  is the cumulative mass of the particles with size  $R$  smaller than a given comparative size  $r$ .  $M_T$  represents the total mass of particles,  $r$  is the sieve size opening, and  $r_L$  is the maximum particle size as defined by the largest sieve size opening used in the analysis.  $D_f$  is the fragmentation fractal dimension.

$D_f$  can be used as a measure of particle size distribution. Well graded mixtures containing different sizes have higher values of  $D_f$ , while uniform size mixtures dominated by particles having the original size exhibit lower values. Several authors have reported maximum values of fragmentation fractal dimension around 2.5-2.6 for materials subjected to pure crushing [Turcotte, 1986], [Sammis, 1997], [Bolton and McDowell, 1997], [McDowell and Bolton, 1998], [McDowell and Daniell, 2001]. Nevertheless, a soil in the field can have a fragmentation fractal dimension higher than 2.6 as a result of an artificial sorting.

## **2.4 STATISTICS OF PARTICLE TENSILE STRENGTH**

Crushing occurs in two different forms: abrasion and particle fragmentation. Most of the detrimental effects associated with crushing such as settlements and reduction in hydraulic conductivity are related with particle fragmentation. Particle fragmentation takes place when a particle is subjected to a tensile stress greater than its tensile strength. However, determining a constant value of tensile strength is a complicated task when working with natural materials such as rock aggregates due to a high variability in the measured strengths.

The tensile strength of some man made materials such as steel is fairly constant and independent of the size of the tested specimen. These materials have a uniform structure that is not dominated by the presence of flaws or weak zones. Thus, every part of a perfect uniform material has the same strength as the whole group. On the other hand, natural materials such as soil particles or rock aggregates have a structure that is dominated by the presence of flaws or weak zones. Since these materials always fail by their weakest points and every specimen is unique, they often present a great variability in tensile strength. Thus, specimens having similar size and coming from the same material exhibit different values of strength, making possible to establish a relationship between average tensile strength and size of the

specimen [Billam, 1971], [McDowell and Bolton, 1998], [Nakata et al., 1999], [McDowell and Amon, 2000], [Nakata et al., 2001b], [Takei et al., 2001], [McDowell, 2002]. This is explained by the fact that a big specimen has a higher probability of having more and bigger defects than a small specimen [Hardin, 1985], [Lade et al., 1996]. Fig.2.2 shows how two different specimens coming from the same material could present different values of tensile strength due to the size and quantity of their flaws. The bigger specimen has more and bigger flaws than the smaller specimen, and thus it has a lower tensile strength [Ashby and Jones, 1998].

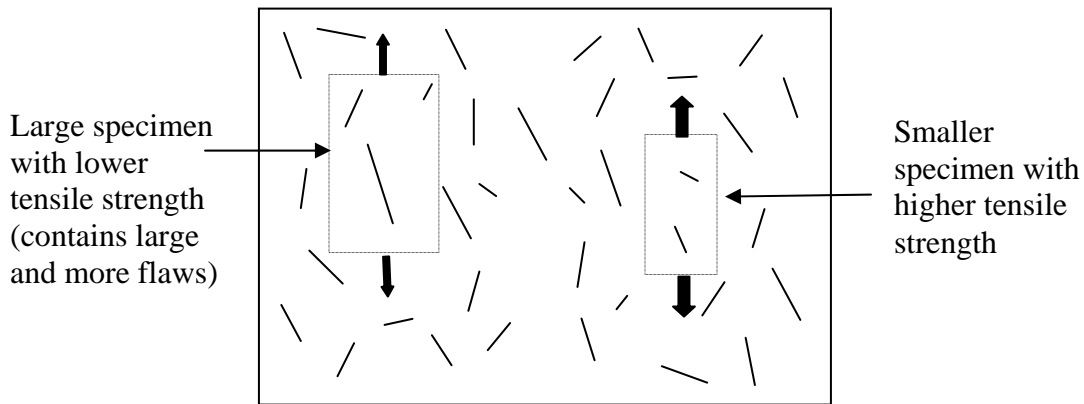


Figure 2.2. Different specimens coming from the same material (Modified from Ashby and Jones, 1998)

Since some natural materials used in the civil engineering practice such as rock aggregates present a significant variability in tensile strength, it becomes necessary to quantify this variability with simple statistical descriptors. A parameter called the Weibull modulus,  $m$ , can be used not only to describe the variability in tensile strength of specimens of similar size but also to describe the effect of specimen size in average tensile strength. Thus, this parameter condenses important information in just one number.

#### 2.4.1 Calculating Weibull statistics for specimens of similar size

Weibull found that the variability in tensile strength of specimens having similar size and coming from the same material could be described with the following equation [Ashby and Jones, 1998]:

$$P_s(V_0) = \exp \left[ - \left( \frac{\sigma}{\sigma_0} \right)^m \right] \quad (2.3)$$

Where  $P_s(V_0)$  is the probability that a specimen with a volume  $V_0$  has to survive an induced tensile stress  $\sigma$ . This probability is the number of specimens having a tensile strength greater than  $\sigma$ , divided by the total number of specimens tested. The parameter  $\sigma_0$  is the value of tensile stress such that 37% of the total number of specimens survive. The parameter  $m$  is known as the Weibull modulus. After testing several specimens of the same size a plot similar to Fig.2.3.a can be constructed and the values of  $\sigma_0$  and  $m$  can be calculated as illustrated in the figure.

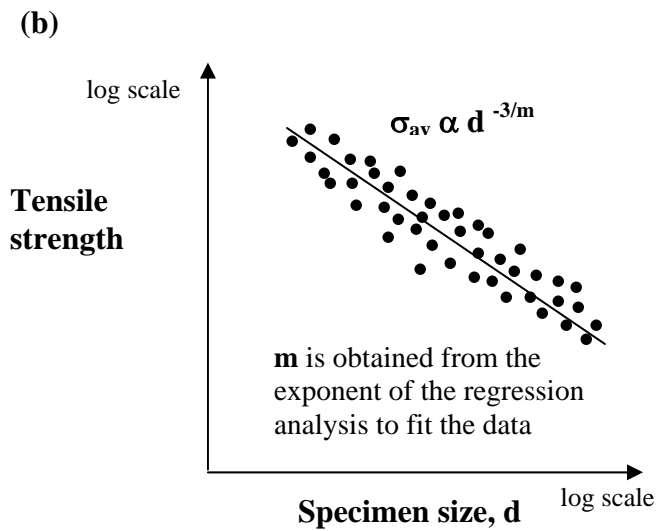
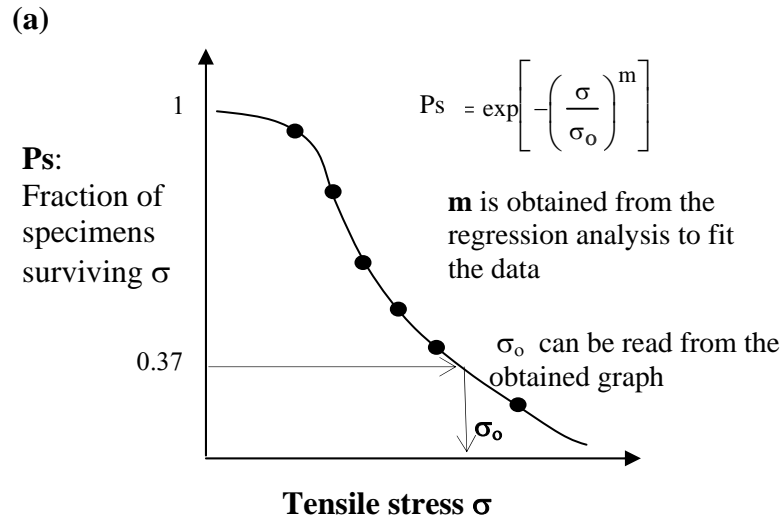


Figure 2.3 Calculation of the Weibull modulus: (a) based on survival probabilities, (b) based on a size-strength relationship.

#### 2.4.2 Calculating Weibull statistics for specimens of different sizes

Another way to calculate the Weibull modulus for a given material is to test specimens of different sizes. The average tensile strength,  $\sigma_{av}$ , for a specimen is proportional to its size,  $d$ , and the Weibull modulus of the material [McDowell and Amon, 2000], [McDowell, 2001]:

$$\sigma_{av} \propto d^{-3/m} \quad (2.4)$$

Thus, Eq.(2.4) can be used to find the value of  $m$  as shown in Fig.2.3.b. The Weibull modulus,  $m$ , is equal to 3 divided by the exponent obtained after applying a power regression to the experimental results. Eq.(2.4) is in agreement with the fact that the average tensile strength of a specimen decreases with increasing its size. The values of the Weibull modulus calculated using the two different approaches should be equal.

#### 2.4.3 Significance and typical values of the Weibull modulus “ $m$ ”

The value of  $m$  reflects the variability in tensile strength of the analyzed material. Steel which is a very uniform material with no defects on its structure has a Weibull modulus around 100 as reported by Ashby and Jones [1998]. Other engineering materials such as ceramics have  $m$  values of 10 [McDowell et al., 1996]. Chalk, pottery and cement have values of  $m$  around 5 [McDowell and Bolton, 1998]. Takei et al. [2001] reported values of  $m$  equal to 7.5 for chalk, 8 for glass beads, and between 2 and 3 for quartz sands. Nakata et al. [2001b], McDowell [2002], and Cheng et al. [2003] also reported  $m$  values around 3 for silica sand. McDowell and Humphreys [2002] obtained values of  $m$  for weak granular materials such as 3.1 for rice krispies, and 2.5 for pasta. McDowell and Amon [2000] reported a value of  $m$  equal to 1.5 for Quiou sand. In summary, the more uniform the material is, the higher the value of  $m$  and the smaller the variability in tensile strength.

#### 2.4.4 An example of the application of Weibull statistics

A simple example of the application of Weibull statistics is shown next in order to illustrate the importance of the Weibull modulus. More than 390 point load tests were carried out in several samples coming from two different rocks: a red Biotite Gneiss and a grey Quartzite. The point load tests were conducted following the ASTM standard D5731-02. In this test a rock aggregate is subjected to a

diametrical compression by vertically moving two conical platens until the induced horizontal tensile stress inside the sample causes its breakage. A characteristic tensile strength is calculated as the force required to break the particle,  $F$ , divided by the square of the separation of the conical platens,  $d$ , as explained in Fig.2.4. Even though this characteristic tensile strength is only an approximation of the real tensile strength of the material, is the only feasible way to establish a value of tensile strength in rock fragments at the size of aggregates.

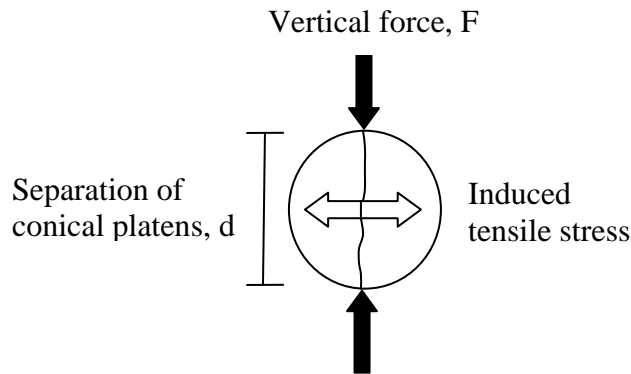


Figure 2.4. Schematic description of the point load test

A plot showing the relationship between size and tensile strength was constructed for each material. From these results the Weibull modulus were calculated. After this, the information collected from each material was organized depending on the size of the particles. Plots of survival probability were constructed for each group using the obtained laboratory results and those predicted by Eq.(2.3).

Fig.2.5 shows the obtained relationships for the characteristic tensile strength vs. size of the specimen for both materials. The Weibull modulus were calculated using Eq.(2.4) as 3 divided by the obtained exponents. The Biotite Gneiss had a Weibull modulus of 2.75 while the Grey Quartzite had a Weibull modulus of 4.23. These numbers are consistent with the fact that the Biotite Gneiss had more variability than the Grey Quartzite. The greater variability of the Biotite Gneiss compared to the Grey

Quartzite is reflected not only in the greater dispersion of the obtained data but also in the stronger influence of size in the tensile strength of the specimens as reflected by the exponents of the regression lines (-1.091 for the Biotite Gneiss vs. -0.7092 for the Grey Quartzite). The reason for this greater variability lays in the structure of each material as shown in Fig.2.6. The Grey Quartzite has a uniform structure with less weak planes than the Biotite Gneiss.

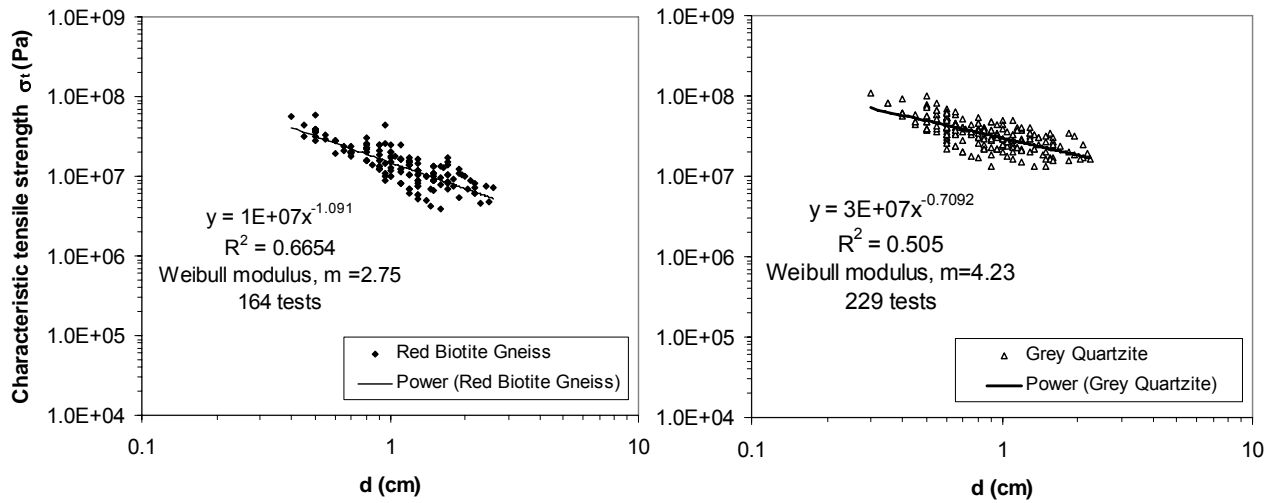


Figure 2.5. Characteristic tensile strength vs. specimen size

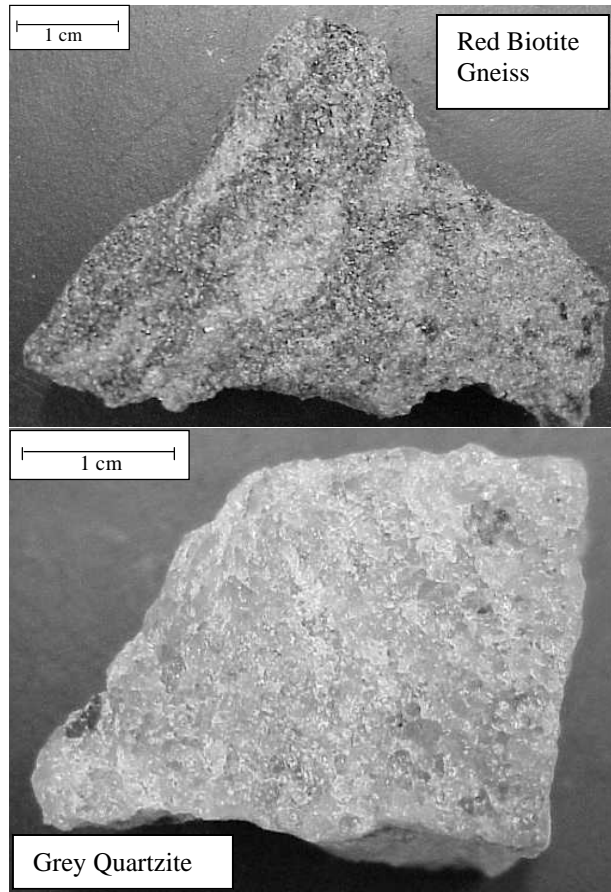


Figure 2.6. Photographs of the tested materials.

Fig.2.5 also shows the square of the correlation values (coefficient of determination) for the two different materials. The Biotite Gneiss had an  $R^2$  equal to 0.665 while the Grey Quartzite had a value equal to 0.505. These values are rather low and do not give a clear indication of the variability in tensile strength of the samples. It is not possible to conclude what material present more variability in tensile strength by only using this descriptor. On the other hand, the Weibull modulus  $m$  gives a clear indication of the variability in tensile strength including the influence of specimen size on the average tensile strength.

The results obtained on particles with a value of  $d$  between 1cm and 2cm were used to construct survival probability graphs for each material. Even though all the particles in the established range did not have the exact same size, they were grouped together since they have a similar size and it was the only

way to conform a group of several specimens. Fig.2.7 shows the obtained results. Also, the survival probabilities were predicted using Eq.(2.3) and the Weibull modulus obtained in Fig.2.5. It can be observed a good agreement between the obtained and the predicted values.

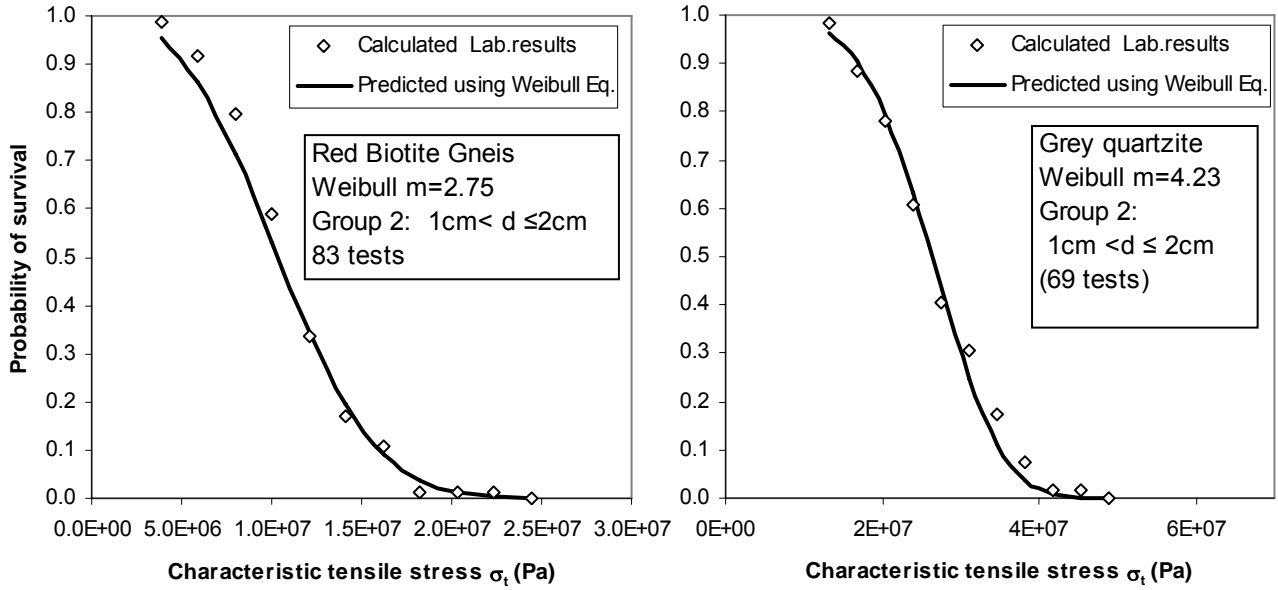


Figure 2.7. Survival probabilities: comparison between calculated and predicted values.

In summary, the Weibull modulus is a very useful statistical descriptor that can be used not only to quantify the variability in tensile strength of particles of similar size but also to describe the effect of specimen size in the average tensile strength.

### **3.0 LABORATORY TESTS USING A WEAK GRANULAR MATERIAL**

There are different tools that can be used to study the evolution of crushing in granular materials. Some of these tools are simple laboratory tests while others consist on numerical modeling. This chapter focuses on laboratory tests. Since common soil particles such as sand grains require higher loads to be crushed, most of the standard geotechnical equipment can not be used for these purposes. There are two possible solutions to this problem: the first one is to work with bigger and stronger machines while the second solution is to work with weaker materials. This chapter shows the results of laboratory tests conducted in order to study how crushing evolves in a weak granular material. Raw sugar was used in confined uniaxial compression tests, direct shear tests, and ring shear tests.

#### **3.1 SUGAR AS A WEAK GRANULAR MATERIAL**

Studying crushing of granular materials has always been limited by the equipment needed to develop the considerable loads that can lead to grain fragmentation. One way to sidestep this is to use standard geotechnical equipment with weak granular materials [Mandl et al., 1977], [McDowell and Humphreys, 2002], [McDowell and Khan, 2003]. Raw sugar was chosen as a suitable weak granular material and different laboratory tests were performed on different samples of the same sugar. The used sugar had an average diameter equal to 1.015mm (between No.16 and No.20 sieves) and a specific gravity ( $G_s$ ) equal to 1.5. The natural angle of repose of this material was found to be  $40^\circ$  as shown on Fig.3.1. During the testing program the humidity and air temperature were carefully controlled, so the used sugar did not experience any visible change in structure.

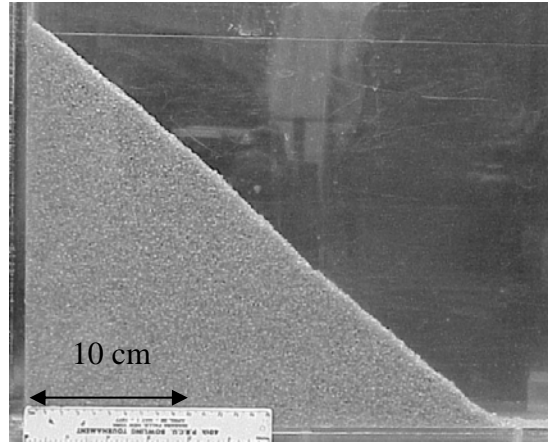


Figure 3.1. Natural angle of repose of the sugar

### 3.2 CONFINED UNIAXIAL COMPRESSION TESTS

A Versa Loader machine was used in the confined uniaxial compression tests. The sugar was placed in a loose state inside a Plexiglas cylinder having an internal diameter equal to 5cm. The samples were subjected to loading and unloading conditions in the cylinder (loading and unloading rate = 0.063in/min). The vertical deformation of the sample was continuously recorded using a LVDT transducer. Each sample was subjected to a different value of maximum vertical stress (between 325kPa and 1548kPa). At the end of each test, the samples were subjected to a sieve analysis.

#### 3.2.1 Void ratio

The relationship between the applied vertical stress and the void ratio for the samples subjected to the five maximum vertical stresses is shown in Fig.3.2.

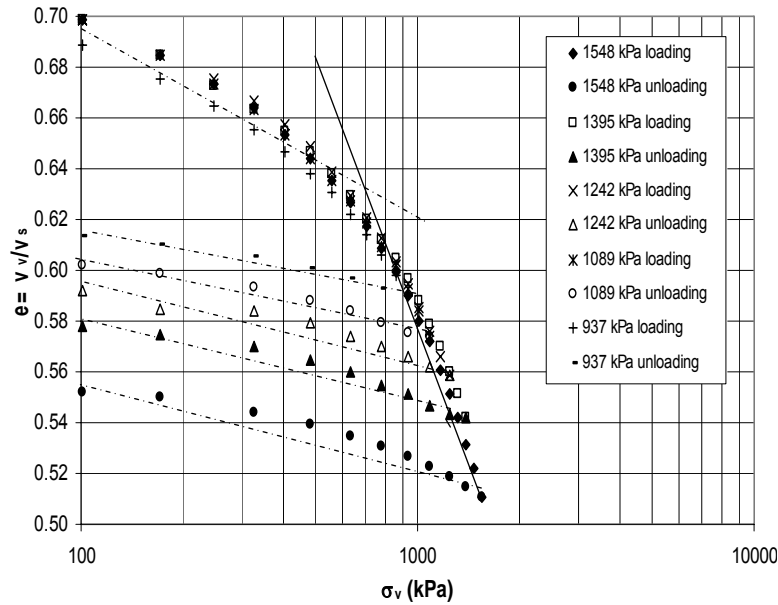


Figure 3.2. Vertical stress vs. void ratio, confined uniaxial compression tests.

Fig. 3.2 shows the typical trend exhibited by a granular material when subjected to vertical compressive stresses [Terzaghi, 1948], [Hagerty et al., 1993], [Pestana and Whittle, 1995], [MacDowell and Bolton, 1998], [Nakata et al., 2001a]. In Fig. 3.2, three different stages can be distinguished. In the first stage (for a vertical stress between 100 and 700 kPa), the void ratio changed very little (from 0.695 to 0.635). This small change in void ratio was the result of grain rearrangement during compression, a slight level of crushing in the form of abrasion of the particles, and some elastic deformation. In the second stage (vertical stress between 700 to 1548 kPa), the void ratio changed substantially (from 0.635 to 0.51). This change in void ratio was mainly the result of crushing of the sugar particles. The third stage took place during the unloading of the samples. The changes in void ratio of the samples during this unloading stage were the result of their elastic rebound.

### 3.2.2 Sieve analyses

Sieve analyses were conducted after the compression tests. The sugar grains had an average diameter equal to 1.015 mm before they were subjected to the compressive loads. After the compressive

loads were in effect on the samples, some of the grains broke. Fig. 3.3 indicates the percentages of the different sizes in the samples after the compression tests. This figure shows that as the compression levels increased, the percentage of the grains with the original size decreased, and the percentage of the grains with size smaller than the original size increased.

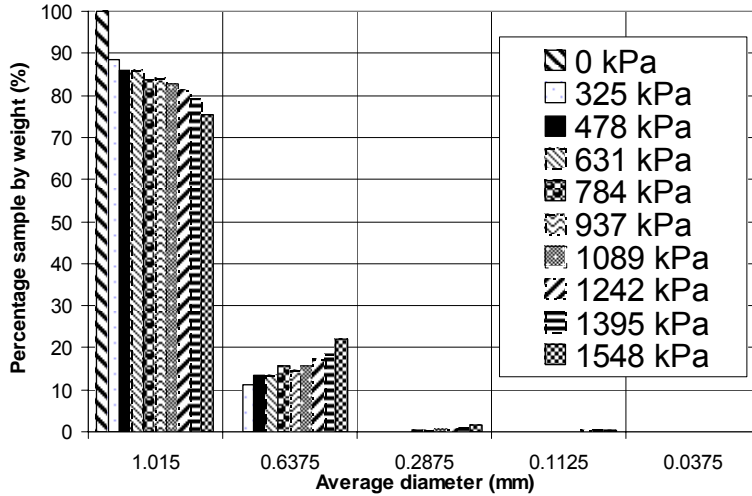


Figure 3.3 Particle size distributions after the compression tests.

The fragmentation fractal dimension of the tested samples were calculated using Eq.(2.2). Figure 3.4 shows the calculation for the sample subjected to 1548 kPa. Similar plots were obtained for the other samples.

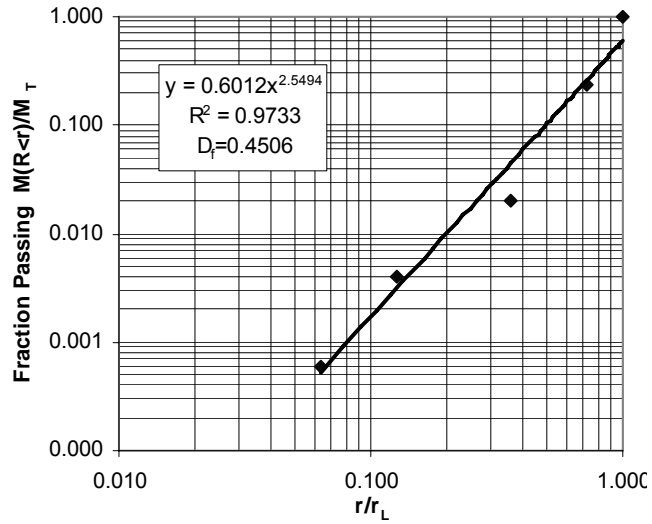


Figure 3.4 Fragmentation fractal dimension,  $\sigma_v = 1548$  kPa

Figure 3.5 shows the relationship between the maximum applied vertical stress and the fragmentation fractal dimension for each sample. It can be noted that the fragmentation fractal dimension increased as the applied vertical stress increased. This means that the original uniform samples tended to become a well graded mixture of sizes due to particle crushing.

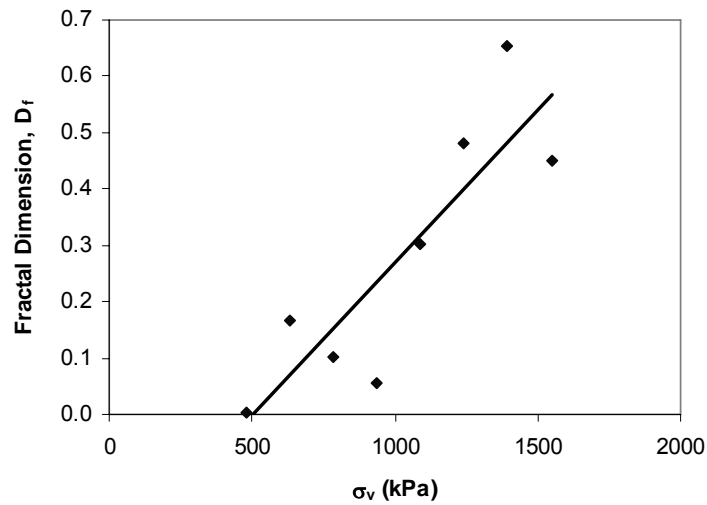


Figure 3.5 Applied vertical stress vs fragmentation fractal dimension

### 3.2.3 Elastic modulus

The Young's modulus of elasticity can be obtained from the compression-uniaxial strain relationships. The elastic modulus,  $E$ , changes during compression and can be obtained at different points of the compression-axial strain curve from the ratio between a small increment in vertical stress ( $d\sigma$ ) and the corresponding increment in vertical strain ( $d\varepsilon$ ). Since the increments in vertical strain and vertical load were recorded at every step of the compression tests, a relationship between the vertical stress and  $d\sigma/d\varepsilon$  was established. Fig. 3.6 shows a plot of the elastic modulus as it changes with the levels of compression. An analysis of Fig. 3.6 indicates that the elastic modulus increased with the levels of compression reaching a maximum at a value of compressive stress equal to 700 kPa to 800 kPa. After this compressive stress was reached, the modulus of elasticity decreased slightly. If one considers Fig.3.2, the compressive stress separating the stages dominated by particle rearrangement or by granular crushing was equal to 700 kPa. From a comparison of Figs. 3.2 and 3.6 it can be concluded that the elastic moduli of the granular material increases as a result of particle rearrangement and particle abrasion and tends to decrease slightly as a result of particle crushing.

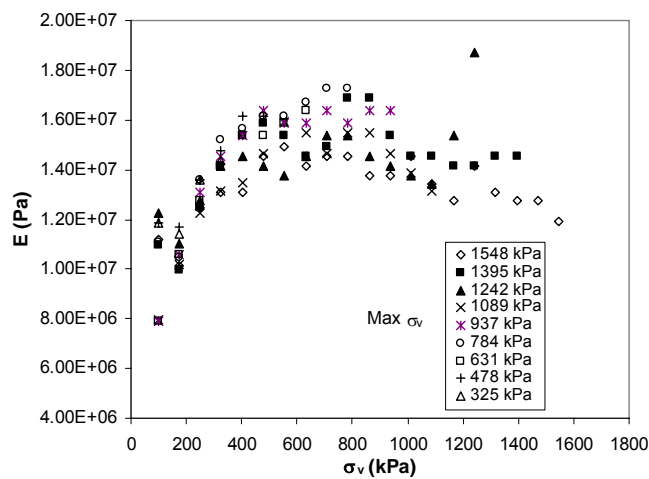


Figure 3.6 Vertical stress,  $\sigma_v$ , versus Young's Modulus of Elasticity,  $E$ .

### 3.3 DIRECT SHEAR TESTS

A circular direct shear box having an inside diameter of 6.35cm and a sample height of 2.1cm was used in the direct shear tests. Vertical stresses that range in value between 110 kPa and 225 kPa were used. These vertical stresses are substantially smaller than those used in the confined uniaxial compression tests. The samples were prepared by placing the sugar in a loose state (pluviation method) inside the shear box; then, the shear box was vertically loaded to normal stresses that varied between 110 and 225 kPa. These normal stresses were kept on the samples for a period of 10 minutes. During this time, the samples deformed vertically. After this, the samples were subjected to shear stresses. Changes experienced by the samples were recorded at 0, 3, 6 and 9 mm horizontal deformation of the samples. After each of these horizontal deformations was reached by the samples, they were removed from the shear box and were subjected to sieve analysis and microscopic inspection. For each vertical stress used, four different samples (deformed to 0, 3, 6, and 9 mm) were used for the shear-deformation analysis.

#### 3.3.1 Mobilized friction coefficient

Fig.3.7 shows the curves relating the friction coefficient ( $\tau/\sigma$ ) and the level of horizontal deformation for the five vertical stresses used in the direct shear tests. For each vertical stress, only the results of the sample subjected to a deformation of 9mm are presented since these results include those at deformations of 3mm and 6mm. Fig.3.7 indicates very little variation of the coefficient of friction with respect to the normal stresses used in the tests.

It can be observed that the maximum friction coefficient for all the vertical stresses varied between 0.78 and 0.9 (corresponding to angles of shearing resistance between  $38^\circ$  and  $42^\circ$ ). This variability could be the result of random changes of average porosity or fabric during the preparation of

the samples. An average value for the maximum coefficient of friction is 0.82 that corresponds with an angle of shearing resistance equal to  $39.4^\circ$ . This angle of shear resistance is slightly lower than the angle of friction before crushing ( $40^\circ$ ). On the other hand, it can be seen that at every vertical stress level (except  $\sigma_v=110$  kPa), the friction coefficient decreased slightly with displacement.

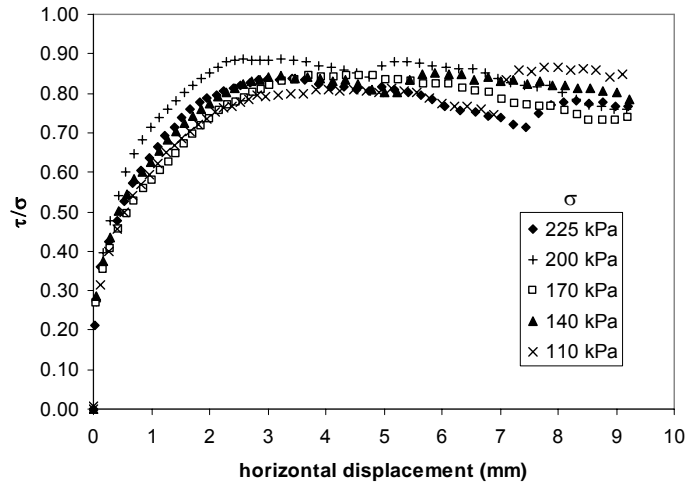


Figure 3.7 Horizontal deformation vs. friction coefficient.

### 3.3.2 Photographic analysis

Fig. 3.8 shows a picture of some particles from three different samples subjected to an average vertical stress of 110 kPa, but to a different horizontal deformation. This value of vertical stress was the smallest one used in the tests. Fig.3.9 shows a picture of some particles from three different samples all subjected to a vertical stress equal to 225 kPa. This vertical stress was the largest one used in the direct shear tests. In Figs.3.8 and 3.9, the sugar grains located in a row represent the size of the grains passing and being retained on certain sieves. The sugar grains in a column of the photographs represent the different sugar grain sizes that the samples developed at different values of the horizontal deformation in the shear tests.

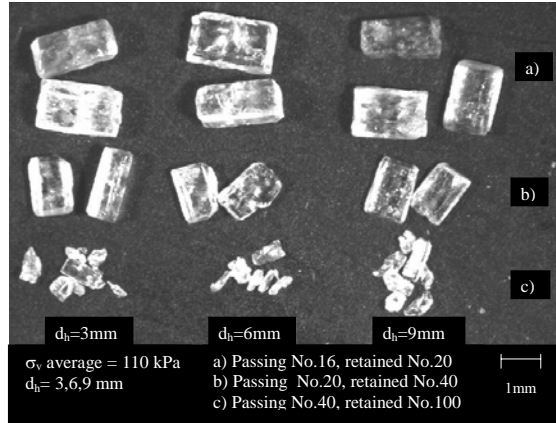


Figure 3.8 Samples subjected to an average vertical stress of 110 kPa.

An analysis of Figs. 3.8 and 3.9 indicates that the samples broke and developed fines as the vertical stress was increased on the samples or as the amount of deformation was also increased. During the combination of normal and shear stresses, the sharp corners of the grains broke producing the smaller particles in Fig.3.8 and 3.9. The larger particles also break in two large pieces. The fragmentation of the sugar during the direct shear tests changed the sugar from a uniform granular material into a somewhat well graded material.

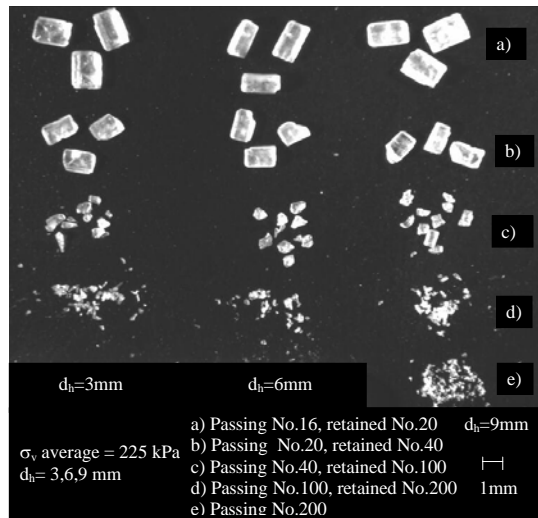


Figure 3.9 Samples subjected to an average vertical stress of 225 kPa.

### 3.3.3 Sieve analyses

The results of some of the sieve analyses are presented in Figs.3.10, 3.11 and 3.12. Fig.3.10 presents the sieve analyses for the samples subjected to a 110 kPa normal stress. Fig.3.11 for the samples subjected to a 200 kPa normal stress. And Fig.3.12 for the samples subjected to a 225 kPa normal stress. Figs. 3.10 to 3.12 also indicate the size distribution of the grains for the different values of horizontal deformation in the direct shear tests. Under 110 kPa, the samples experienced a very small amount of breakage. A comparison of Figs. 3.11 and 3.12 shows that the two plots are very similar. The similarity of these plots is a sign that no further crushing was generated by the increment in the vertical stress.

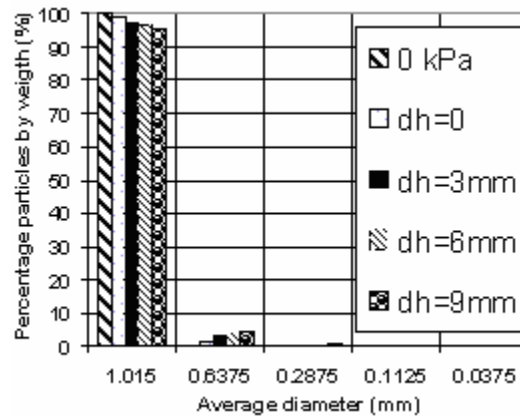


Figure 3.10 Particle size distribution,  $\sigma_v=110$  kPa.

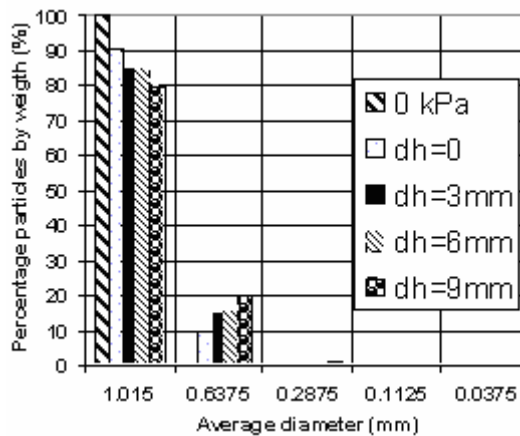


Figure 3.11 Particle size distribution,  $\sigma_v=200$  kPa.

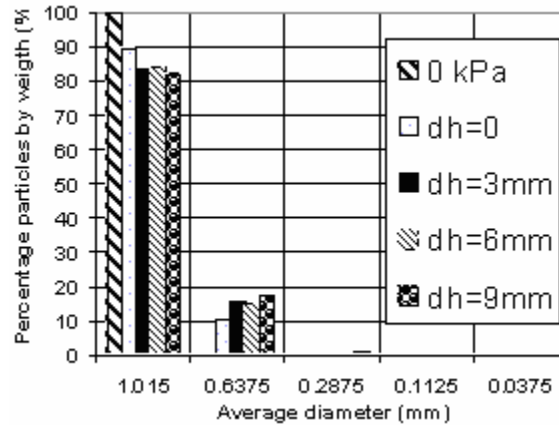


Figure 3.12 Particle size distribution,  $\sigma_v=225$  kPa.

A comparison of the results at 200 kPa and 225 kPa presented in Fig.3.7 and the results presented in Fig.3.11 and 3.12 shows that most of the crushing during the shearing stage took place at the 0-3mm displacement interval. This suggests that as the peak strength is reached, some particles had broken. After the peak resistance, the strength drops off slightly and with little subsequent breakage of the particles. Most of the fragments generated by crushing were particles with a diameter of 0.6375mm (almost half of the original average diameter).

Comparing the amount of crushing obtained under a uniaxial compression stress of 1395 kPa (Fig.3.3) and the crushing results obtained in the direct shear test under vertical stresses of 200 kPa or 225 kPa and a horizontal deformation of 9mm, it can be established that the same degree of crushing was reached in the samples. However, the level of vertical stress used in the compression test was about six times greater than the normal stress used in the direct shear test. Thus crushing can be generated in granular materials under low values of normal stress if a shear stress is also applied.

The results from the calculations of the fragmentation fractal dimension are not presented since the samples reached the same grain size distribution of the samples tested in the confined uniaxial compression tests.

### 3.3.4 Volumetric changes

Fig. 3.13 shows the vertical and horizontal displacements experienced by the samples at a vertical stress of 225 kPa. These results are representative of those obtained at different values of vertical stress. The measured vertical displacements of the samples started from a value different than zero since each sample was allowed to deform after the application of the vertical load prior to the shearing stage. This initial vertical deformation was produced by particle crushing and particle rearrangement. Similarly, due to particle crushing and particle rearrangement the sample contracted during the first part of the shearing phase (horizontal displacement < 2mm). However, after this first phase of decrease in volume due to shearing, the sample experienced dilation. Fig.3.13 shows that at a horizontal deformation close to 3 mm the sample had almost the same height that it had at the beginning of the shearing stage. After this horizontal deformation, the sample experienced a slight increase in volume as a result of dilatancy.

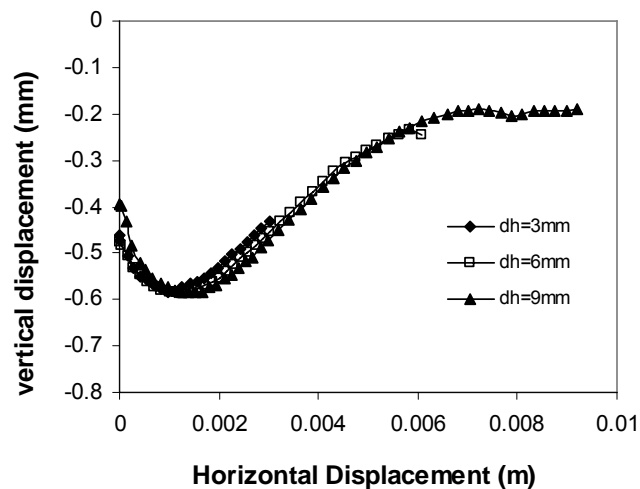


Figure 3.13 Vertical deformation vs. horizontal deformation  $\sigma_v=225\text{kPa}$ .

In summary a complex interaction between contraction due to crushing and dilatancy due to particle rearrangement took place inside the samples as they were sheared.

### 3.4 RING SHEAR TESTS

Ring shear tests were carried out using sugar in a standard Bromhead type apparatus. The tested samples had an outside radius of 5cm and an inside radius of 3.5cm. The height of the samples was equal to 5mm. They were prepared by placing the sugar inside the ring shear by using the pluviation method. Thus, the samples had a loose state at the beginning of the tests and crushing of the sugar grains was avoided during the preparation of the samples. Three different vertical stresses were used in the testing program: 198 kPa, 296 kPa, and 394 kPa. The angular velocity of the upper part of the ring shear was equal to 1.2 degree/minute.

#### 3.4.1 Mobilized friction coefficient

Fig.3.14 shows the curves relating the mobilized friction coefficient ( $\tau/\sigma$ ) and the level of horizontal deformation for the vertical stresses used on the tests (horizontal displacement = [average radius][angular displacement in rads]). As is explained later, it was found that the sugar achieved an almost constant grading before completing one revolution (horizontal displacement of 26.7cm), and very small crushing was expected to occur after this deformation. Fig.3.14 indicates little variation of the mobilized friction coefficient with respect to the normal stresses and the induced deformations. It can be observed that a constant friction coefficient for all the vertical stresses varied between 0.55 and 0.6 (corresponding to angles of shearing resistance between  $28.8^\circ$  and  $31^\circ$ ). An average value for this constant friction coefficient is 0.575 that corresponds with an angle of shearing resistance of  $29.9^\circ$ . This angle of shear resistance is considerably lower than the angle of friction before crushing ( $40^\circ$ ) measured with the angle of repose. This constant internal friction angle represents the residual state friction angle of the material.

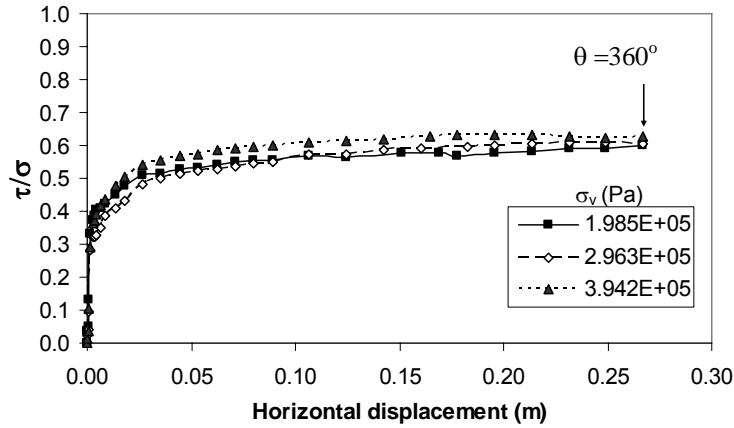


Figure 3.14 Friction coefficient vs. horizontal deformation.

### 3.4.2 The evolution of crushing

Fig.3.15 shows the average size compositions of the three samples subjected to vertical stresses of 198kPa, 296kPa, and 394 kPa after one revolution in the ring shear. Fig.3.15 also shows how the original uniform material became a well graded mixture of sizes after the tests. It can be noted that the amount of crushing increased with the magnitude of the applied vertical stress. A comparison of Fig.3.14 and Fig.3.15 shows that even though the samples had different level of crushing they all exhibited a constant friction coefficient. This is in agreement with the laboratory results reported by Coop et al. [2004].

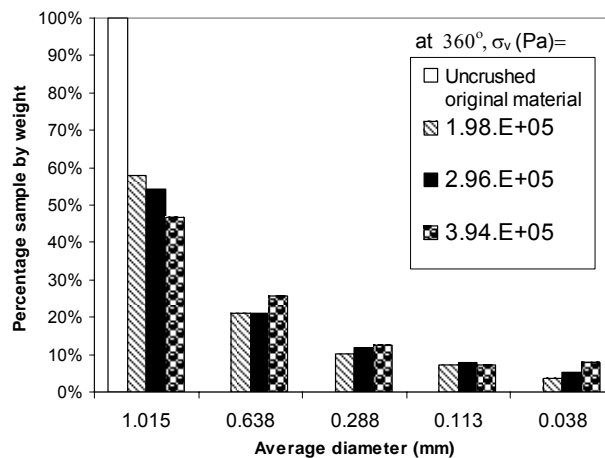


Figure 3.15. Particle size distribution of the samples after one revolution in the ring shear

Fig.3.15 does not provide any information regarding the evolution of crushing inside the samples with respect to the horizontal deformation since it only shows the final configuration of the sugar particles. Thus, four more tests were conducted on the ring shear apparatus. The four tests had vertical stresses of 296kPa, but where ended at different values of angular deformation ( $0^\circ$ ,  $90^\circ$ ,  $180^\circ$ ,  $270^\circ$ ). Fig.3.16 shows the average size compositions of the four samples at the end of each test (the results obtained at  $360^\circ$  were also included in this figure). It can be observed that most of the crushing was produced before an angular deformation of  $90^\circ$ . Moreover, there was only a small amount of crushing (almost 3%) between angular deformations of  $270^\circ$  and  $360^\circ$ . It can be concluded that the sample at  $360^\circ$  tended to reach a stable grain size distribution where almost no crushing was expected to occur.

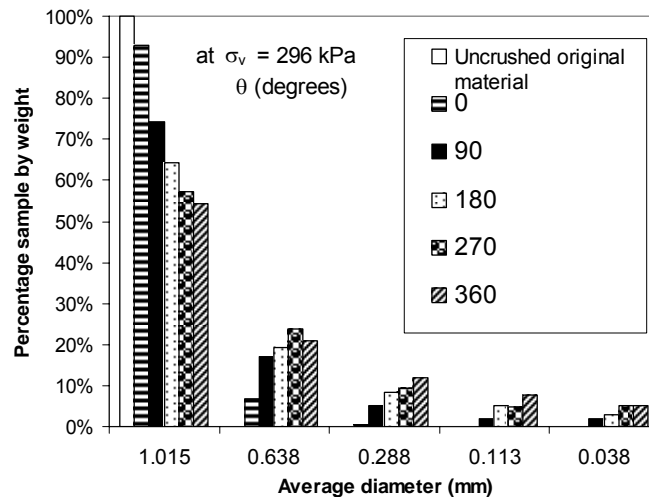


Figure 3.16. Particle size distribution of the laboratory samples at  $\sigma_v=296$  kPa.

Using the results from the sieve analyses, the fragmentation fractal dimension of the samples were calculated using Eq.(2.2). Fig.3.17 shows the obtained results. Power regression lines were added to the laboratory data. It can be noted that the fragmentation fractal dimensions of the samples corresponding to angular deformations of  $270^\circ$  and  $360^\circ$  were similar (2.014 and 2.03) which confirms that the sample reached a stable grading where no further crushing was expected to occur. However, these values are below the maximum fragmentation fractal dimension (around 2.5-2.6) reported in the

literature (Chapter 2). This is in agreement with the fact that more crushing was produced when increasing the applied vertical stress.

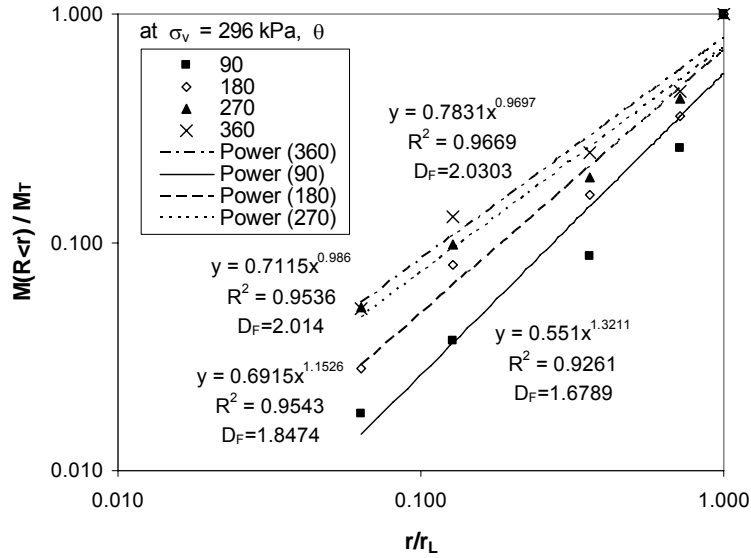


Figure 3.17 Fragmentation fractal dimensions of samples at  $\sigma_v=296$  kPa.

Fig.3.18 shows a photograph of selected particles from the samples after the tests. Each column shows particles from samples subjected to different values of angular deformation, while each row shows the size of these particles. It is interesting to see how the original particles fractured into two big particles and some small fragments. Also, it can be noted how some particles lost their angularities as a result of crushing.

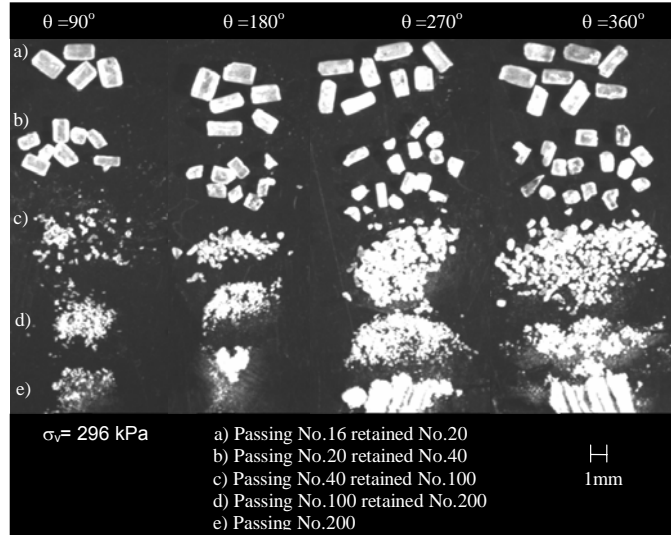


Figure 3.18 Photograph of particles from the laboratory samples,  $\sigma_v=296$  kPa.

### 3.5 CONCLUSIONS ABOUT THE LABORATORY RESULTS

The results from the laboratory tests provided a better understanding of the crushable behavior of granular materials. The results of the confined uniaxial compression tests indicated the existence of a yield stress that is reflected on the void ratio vs vertical stress curve, and influences also the elastic modulus of the crushable material. This yield stress corresponds with the point where the deformation of the material changed from a stage dominated by particle rearrangement, a slight level of abrasion, and some elastic deformation to a stage dominated by particle crushing, its associated particle rearrangement, and some elastic deformation. These tests also showed that as a result of particle crushing the granular material tended to evolve toward a fractal distribution of sizes.

The results of the direct shear tests showed that the level of crushing produced by a large compressive stress can also be obtained by using combinations of small normal stresses and shear stresses. These tests also showed how the peak friction coefficient of the material somehow decreased as

a result of particle breakage. An interesting interaction between contraction of the material due to particle crushing and dilation of the material due to particle rearrangement was found to take place as the samples were sheared.

The results from the ring shear tests showed that the residual friction coefficient did not change regardless of the severe degradation of the crushable material. It was found that a large value of deformation was required to reach a stable grading of the samples. This stable grading was found to be fractal and related to the value of the applied vertical stress. The value of the fragmentation fractal dimension of the samples after the tests were much higher than those obtained in the other laboratory tests. This is due to the fact that the ring shear test induces larger values of horizontal strain with a more severe combination of normal and shear stresses.

The photographs of randomly selected particles from the samples after the tests showed how the particles broke mainly into two big fragments and some small particles. These photographs also showed the influence of the induced levels of deformation and stress.

## 4.0 DEM AND PARTICLE BREAKAGE CRITERION

### 4.1 THE DISCRETE ELEMENT METHOD

The Discrete Element Method (DEM), originally developed by Cundall and Strack [1979], is a powerful tool that has been used during the past few years to study the behavior of granular materials. Programs such as the Itasca PFC<sup>2D</sup> or PFC<sup>3D</sup> are commercial numerical codes based on this method. Since this research project uses the Itasca PFC<sup>2D</sup>, some general assumptions and principles of this code are presented. All the information comes from the PFC<sup>2D</sup> manuals [Itasca, Theory and Background]. There are some basic assumptions that need to be done when modeling with this program:

- Particles are idealized as circular rigid disks that interact at their contacts.
- Particles are allowed to overlap at their contacts, but these overlaps are small compared to the size of the particles.
- Contacts can be characterized by a force displacement law, so the force in a contact is related to the magnitude of the overlap.

PFC<sup>2D</sup> uses an explicit numerical scheme. The calculations performed by the program are based on the interaction between the numerical integration of the Newton's second law applied to each particle and the force displacement laws applied to each contact. The force-displacement laws are applied separately for the normal and shear components of the contact force. In this way, there are two different kinds of stiffness, the normal stiffness and the shear stiffness. In general, the constitutive model for each

contact consists on three different models: the contact-stiffness model, the slip model, and the bonding model.

- Contact-stiffness model: is defined as the relationship between force and magnitude of the overlap at the contact. PFC<sup>2D</sup> understands linear models and simplified Hertz-Mindlin models. Only the linear stiffness model was used in this research project. For this model, both the normal and shear stiffness in a contact are calculated as if the two entities (particle-particle or particle-wall) act in series.
- Slip model: this model allows the particles to slip by defining a maximum allowable shear force at the contact. It is based on the contact friction coefficient  $\mu$ . This friction coefficient is chosen by the program as the lowest friction coefficient from the two entities (particle-particle or particle-wall). Therefore, the maximum shear force in the contact is set to  $F_{\max}^s = \mu |F_i^n|$ , where  $F_{\max}^s$  is the maximum allowable shear force and  $F_i^n$  is the normal force on the contact. If the applied shear force on the contact is higher than  $F_{\max}^s$ , a slip condition will take place.
- Bonding model: this model recreates glue bonding the two particles in a contact. PFC<sup>2D</sup> recognized two different bonding models: the contact-bond model and the parallel-bond model. Only the contact-bond model was used in this project (Pavement simulation, Chapter 6). Maximum values of normal and shear forces are specified in order to characterize the strength of the bond.

A schematic description of these models is shown in Fig.4.1 [Adapted from Itasca, PFC<sup>2D</sup> User's Guide].

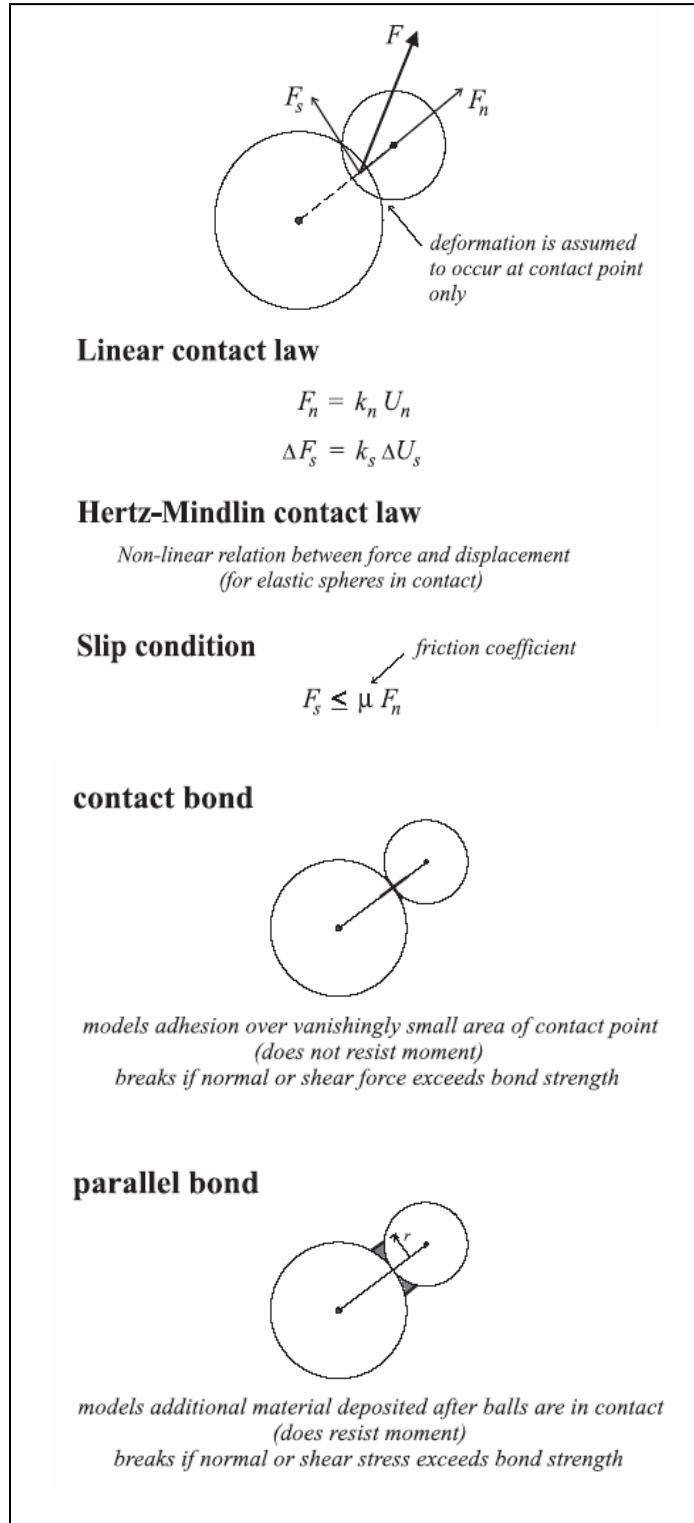


Figure 4.1 Summary of the constitutive model of PFC<sup>2D</sup>  
(Figure from the User's guide volume of the Itasca PFC<sup>2D</sup> manuals)

A simulation in PFC<sup>2D</sup> starts by generating particles and walls and defining the values used on the constitutive models. Walls have similar properties to those that can be specified for particles. Boundary and initial conditions such as the velocity of the walls, the initial velocity of the particles, the gravitational field, and many others can be established. Also, several variables such as the contact forces in the arrangement, the velocity and displacement of the particles, the porosity of the media, and many other can be continuously monitored and if desired they can be plotted as the simulation progresses. Also, PFC<sup>2D</sup> allows the user to create his own functions by programming and using the FISH language that is embedded in the code. In this way, the user can generate his own variables and plots and he can even create functions that interact with the course of the simulation.

#### **4.2 THE ROLE OF PARTICLE ROTATION: A DEM LIMITATION**

Previous research has shown that particle rotation plays an important role in the micromechanics of a real granular material when subjected to shearing, having an important effect on its shear strength [Skinner, 1969], [Corriveau et al., 1997], [Oda et al., 1997], [Iwashita and Oda, 1998], [Oda and Kazama, 1998]. Even though DEM considers this, it tends to overestimate the real amount of particle rotation that actually takes place [Iwashita and Oda, 1998], [Jensen et al., 1999], [Morgan, 2004]. This could be the reason why DEM simulations often present a friction coefficient of the sample smaller than the friction coefficient between the particles forming the sample [Bardet and Proubet, 1991]. This could also explain why at large values of shear strain, DEM simulations show a residual friction coefficient around 0.3 while real granular materials present results around 0.6 [Morgan, 1999].

Possible solutions to the excess of particles rotation have been proposed and implemented by different researchers. For example, it is often argued that considering ellipses (2D) or ellipsoids (3D) instead of disks or spheres gives a better representation of real granular materials [Lin and Ng, 1997]. Other solutions include the consideration of some kind of rotational restraint at the contacts [Oda et al.,

1997], [Iwashita and Oda, 1998], [Morgan, 2004], and the use of clusters which is a group of bonded particles simulating a non circular shape [Jensen et al., 1999]. Even though the implementations of these solutions have shown interesting results, they were not considered in this research project. The author believes that it is better just to keep in mind the effects of particle rotation than trying to include new unknown variables in the analysis. Perhaps there could be many other reasons why excess particle rotation takes place, such as the lack of restraint in the plane perpendicular to the 2D plane considered in the simulations [Morgan, 1999].

### **4.3 ALLOWING PARTICLE BREAKAGE**

#### **4.3.1 Previous work**

Numerical simulations in the form of DEM can be used for the visualization of crushing. Since the original DEM developed by Cundall and Strack [1979] did not consider particle breakage, different solutions have been proposed to overcome this constraint.

One solution to this problem is to treat each granular particle as an agglomerate built by bonding smaller particles. In order to establish a failure criterion, the strength of the bond between the particles forming the agglomerates needs to be specified. The crushing of a single agglomerate loaded between flat platens can be simulated in order to establish this value. This approach has been used by Cheng et al. [2003] when modeling isotropic compression tests, and McDowell and Harireche [2002] when modeling normal compression of sand. Harireche and McDowell [2003] and Lim and McDowell [2005] have also used this approach. A slightly different technique was used by Jensen et al. [2001] when modeling particle damage in a shear zone similar to the one induced in a ring shear test. Even though they also considered that an aggregate can initially be modeled as a group of jointed particles, they used a clustering technique based on a sliding energy criterion to establish when an initial cluster can partially or

fully disaggregate. A similar but slightly different technique called the lattice solid model has also been used by Mora and Place [1994], and Place and Mora [2000]. This technique also considers bonded particles as the original structures.

A different solution to the particle breakage problem is to replace the particles fulfilling a predefined failure criterion with an equivalent group of smaller particles. For example, when modeling comminution of granular materials in fault gouges, Lang [2002] used this approach, considering that a particle fulfilling a predefined tensile failure criterion could be replaced by a group of seven uniform particles. Tsoungui et al. [1999] also used this approach when modeling oedometric compression tests on granular materials, but they replaced the particles fulfilling the failure criterion with a group of 12 particles having 4 different sizes. Astrom and Herrmann [1998] also used this approach when studying fragmentation of granular media under pressure; they developed simulations using two different configurations for the generated fragments: splitting into two equal size circular fragments, and splitting into 12 circular fragments of 3 different sizes.

This study uses the second solution and a new simplified tensile failure criterion that can be easily implemented on DEM.

#### 4.3.2 Breakage criterion

The proposed simplified failure criterion considers:

- Only particles with a coordination number equal to or smaller than 3 are able to be broken. Particles break more easily when their coordination number is low [Tsoungui et al., 1999], [Lade et al., 1996], [Nakata et al., 2001a].
- For those particles having a coordination number smaller than or equal to 3, the real loading configuration such as the one presented in Fig.4.2(a) is assumed to be equivalent to the one

obtained in a diametrical compression test such as the Brazilian test, as shown in Fig.4.2(b). By using this simplification the induced tensile stress,  $\sigma_t$ , can be approximated with the expression presented on Fig.4.2(b), where  $P_1$  is the value of the highest contact force acting on the particle,  $L$  is the thickness of the disk (unit thickness for the simulated case), and  $D$  is the diameter of the disk. The induced tensile stress in Fig.4.2 (b) could be more severe than the stress induced in Fig.4.2 (a), but the author believes that the implemented simplification is justified due to the simplicity in the calculation of the induced tensile stress.

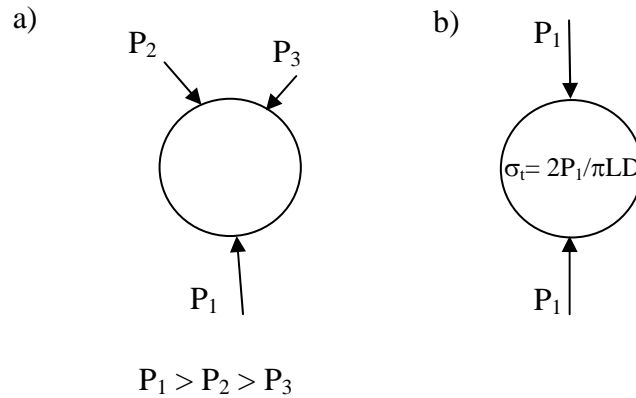


Figure 4.2 Equivalent load configuration and idealization of the induced tensile stress

- The tensile strength of a particle with a radius of 1mm is predefined as  $\sigma_{\max 1\text{mm}} = 3 \times 10^6$  Pa. This value was arbitrarily chosen by the author. It represents the strength of the virtual material. By changing this value, the necessary stresses to produce crushing will also change. It is assumed that the tensile strength of a particle with a radius  $r$ ,  $\sigma_{\max}(r)$ , is related to  $\sigma_{\max 1\text{mm}}$  according to the following relationship (where  $r$  is expressed in mm):

$$\sigma_{\max}(r) = \sigma_{\max 1\text{mm}} [r]^{-1} \quad (4.1)$$

In this way, particles with a radius greater than 1mm have a tensile strength smaller than  $\sigma_{\max 1\text{mm}}$ , and particles with a radius smaller than 1mm have a tensile strength greater than  $\sigma_{\max 1\text{mm}}$ . Other researchers have reported experimental results in order to describe the change in tensile strength as a function of size for different materials such as quartz fibers and sand grains [Billam, 1971], [Nakata et al., 2001b]. They found that the experimental results could be described using an equation similar in form to Eq.(4.1). As expected, the values of the two constants in Eq.(4.1) depend on the analyzed material. Eq.(4.1) is in agreement with the Weibull statistics for particle tensile strength as explained in Chapter 2.

- Every particle with a coordination number smaller than or equal to 3 is allowed to break if  $\sigma_t > \sigma_{\max}(r)$ .

#### 4.3.3 Fragmentation

The distribution of fragments produced by a tensile failure depends on the nature of the tested material [Nakata et al., 1999], [Takei et al., 2001]. For example, Fig.4.3(a) and Fig.4.3(b) show photographs of a real aggregate (a gravel particle) and a glass bead that were broken in diametrical compression tests (point load tests). The real aggregate broke down into a group of 7 particles having 3 different sizes, while the glass bead broke down mostly into a group of fragments of similar size. It was assumed that if a particle is fulfilling the previously established failure criterion, it is allowed to break into a group of 8 particles having 3 different sizes, as shown on Fig.4.3(c). This distribution of sizes resembles the one observed in crushed sugar (previous chapter) and is similar to the one observed for the real aggregate as indicated in Fig.4.3(a).

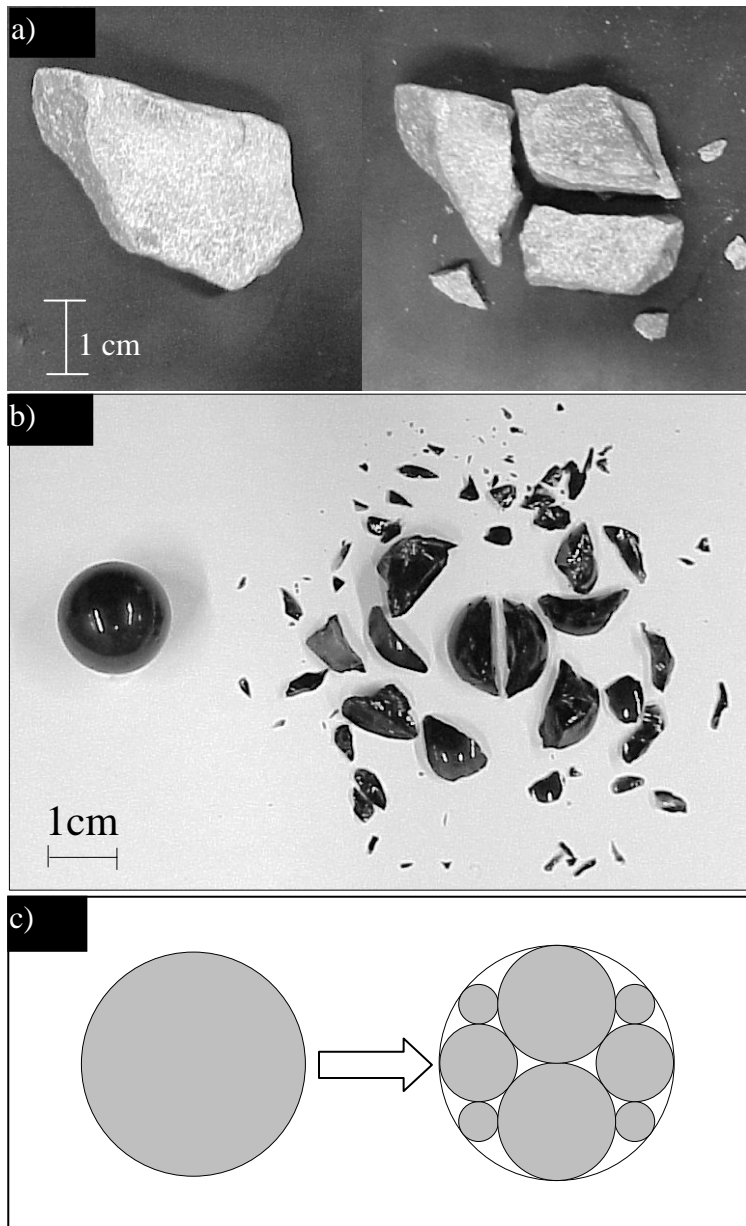


Figure 4.3 Fragments produced after a tensile failure of a real aggregate, a glass bead, and the idealized material.

#### 4.3.4 Applying the breakage criterion

In order to implement the failure criterion, a new subroutine (Remplazo) was programmed using the FISH language [Itasca, FISH in PFC]. This subroutine automatically checks whether a given particle is fulfilling the failure criterion. If it is, the particle that broke is deleted and replaced by the set of particles shown in Fig.4.3(c). The properties of the fragments are similar to the properties of the breaking particle. The subroutine does not restrict smaller particles from continuing to break.

Different generations of crushing are distinguished by the color of the particles. The subroutine assigns different colors to the particles depending if they are original particles of the simulation, come from previously original particles (first generation of crushing), come from fragments of original particles (second generation), come from fragments of fragments of the original particles (third generation), and so on.

The subroutine only needs to be called at the beginning of the simulation, and it automatically performs the required tasks. Thus, DEM codes such as PFC<sup>2D</sup> can now be enhanced allowing the possibility of particle breakage.

## **5.0 DEM SIMULATIONS OF THE LABORATORY TESTS**

This chapter presents DEM simulations of the laboratory tests presented in Chapter 3: confined uniaxial compression tests, direct shear tests, and ring shear tests. Also, simulations of biaxial tests are presented. These simulations allow the visualization of the evolution of crushing in granular materials under different conditions of stress and strain.

### **5.1 CONFINED UNIAXIAL COMPRESSION TEST**

#### **5.1.1 Configuration of the sample**

This simulation was intended to recreate how granular crushing evolves when a granular material is subjected to a confined uniaxial compression test. The first step was the construction of the simulated rectangular container. The simulated container had a width of 5cm and a height of 10 cm. It was composed by 4 different walls with a friction coefficient of 0.7. The normal and shear stiffness of these walls was set to  $1 \times 10^9$  N/m. After the construction of the container, 120 circular disks with unit thickness and a uniform radius of 3mm were generated inside. Their positions were randomly chosen by the program, with the limitation of no overlaps between particles. The density of the particles was set to 2500 kg/m<sup>3</sup>, their normal and shear stiffness was set to  $1 \times 10^8$  N/m, and their friction coefficient was set to 0.7.

After the disks were generated, they settled down and reorganized under the action of a normal gravity field (9.8m/s<sup>2</sup>). In this way, the sample had a loose structure at the beginning of the test. After this, the upper wall of the container started to move with a constant velocity of  $1 \times 10^{-7}$  m/step. After some

displacement, it made contact with the particles initiating the uniaxial compression. The velocity of the upper wall was constant during the test. This slow vertical velocity was chosen to guarantee that particles did not crush as a result of the rapid movement of the wall.

### 5.1.2 Evolution of crushing: void ratio

The loading stage started and the particles rearranged and started to crush as a result of the applied load. Fig. 5.1 shows the applied force vs void ratio curves for the upper and lower regions of the sample. Also, some snap shots of the sample are shown at different values of applied load. The first two particles that crushed were located in the middle and upper regions of the sample, and in general crushing concentrated in the upper region during the first stages of the simulation. It can be seen that almost every particle from the upper row was quickly broken. After these first stages, crushing started to spread into the middle region and ultimately into the lower region. This behavior is explained by the fact that the upper particles had to bear large loads and their coordination numbers were low since they were closer to the walls. Also, since friction forces were developed at the vertical walls of the container, the top part of the sample carried the full applied load, while the bottom part carried a lesser amount.

The void ratio curves present two different regions. The first one is characterized by a small decrement in void ratio while the second one is associated with an important decrement in void ratio. In other words, small values of deformation are associated with the first region and large values are associated with the second region. The transition between these two regions corresponds to an applied vertical force between  $2 \times 10^4 \text{N}$  and  $3 \times 10^4 \text{N}$ , and is related to the starting of crushing. The change in void ratio in the first region can be explained by the rearrangement of the original particles while the change in void ratio in the second region is the product of particle breakage and the produced rearrangement of the original particles and fragments. This is in agreement with the experimental results presented in Chapter 3, and those reported by several authors (Chapter 2).

As shown on Fig.5.1, the values of the void ratio in the upper part of the sample were always smaller than the values in the lower part. This is consistent with the fact that most of the crushing and consequently the reduction in volume of voids took place in the upper part. Hence, crushing is a phenomenon that must be studied by regions inside the sample since it is not uniformly distributed. Engineering properties of a crushable granular material will be affected differently depending on the analyzed region of the sample. For example, by only looking the snap shots one can get an idea of how different the hydraulic conductivity of the upper and lower parts could be.

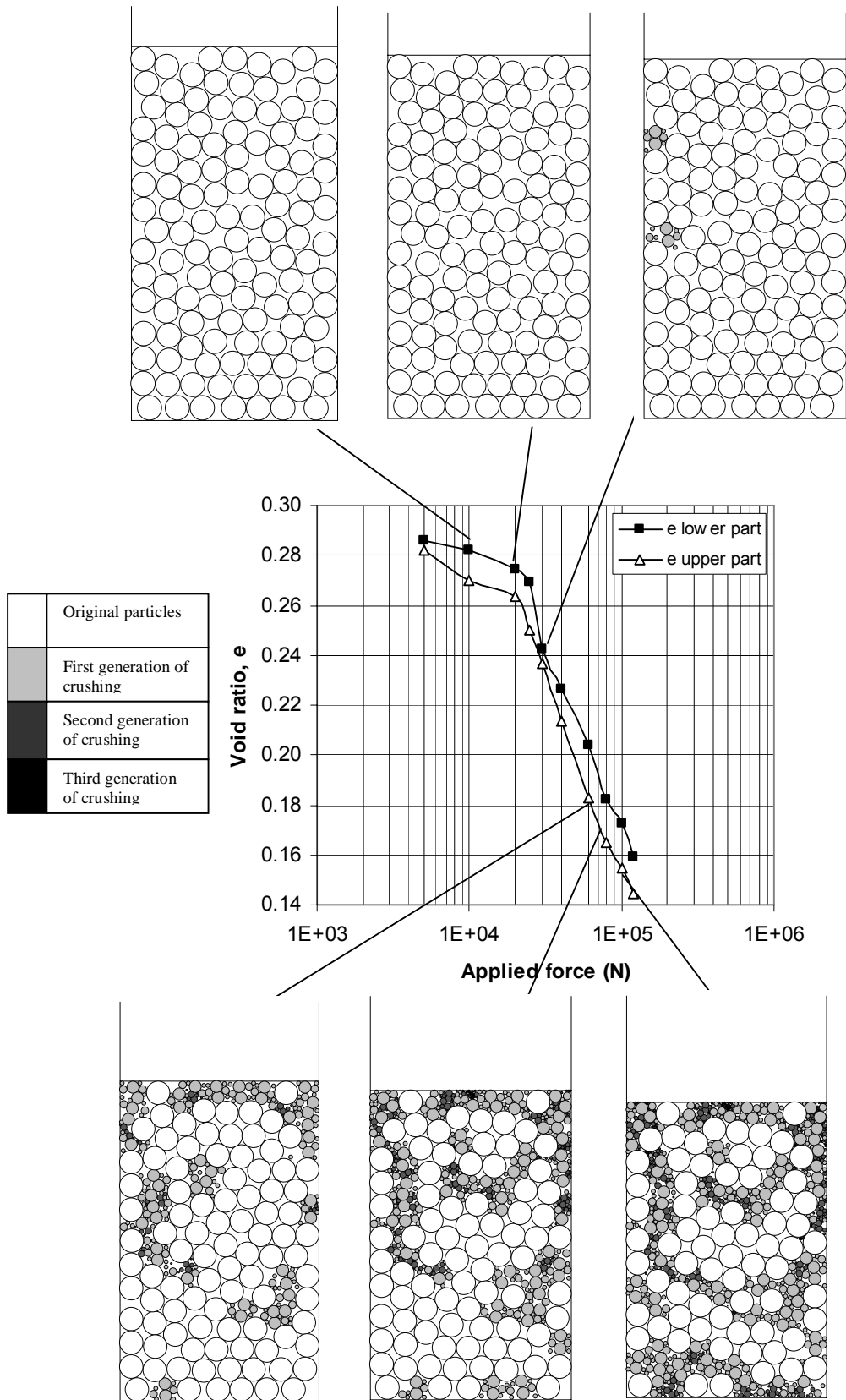


Figure 5.1 Crushing evolution, confined uniaxial compression test.

Fig 5.2 shows some amplified details from the sample at different values of applied vertical force. It can be observed how the produced fragments reorganized forming a dense structure. If several of these dense zones interconnect with each other, the drainage capacity of the granular material will be severely affected.

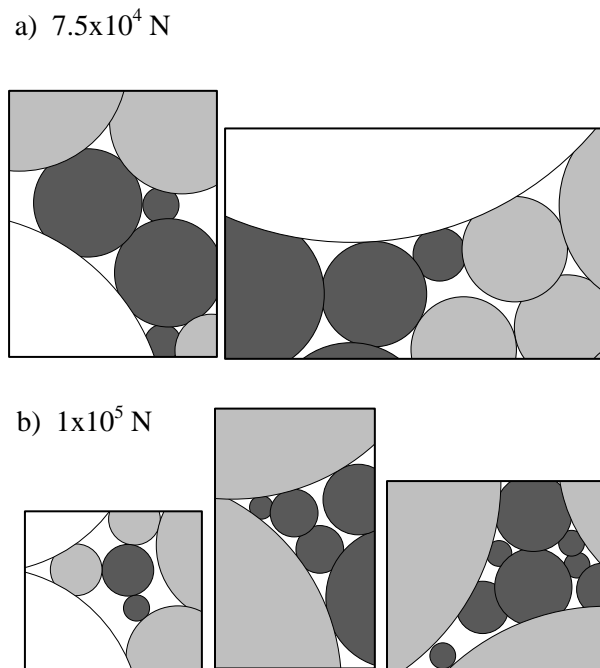


Figure 5.2 Details of the pore structure at different values of vertical force

### 5.1.3 Evolution of crushing: particle size distribution

The snap shots presented in Figs.5.1 and 5.2 show how the simulated group of particles evolved from a uniform granular material into a well graded mixture of sizes. Eq.(2.1) was used to analyze the evolution of the particle size distribution of the simulated sample. The final results are shown in Fig.5.3.

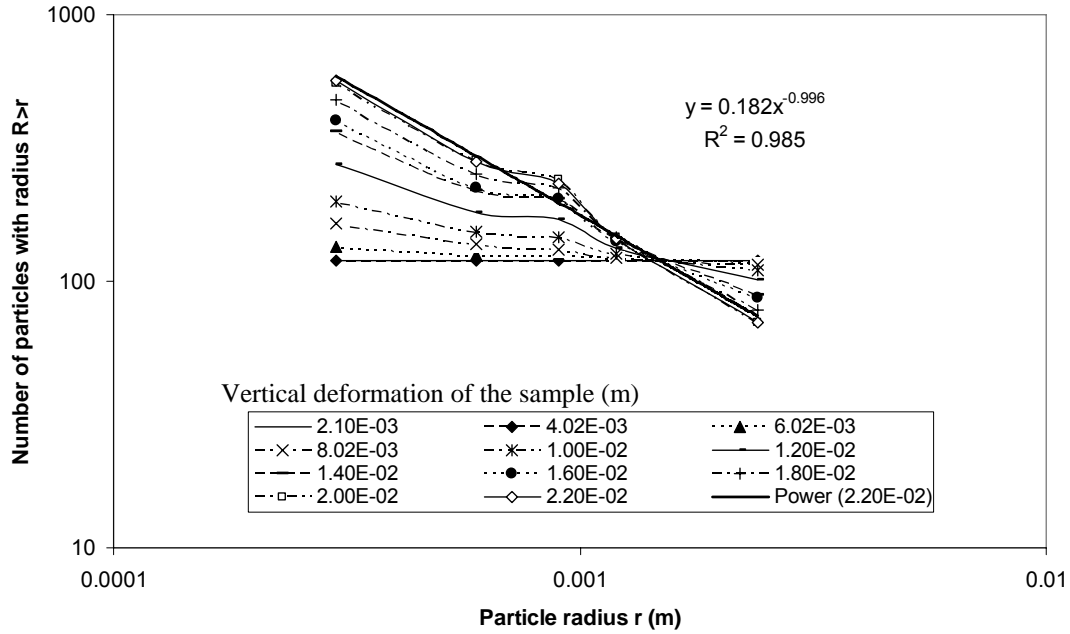


Figure 5.3 Evolution of the particle size distribution, confined uniaxial compression test

Fig.5.3 shows the particle size distribution of the sample as a function of the induced vertical deformation. It also includes the power regression line for the distribution obtained at the end of the simulation. The higher value obtained for  $R^2$  in the power regression shows that the obtained distribution was fractal, as suggested by other researchers (Chapter 2). However, it can be noted that the obtained fractal dimension from this power regression was equal to 0.996. The maximum fragmentation fractal dimension in a two dimensional case is 1.5, which is equivalent to the 2.5-2.6 value reported for a three dimensional case ( $D_{f3D} = D_{f2D} + 1$ ). Even though the sample was evolving into a well distributed mixture of sizes, it was still some how being dominated by the original particles.

#### 5.1.4 Evolution of crushing: experimental validation of the concentration of crushing

The results presented thus far satisfactorily agree with the experimental results reported in Chapter 3 and those reported by other researchers. However, it was necessary to corroborate that particle breakage does not evolve uniformly throughout the sample, but rather concentrates in the upper region.

Experimental tests conducted by Dr. Luis F. Vesga at the University of Pittsburgh are presented to validate the results from the simulation. Confined uniaxial compression tests were carried out using an uniform sand that passed the sieve No. 10 and was retained on the sieve No. 20 (coefficient of uniformity equal to 1.65). The specific gravity of this sand was equal to 2.65. The container used for this test was cylindrical in shape, having an internal diameter of 5cm and a height of 8cm. Different samples of the same sand were loaded to different vertical stresses, ranging in value between 1 and 20 MPa. Grain size distribution analyses were carried out after the tests.

Fig.5.4 shows the applied vertical stress vs. void ratio curve for the sample subjected to the maximum vertical stress. This figure shows the same trend observed during the computer simulation. It can be noted that a yield stress between 2 MPa and 4 MPa defines the change of behavior.

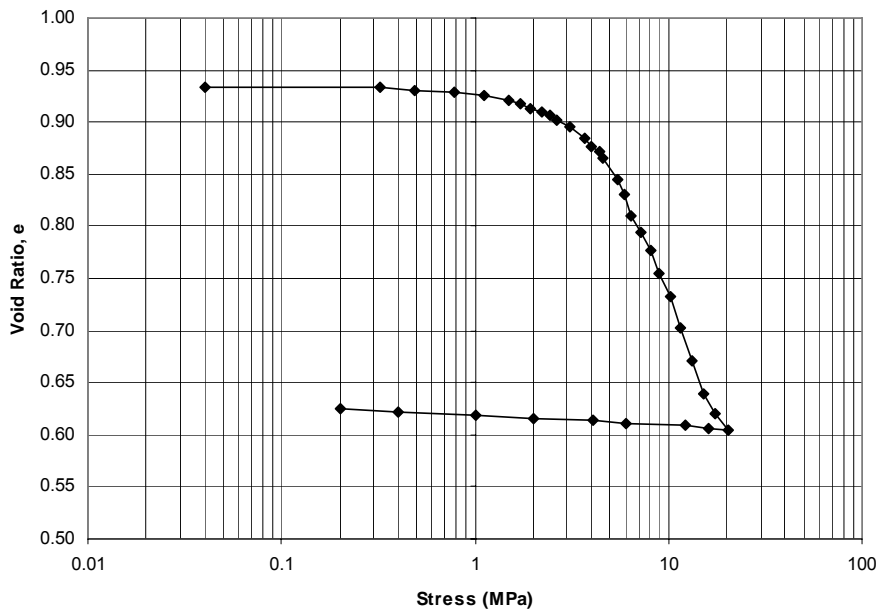


Figure 5.4 Void ratio vs applied vertical stress, sand (tests conducted by Vesga, L.F. at the University of Pittsburgh)

Since the initial material was uniform in size, a percentage of crushing was defined as the percentage by weight of the sample after the test that passed through the sieve that originally retained all

the material. Fig.5.5 shows how the different layers of the samples had different levels of crushing, displaying the same trend observed before on the computer simulation.

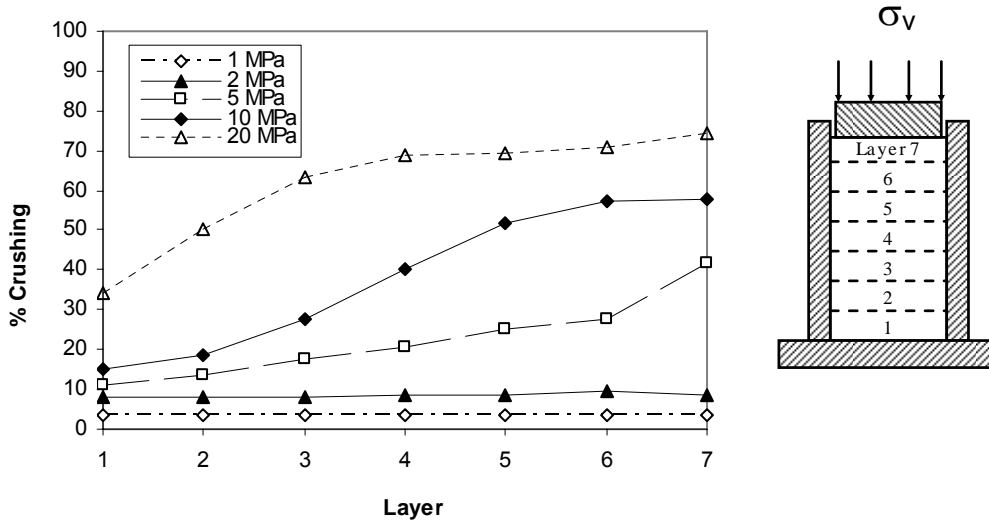


Figure 5.5 Layered analysis, sand.  
(tests conducted by Vesga L.F. at the University of Pittsburgh)

In summary, Fig.5.4 and Fig.5.5 show that by applying a vertical stress greater than the yield stress, crushing is produced inside the sample. It must be noted that for every applied stress, more crushing took place in the upper layers than in the middle and lower layers of the sample. This phenomenon was very important when crushing was just starting. As crushing evolved, the different layers tended to present similar levels of fragmentation. These results validate those obtained during the computer simulation.

## 5.2 DIRECT SHEAR TESTS

Two computer simulations are presented to simulate the behavior of a crushable material when loaded under direct shear test conditions. During the first simulation the sample was subjected to a low value of vertical stress, and only one particle crushed during the simulated test (including both uniaxial compression and shearing stages). Conversely, during the second simulation the applied vertical stress was much higher, and several particles were broken. Both simulations were carried out using the same simulated shear box and the same simulated granular material.

### 5.2.1 Configuration of the samples and sequence of the simulated direct shear tests

The first step was the construction of the shear box. The box had a width of 6cm and a height of 3 cm. The shear and normal stiffness of the frictionless walls forming the box were set to  $1 \times 10^9$  N/m. After the construction of the box, 48 circular particles were generated. The simulated disks had the same properties used for the confined uniaxial compression test, and only the number of disk was different. Their positions were randomly chosen by the program, having the limitation of no overlaps between particles. A normal gravity field ( $9.8 \text{m/s}^2$ ) was used during the simulations. The two simulations presented in this study started from here with the same set up, including the same structure of the simulated granular material.

The two tests started by vertically moving the top wall of the upper section of the shear box until a specific vertical applied force was obtained. The first test used a force equal to  $1.6 \times 10^4$  N, the second test used a force of  $3 \times 10^4$  N. The first test used a force that produced a vertical stress in the material that was less than its yield stress. The second test induced a vertical stress greater than the yield stress of the material. The yield stress was defined as the vertical stress that causes the initiation of particle crushing

as visualized in the DEM results. The specific applied vertical force was constant during the remaining part of the simulations. This was accomplished by using a servo-controlled mechanism that was programmed using the FISH language [Itasca, FISH in PFC 2002]. After the applied vertical force was set to a constant value, the shearing stage started by moving the upper section of the shear box to the left with a constant velocity of  $5 \times 10^{-8}$  m/step. The applied shear stress was continuously monitored, and the tests were ended when the horizontal displacement of the upper part of the box was equal to 5mm.

### 5.2.2 Crushing and porosity evolution

As mentioned before, the tests started by applying a constant vertical force to the samples. Only one particle of the sample subjected to  $3 \times 10^4$  N crushed at this stage of the simulation, while no particle breakage was observed for the sample subjected to  $1.6 \times 10^4$  N. After this first stage of uniaxial compression, the shearing stage started by moving the upper part of the shear box with a constant velocity of  $5 \times 10^{-8}$  m/step. Figs.5.6 and 5.7 show the measured porosities of the left and right sides of the samples at different moments of the simulations. Also, some snap shots of the samples are shown at different values of horizontal deformation.

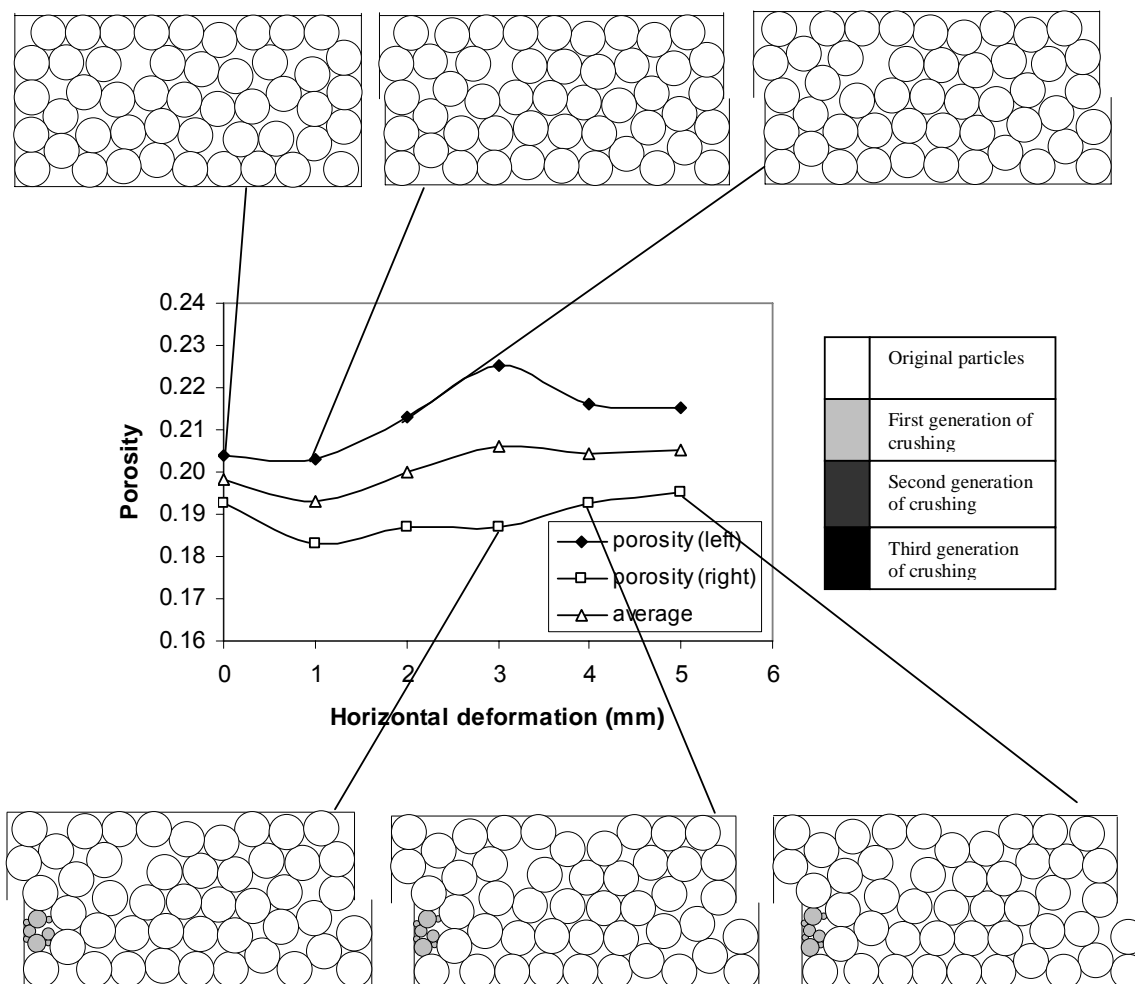


Figure 5.6 Porosity and crushing evolution of the simulated granular material (vertical force =  $1.6 \times 10^4$  N)

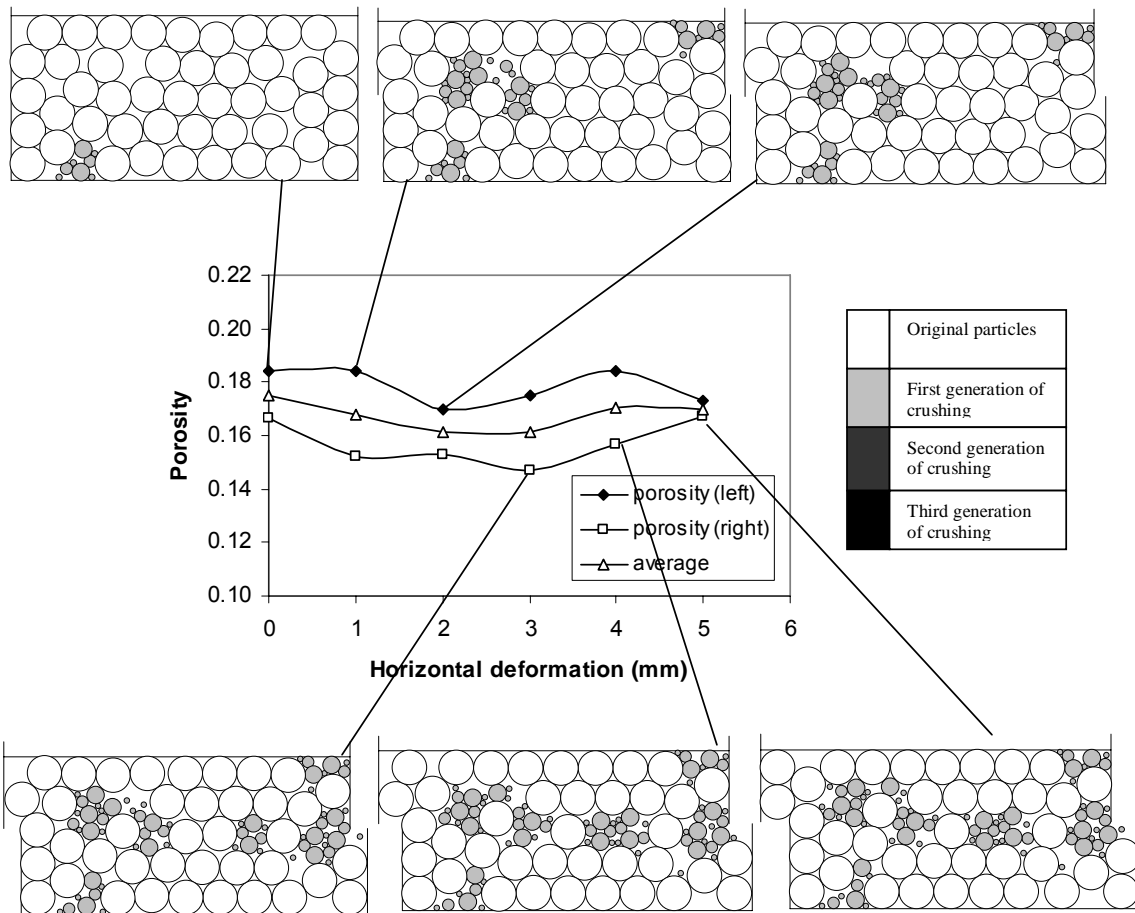


Figure 5.7 Porosity and crushing evolution of the simulated granular material (vertical force =  $3 \times 10^4$  N)

Fig.5.6 shows that only one particle was broken during the simulation with the lower value of applied vertical force. This particle was located at a height close to the middle of the shearing zone, and it was in contact with the left wall of the lower part of the shear box. On the other hand, Fig.5.7 shows that several particles were crushed during the simulation with the higher value of applied vertical force. Two of the first particles that crushed were in contact with the horizontal walls of the shear box. These particles had to bear large loads and their coordination numbers were low due to the imposed geometrical constraints. The other particles that crushed were located in the middle of the shearing zone. As a consequence of the induced displacement, the coordination number of the particles in this region continuously changed, creating a dangerous situation since they transmitted large forces due to the applied shear stress. Thus, the particles in the middle of the shearing zone were very prone to break.

Fig.5.6 shows that the porosities of the left and right parts of the sample subjected to a constant vertical force of  $1.6 \times 10^4 \text{ N}$  had similar trends during the initial deformation of the sample. The porosity of the left part of the sample was always higher than the porosity of the right side. This was expected since the porosity of the left part was slightly greater than the porosity of the right side at the beginning of the uniaxial compression stage. Between the starting of the shearing stage and a horizontal deformation of 1mm, the sample presented a contracting behavior with a slight decrement in porosity. After this, the sample started to dilate. Between a horizontal deformation of 1mm and 3mm, the porosities of the left and right parts of the sample strongly increased as a result of this dilating behavior. A careful observation of Fig.5.6 shows that the upper horizontal wall moved slightly upward. This movement is a clear indication that the sample experienced dilation. After a horizontal deformation of 3mm, the right and left parts of the sample presented different behaviors. The right part of the sample continued to experience a dilating behavior for the remainder of the test, while the left part experienced contraction as a result of the breakage of one particle. In general, the results presented in Fig.5.6 show that the simulated granular material had a structure that tended to dilate as a result of shearing.

Fig.5.7 shows that the porosities of the left and right parts of the sample subjected to a vertical force of  $3 \times 10^4 \text{ N}$  followed a similar trend during the simulation. As explained before, the porosity of the

left part of the sample was always higher than the porosity of the right side because of the initial arrangement of the particles. The dilating behavior identified in Fig.5.6 was somehow suppressed by the generated particle crushing, and as a result of these two effects, the porosities fluctuated, maintaining an almost constant value. This phenomenon is similar to what happens during some triaxial tests on crushable materials where the compressive behavior due to particle crushing is counteracted by the dilating behavior due to particle rearrangement, as explained by Coop et al. [2004].

### 5.2.3 Evolution of the grain size distribution

The snapshots presented in Fig.5.7 show how the simulated group of particles from the sample subjected to a vertical force of  $3 \times 10^4$  N evolved from a uniform granular material into a well graded mixture of sizes. Eq.(2.1) was used to analyze the evolution of the particle size distribution in the simulated sample. The final results are shown in Fig.5.8. This figure shows the particle size distribution of the sample as a function of the induced horizontal deformation. It also includes the power regression line for the distribution obtained at the end of the simulation. The higher value obtained for  $R^2$  in the power regression shows that the distribution obtained as a result of crushing was fractal. However, the fragmentation fractal dimension obtained from this power regression is equal to 0.492 that is almost one third of the maximum possible value equal to 1.5 (two dimensional arrangement). Even though the sample was evolving towards a well distributed mixture of sizes, it was still being dominated by the original particles. The sample could experience more crushing as a result of an increment in the vertical stress or an increment in the induced deformation.

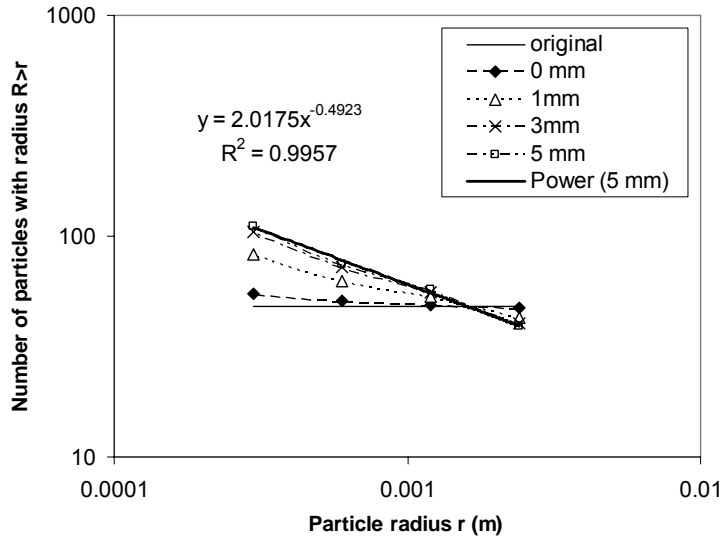


Figure 5.8 Evolution of the particle size distribution during the simulated direct shear test

#### 5.2.4 Shear strength

Fig.5.9 and Fig.5.10 show the applied shear stress as a function of the induced horizontal displacement for the two simulated tests. These curves present some spike drops as a result of particle crushing and particle rearrangement. Forces are transmitted at the contacts of the particles, and if particle crushing or particle rearrangement takes place, a momentary loss in strength will take place and will be reflected in the figures as a spike drop.

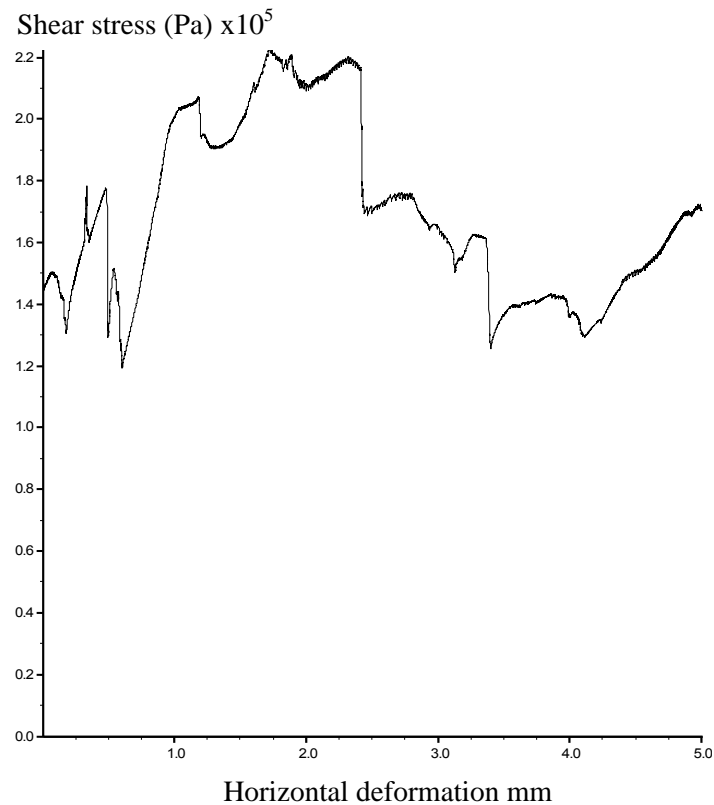


Figure 5.9 Induced horizontal displacement vs. applied shear stress, vertical force=  $1.6 \times 10^4$  N

Fig.5.9 shows the results of the test with the applied vertical force of  $1.6 \times 10^4$  N. A maximum shear strength of  $2.237 \times 10^5$  Pa took place at a horizontal displacement of 1.75mm. The corresponding applied vertical stress at this deformation was  $2.747 \times 10^5$  Pa. The maximum friction coefficient was calculated as the ratio between the maximum applied shear stress and the corresponding normal stress. Thus, a maximum friction coefficient of 0.814 was obtained. It must be noted that this maximum friction coefficient represents the friction coefficient of the sample and is higher than the fundamental friction coefficient of 0.7 that was specified for each individual particle.

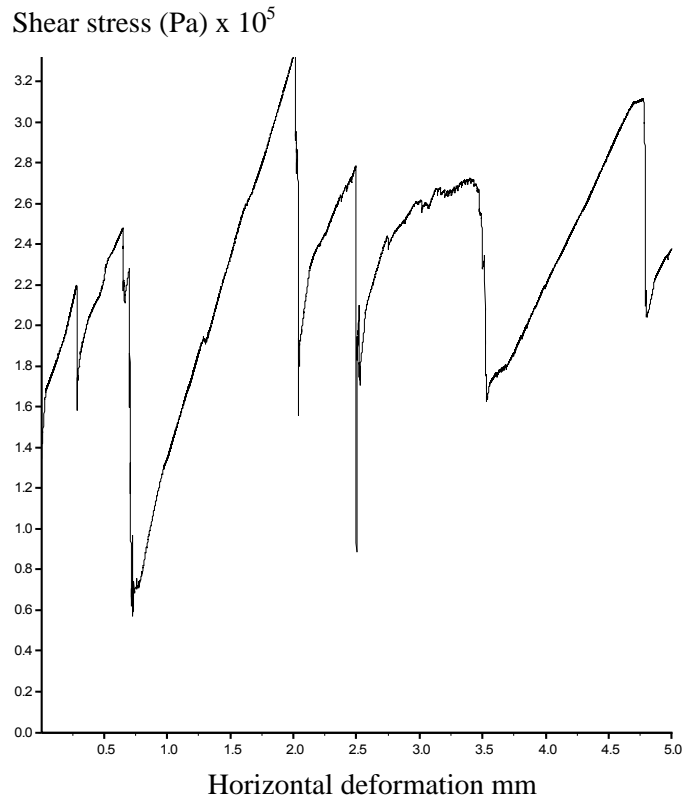


Figure 5.10 Induced horizontal displacement vs. applied shear stress, vertical force=  $3 \times 10^4$  N

Fig.5.10 shows the results of the test with the applied vertical force of  $3 \times 10^4$  N. A maximum shear strength of  $3.36 \times 10^5$  Pa was recorded at a horizontal displacement of 2mm. At this level of deformation the applied vertical stress was equal to  $5.172 \times 10^5$  Pa. Thus, a maximum friction coefficient of 0.65 was obtained. After the sample reached the maximum value of shear strength, more particle crushing took place in the middle of the shearing zone, and spike drops continued to characterize the displacement- shear strength curve. A comparison of the maximum friction coefficients from the two tests shows that the friction coefficient of the simulated granular material decreased as a result of particle crushing. Moreover, the results from Fig.5.10 illustrate that a reduction in shear strength was produced as a consequence of crushing. All this is in agreement with the experimental results previously presented by other researchers (Chapter 2).

### 5.3 RING SHEAR TESTS

Ring shear tests conducted on weak granular materials have shown to be a valuable tool used to understand the evolution of crushing. Previous researchers have conducted ring shear tests on weak granular materials such as carbonate sand [Luzzani and Coop, 2002], [Coop et al., 2004]. Their results satisfactorily agree with those presented in Chapter 3. Two interesting features have been identified: (a) the grain size distribution of the original material evolves towards a stable fractal distribution as a consequence of particle breakage; however, this stable fractal distribution of sizes depends on the magnitude of induced stresses and the initial grading of the sample. (b) the mobilized angle of shearing resistance does not significantly change regardless of the severe degradation of the sample.

One disadvantage of using ring shear tests in the laboratory is that they do not easily allow a visualization of the crushing process. Numerical simulations in the form of DEM have been used to overcome this constrain. Since the original DEM does not consider particle breakage, different solutions have been proposed and programmed using DEM codes:

- a. The first solution is to develop several ring shear simulations considering different grain size distributions. In this way, each grain size distribution represents a different state in the evolution of crushing [Morgan, 1999], [Morgan and Boettcher, 1999].
- b. The second solution is to treat each granular particle inside the ring shear as an agglomerate built by bonding smaller particles, which is defined as a cluster [Jensen et al., 2001]. Following certain criteria, this cluster can fully or partially disaggregate during the simulation.

- c. A third solution to this problem consists on replacing the particles that are fulfilling a predefined failure criterion with an equivalent group of smaller particles [Lang, 2002]. This approach was used to simulate ring shear tests on a crushable granular material.

### 5.3.1 Configuration of the samples

The first step was the construction of the virtual ring shear apparatus. A simulated box having 15cm in width and 6cm in height was created. The top and bottom walls simulate rough walls with a wave length of 2.5cm and a difference in height between peaks of 0.5cm. Their coefficients of normal and shear stiffness were set to  $1 \times 10^9$  N/m, and their friction coefficients were set to 0.7. Originally these two walls were separated by a vertical distance of 6cm before the generation of the particles. Horizontal periodic boundaries were programmed by the author using the FISH language. When using periodic boundaries, particles located at one side of the sample interact with particles located at the opposite side. Moreover, particles are allowed to exit from one side of the sample entering at the same height on the other side. This technique has been used before by many researchers using DEM codes [Morgan and Boettcher, 1999], [Jensen et al., 1999], [Jensen et al., 2001], [Lang, 2002], [Morgan, 2004].

Three simulations were conducted. The samples used on the simulations came from the same original sample. This original sample was created by generating 230 circular discs inside the simulated ring shear apparatus. The properties of these discs were exactly the same used before for the simulated confined uniaxial test and the direct shear tests. Their positions were randomly generated by the program with no overlaps between discs. The discs were allowed to settle and reorganize under the action of a gravity field ( $g = 9.8\text{m/s}^2$ ). Thus, the original sample had a loose structure. This original sample was recorded, and was the starting point for the three simulations. For the first two simulations, a vertical force of  $1 \times 10^5\text{N}$  was applied by moving downwards the upper wall of the simulated ring shear. The only difference is that particle crushing was only allowed during the second simulation. The applied vertical force was constant for the remaining part of the simulated tests. The shear stress was induced by moving

the upper wall of the simulated ring shear to the left with a constant velocity of  $5 \times 10^{-7}$  m/step. The third simulation started from the sample composed by breakable particles after the vertical force of  $1 \times 10^5$  N was applied but before the shearing stage. The applied vertical force was increased up to a value of  $1.5 \times 10^5$  N, and was constant for the remainder of this simulation. Similar to the other two simulations a constant velocity of  $5 \times 10^{-7}$  m/step was used to induce the shear stress.

### 5.3.2 Evolution of porosity and friction coefficient of the sample composed by unbreakable particles

Fig.5.11 shows the mobilized friction coefficient, the average porosity, and some snap shots at different levels of deformation of the sample composed by unbreakable particles. A vertical strip of particles located at the middle of the sample was marked with dark grey color so the deformation of the granular media could be traced. It can be noted how the mobilized friction coefficient fluctuated maintaining a constant average value equal to 0.3. This fluctuation can be attributed to particle rearrangement during the shearing process. Since the sample was composed by uniform particles, every time that the particles reorganized or locked with each other, the shear resistance of the sample decreased or increased respectively. Thus, as presented by Morgan [1999] more variations are expected to occur when using a uniform granular material rather than a well graded material. The porosity of the sample also fluctuated, roughly maintaining a constant value close to the initial porosity of the sample after the application of the vertical load (0.199).

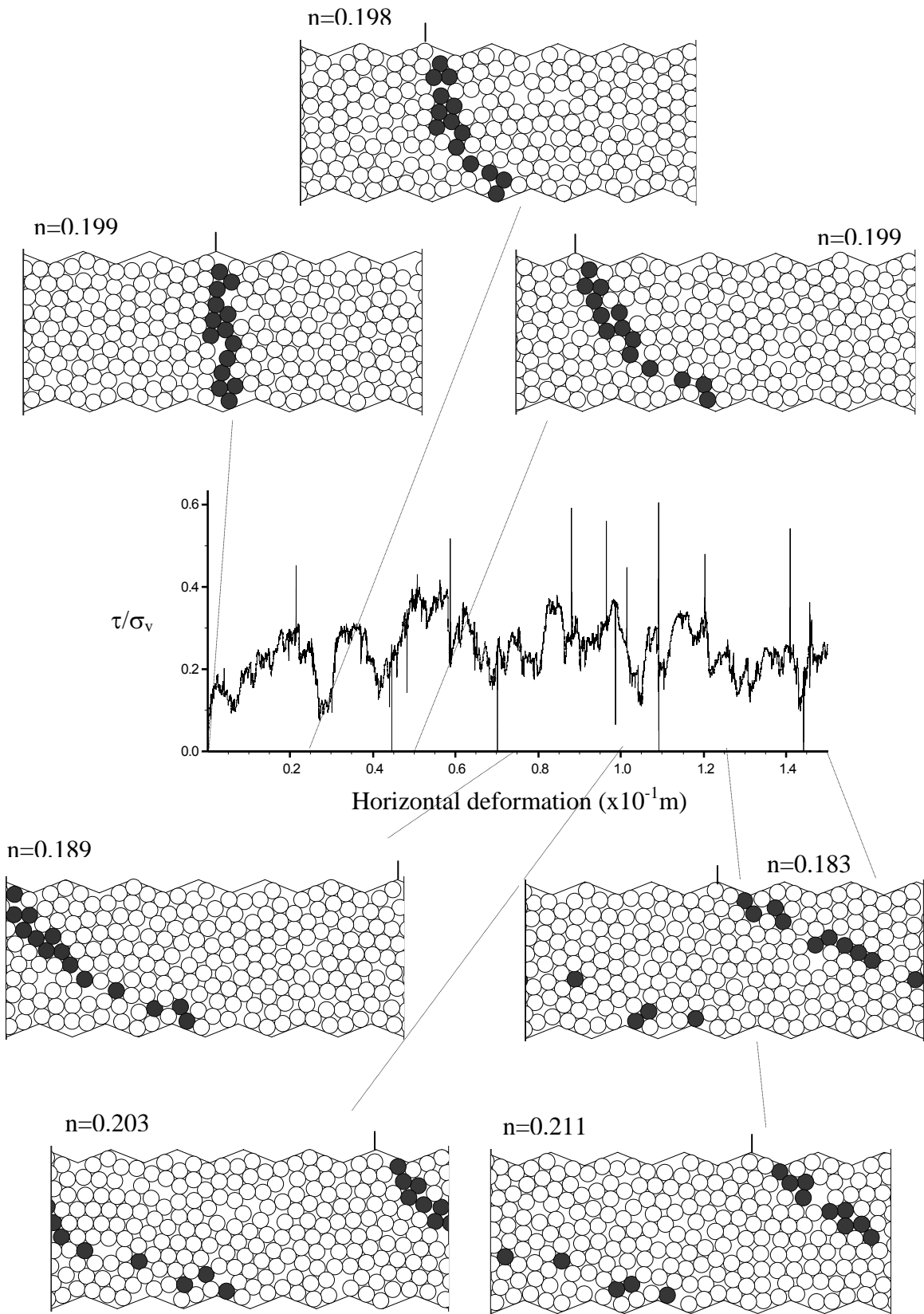


Figure 5.11 Sample composed by unbreakable particles

### 5.3.3 Evolution of crushing, porosity, and friction coefficient: sample composed by crushable particles, vertical force= $1 \times 10^5 \text{N}$

Fig.5.12 shows the mobilized friction coefficient, the average porosity, and some snap shots at different levels of deformation of the sample composed by crushable particles and subjected to a vertical force of  $1 \times 10^5 \text{N}$ . It can be noted how the mobilized residual friction coefficient exhibited a constant value regardless of the severe and progressive degradation of the sample. This is in agreement with the experimental results obtained in Chapter 3 and those obtained by Coop et al. [2004]. An average value for the residual friction coefficient was equal to 0.3, which is consistent with the results obtained during the first simulation.

The porosity of the sample significantly decreased from 0.175 to 0.153 due to particle crushing and particle rearrangement between horizontal deformations of 0 and 5cm. After this, a very small dilation (porosities between 0.153 to 0.157) was produced due to particle rearrangement between horizontal deformation of 5cm and 10cm. Finally, the sample slightly contracted between horizontal deformations of 10cm and 15cm (porosities of 0.157 and 0.149 respectively). The interaction between contractancy due to particle crushing and dilatancy due to particle rearrangement is far from simple, since both phenomena takes place at the same time. It is complicated to conclude if the sample reached a critical state by only looking the porosities of the sample since an almost constant value of porosity could be the balanced effect between contraction due to crushing and dilation due to particle rearrangement.

It can be observed how different generations of crushing coexist inside the sample, and some of the original particles were surrounded and protected by smaller particles. The grain size distributions of the sample at different values of horizontal deformation were analyzed using Eq.(2.1). The results are presented in Fig.5.13. Also, a power regression line was added to the data corresponding with a horizontal deformation of 15cm. The obtained fragmentation fractal dimension was equal to 1.057. This value of fragmentation fractal dimension in this two dimensional arrangement corresponds with an equivalent

value of 2.057 in a three dimensional case ( $D_{f\ 3D} = D_{f\ 2D} + 1$ ). Thus, the simulated sample achieved a fragmentation fractal dimension equivalent to the maximum value obtained in the laboratory ring shear tests presented in Chapter 3.

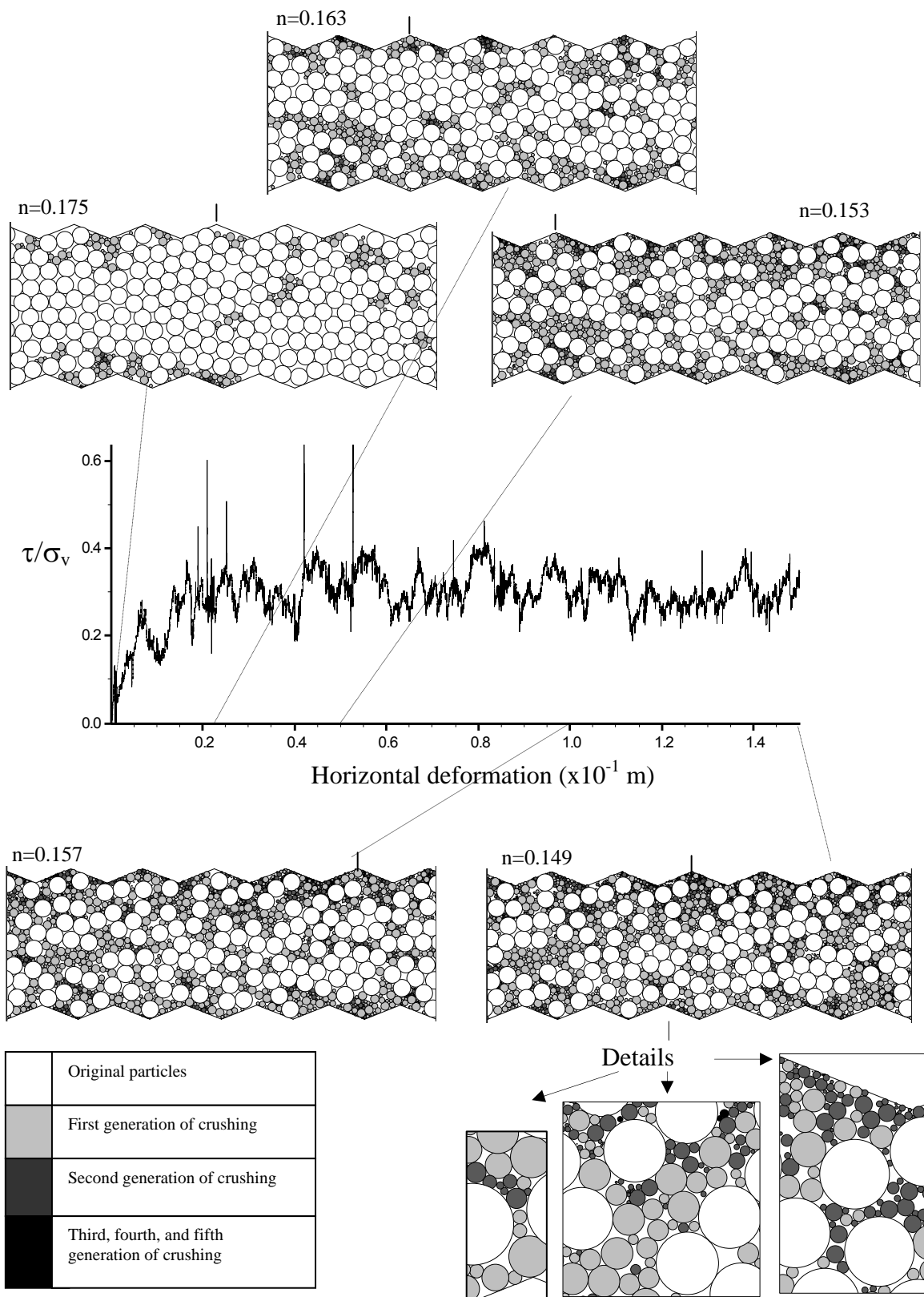


Figure 5.12 Sample composed by breakable particles, vertical force=  $1 \times 10^5$  N

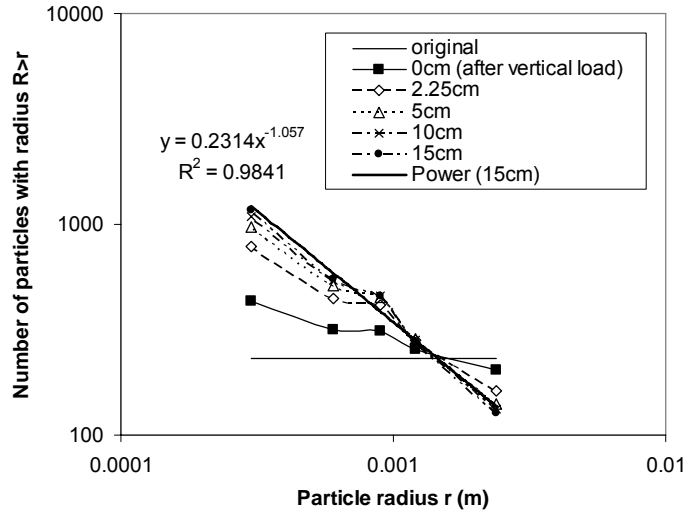


Figure 5.13 Evolution of the particle size distribution, vertical force:  $1 \times 10^5 \text{N}$

Fig.5.14 shows the evolution of the fragmentation fractal dimension. The sample presented an almost constant fractal dimension between horizontal deformations of 7.5cm and 15cm. Crushing seems to have ceased at these values of deformation. However, a very small amount of crushing was still occurring in the sample, as is shown in this figure.

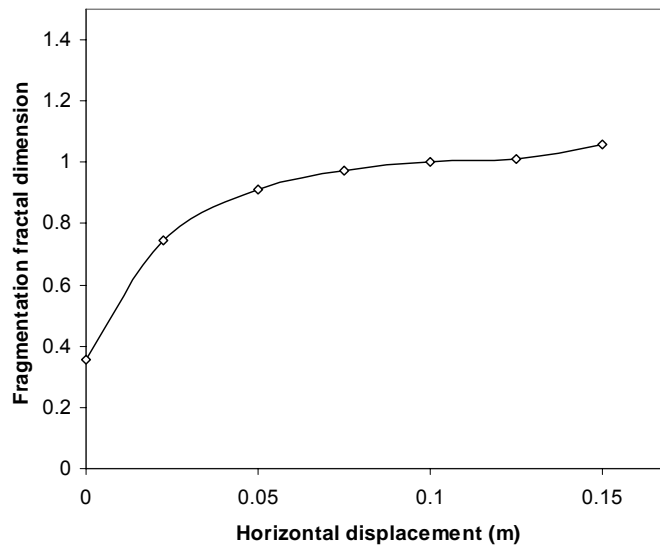


Figure 5.14 Evolution of the fragmentation fractal dimension, vertical force:  $1 \times 10^5 \text{N}$

The results of the porosities at different values of horizontal deformation and the results from Fig.5.14 show that the sample tended to achieve an almost steady state after a horizontal deformation of 7.5cm since the changes in porosity and grain size distribution were very small. Nevertheless, it should be noted that a critical state was not completely achieved since the sample continued to experience a very small amount of crushing even at very large deformations.

5.3.4 Evolution of crushing, porosity, and shear strength: sample composed by crushable particles, vertical force=  $1.5 \times 10^5 \text{N}$

Fig.5.15 shows the applied shear force, the average porosity, and some snap shots at different levels of deformation of the sample subjected to a vertical force of  $1.5 \times 10^5 \text{N}$ . The applied shear force exhibited an almost constant value of  $0.45 \times 10^5 \text{N}$  regardless of the severe and progressive degradation of the sample. Thus, the average residual friction coefficient was again equal to 0.3 ( $0.45 \times 10^5 \text{N} / 1.5 \times 10^5 \text{N}$ ). This is in agreement with the results from the other two simulations, the experimental results obtained in Chapter 3, and those obtained by Coop et al. [2004].

The porosity of the sample significantly decreased from 0.166 to 0.139 due to particle crushing and particle rearrangement between horizontal deformations of 0 and 5cm. After this, the porosity continued to decrease but at a very small rate (from 0.139 to 0.130 in 5cm of horizontal deformation). The higher applied vertical force precluded the occurrence of dilatancy. Fig.5.16 shows the results of applying Eq.(2.1) to the particle size distributions of the sample at different values of horizontal deformation. A maximum value of fragmentation fractal dimension equal to 1.1484 (Equivalent to 2.1484 in 3D) was achieved by the sample at the end of the simulation. More crushing occurred during this simulation than during the second one. This is reflected in the fact that the fragmentation fractal dimension was higher than the one obtained during the second simulation (2.1484 vs. 2.057). This is in agreement with the laboratory results presented in Chapter 3.

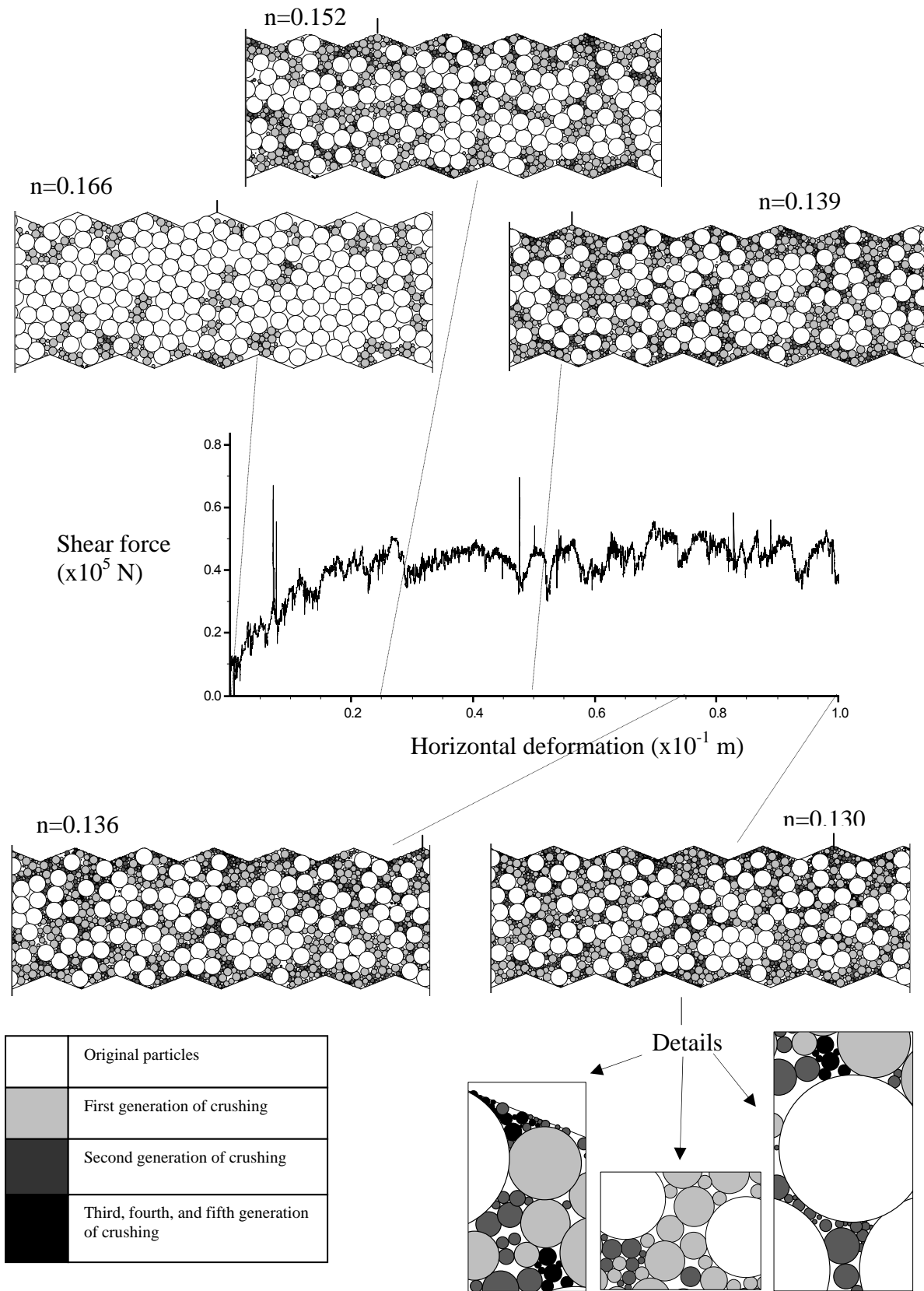


Figure 5.15 Sample composed by breakable particles, vertical force=  $1.5 \times 10^5 \text{ N}$

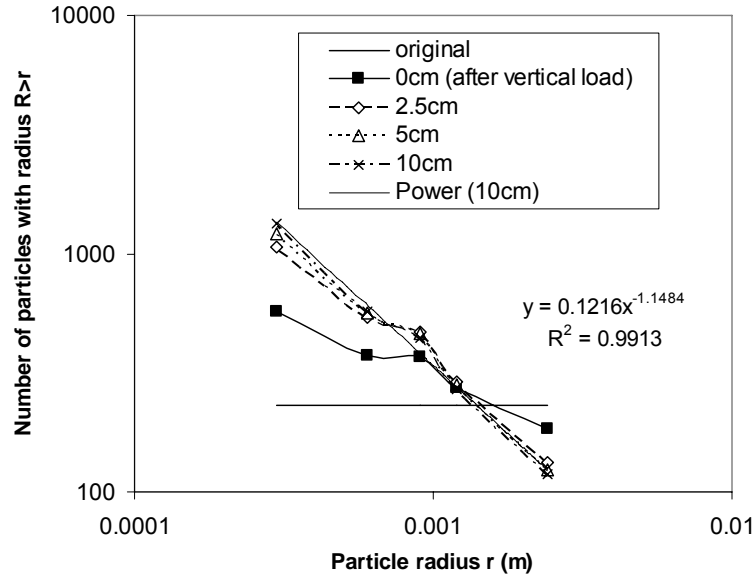


Figure 5.16 Evolution of the particle size distribution, vertical force:  $1.5 \times 10^5 \text{N}$

Fig.5.17 shows the evolution of the fragmentation fractal dimension during the simulation. It can be noted that the sample achieved an almost constant fragmentation fractal dimension at a horizontal displacement of 5cm.

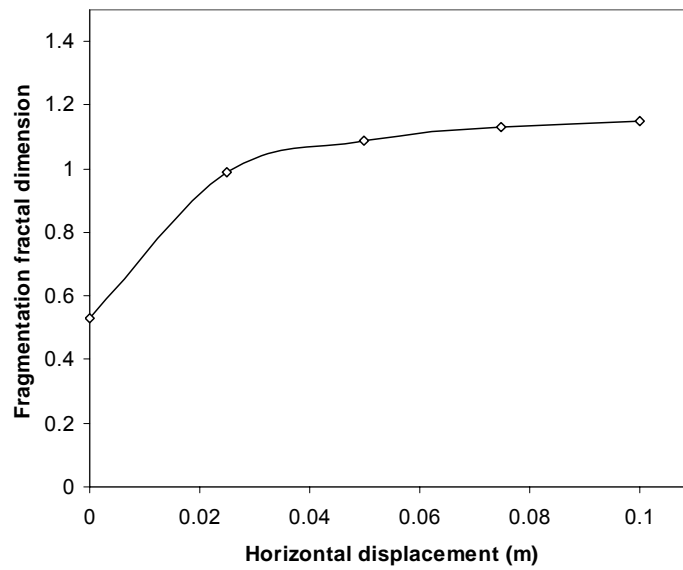


Figure 5.17 Evolution of the fragmentation fractal dimension, vertical force:  $1.5 \times 10^5 \text{N}$

A comparison of Fig.5.15 and Fig.5.17 shows that the sample reached an almost steady state at a horizontal deformation of 5cm since the changes in porosity and fragmentation fractal dimension were considerably small after this deformation. Nevertheless, it should be noted that a critical state was not completely achieved since the sample continue to experience a very small amount of crushing even at very large deformations.

## 5.4 BIAXIAL TESTS

Biaxial tests were not carried out in the laboratory due to technical difficulties. Nevertheless, DEM simulations were developed since there is a significant amount of experimental results that have been obtained by other researchers in the past and can be used for comparison.

### 5.4.1 Configuration of the samples and sequence of the simulated biaxial tests

The biaxial box had originally a width of 5cm and a height of 13cm. The horizontal walls had a total length of 7cm, so the biaxial box could expand horizontally. The shear and normal stiffness of the walls forming the box were set to  $1 \times 10^9$  N/m. These walls were assumed to be frictionless. The vertical walls were allowed to move horizontally in opposite directions in order to control the applied horizontal stress. The upper horizontal wall was allowed to move vertically in order to control the applied vertical stress. In this way, the applied principal stresses were controlled using a FISH servo-mechanism programmed by the author. Both vertical and horizontal stresses were calculated as the average between the applied stresses on the two opposite walls. It should be noted that in the PFC<sup>2D</sup> software, walls forming a box can be designed so they do not interact [Itasca, Theory and Background, 2002]. For example in the biaxial test the movement of the upper horizontal wall is not influenced by the movement of the two vertical walls. Thus, they can overlap with no interaction.

After the construction of the box, 165 discs were generated inside. Their positions were randomly chosen by the program, having the limitation of no overlaps between particles. The properties of these particles were equal to those used on the previous simulations. A gravity field of  $9.8\text{m/s}^2$  was used during the simulations. The generated particles were allowed to fall and accommodate inside the box, thus the initial height of the samples was less than 13cm.

The simulation started subjecting the sample to an isotropic compression up to a confining pressure equal to  $18 \times 10^5$  Pa. Three copies of this original sample were saved at different values of confining pressure ( $\sigma_3 = 1 \times 10^5$  Pa,  $5 \times 10^5$  Pa, and  $10 \times 10^5$  Pa). Then, deviator stresses were applied to the three copies while the correspondent  $\sigma_3$  in each case was kept constant. The deviator stresses were induced by moving downwards the upper wall of the box with a constant velocity of  $1 \times 10^{-7}$  m/step. Granular crushing developed as a result of the isotropic compression and the application of the deviator stresses.

#### 5.4.2 Isotropic compression

Fig.5.18 shows the void ratio of the upper and lower regions of the sample at different values of applied confining pressure. Also, some snap shots of the sample at different confining pressures are presented in this figure. These snap shots show that crushing started at a confining pressure between  $5 \times 10^5$  Pa and  $6 \times 10^5$  Pa. It can be seen how a sudden change in the trend of the void ratio curves also took place at these stresses, and the sample exhibited a well defined normal compression line after this. At low values of isotropic confining pressure, the upper and lower parts of the sample had different values of void ratio, but after crushing this difference was considerably reduced. The snap shots presented in Fig.5.18 show that most of the crushing took place at the boundaries of the sample. This was expected since these particles were transmitting large forces and their coordination numbers were small due to the

imposed geometrical constraints. It was found that no more than a third generation of crushing was produced during the isotropic compression.

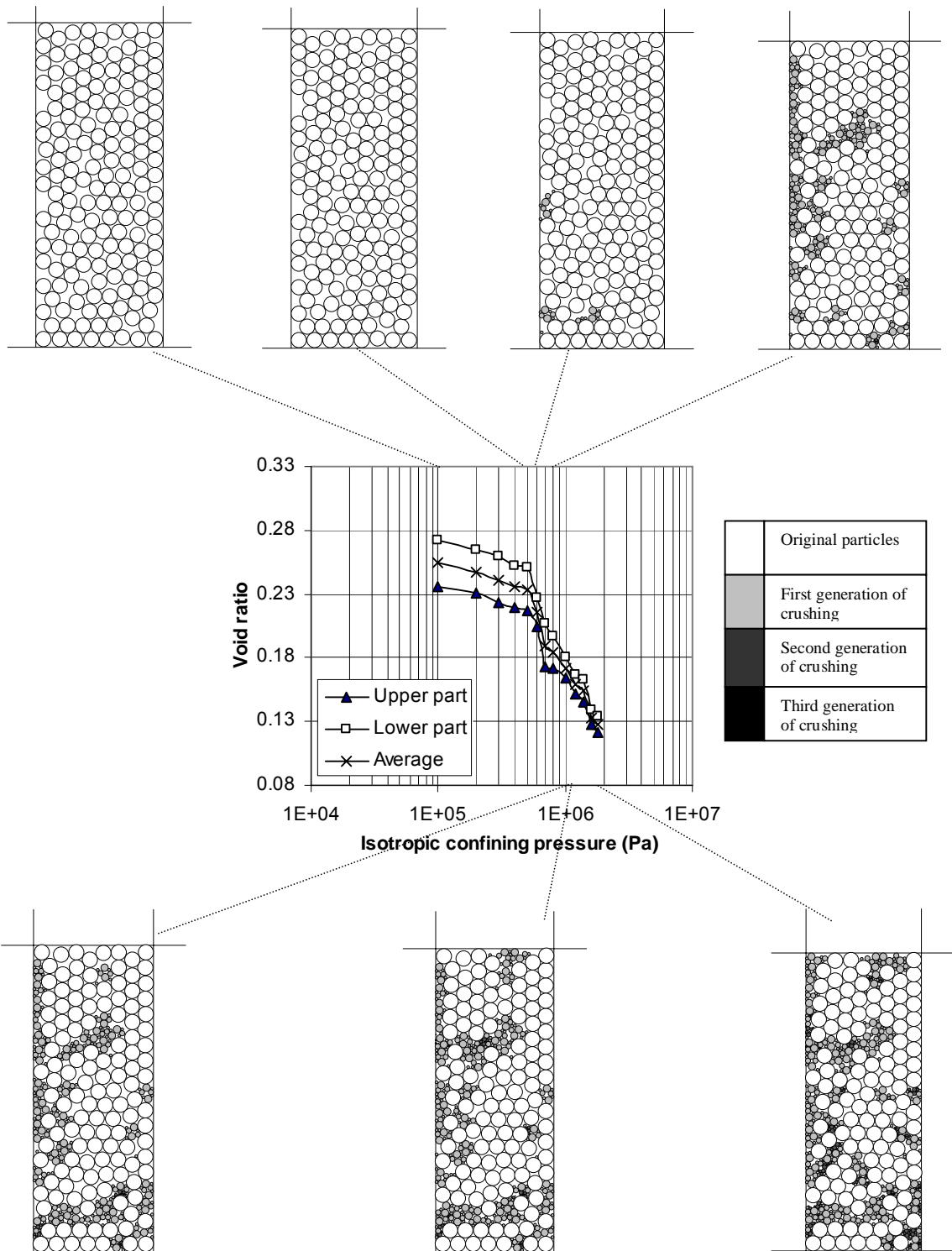


Figure 5.18 Isotropic compression of the original sample

#### 5.4.3 Shearing at $\sigma_3=1 \times 10^5$ Pa

A copy of the original sample subjected to the isotropic compression was recorded at a confining pressure of  $1 \times 10^5$  Pa. It can be noted from Fig.5.18 that the sample at this stage was far from experiencing crushing. After this, a deviator stress was induced on the sample while  $\sigma_3$  remained constant. The values of the applied deviator stress and the induced vertical and volumetric strains were recorded. The test was ended at a vertical strain of 0.3. It was observed that the volume of the sample did not significantly change during the test. Thus, the value of volumetric strain was -0.0116 at the end of the simulation (negative sign represents a decrement in volume). No crushing was produced during this simulation. The detailed results of this test (except the Mohr circle at failure) are not presented since they are not relevant for the analysis.

#### 5.4.4 Shearing at $\sigma_3=5 \times 10^5$ Pa

A copy of the original sample subjected to the isotropic compression was recorded at a confining pressure of  $5 \times 10^5$  Pa. This confining pressure was very close to the yield stress that caused the beginning of crushing. A deviator stress was induced while  $\sigma_3$  remained constant. Fig. 5.19 shows the obtained values of deviator stress and the correspondent vertical strains. Also, some snap shots of the sample at different values of vertical strain are presented with their correspondent values of volumetric strain. The deviator stress vs. vertical strain curve presents spike drops as a consequence of particle crushing and particle rearrangement. It is interesting that when crushing started, the sample momentarily experienced a small negative value of deviator stress since  $\sigma_1$  was smaller than  $\sigma_3$ .

Fig. 5.19 shows that crushing started at a small value of vertical strain, and continued until the end of the test. Even though some of the initial crushing took place at the boundaries of the sample, it did not concentrate in these regions. Moreover, by comparing Fig.5.18 and Fig.5.19 it can be observed that

the regions where most of the crushing took place were not exactly the same. No particles representing more than a third generation of crushing were generated during this simulation.

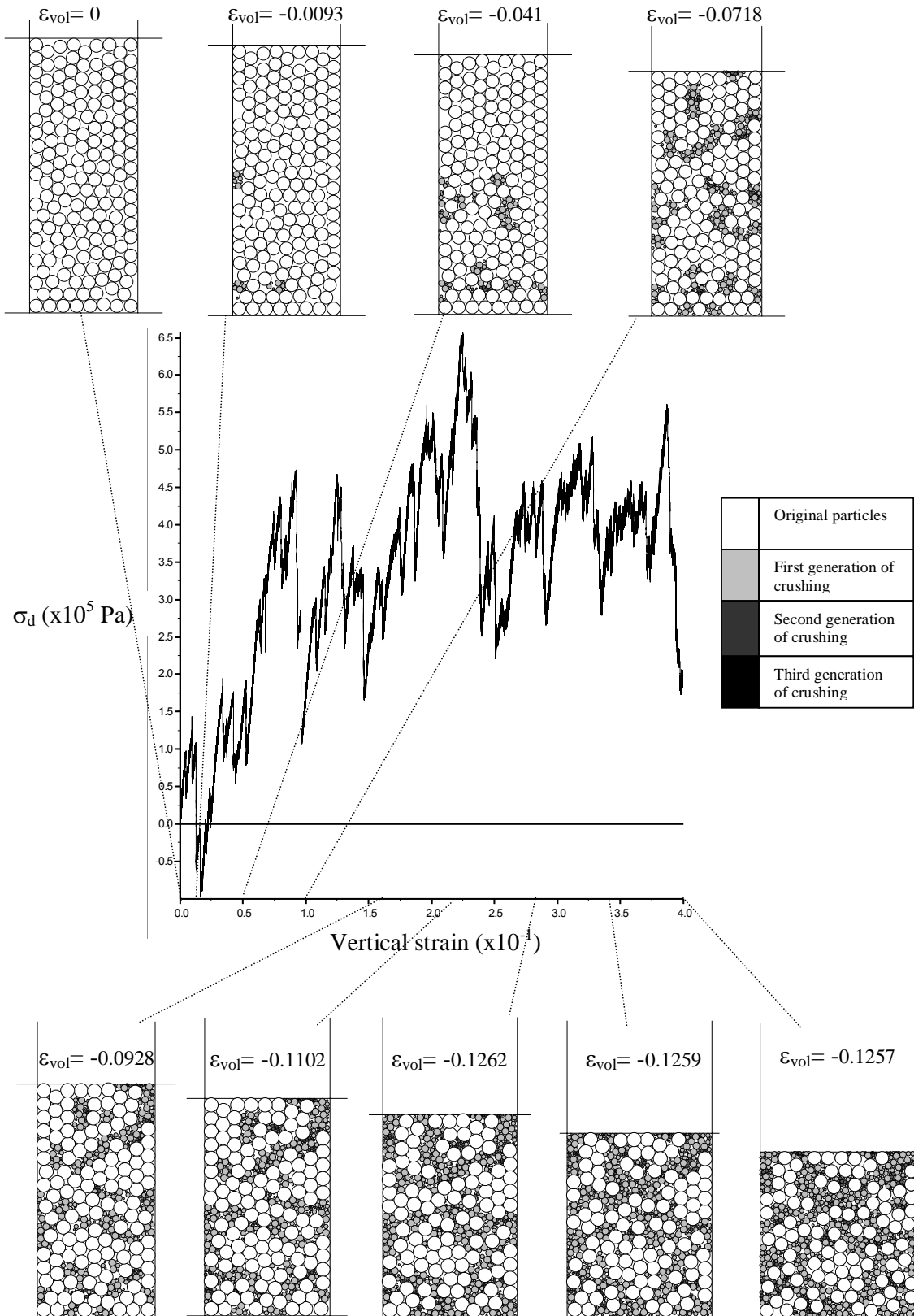


Figure 5.19 Evolution of granular crushing during the application of the deviator stress at  $\sigma_3 = 5 \times 10^5$  Pa

The values of volumetric strain in Fig.5.19 show that the sample presented a contractive behavior due to the generated crushing. Fig.5.20 shows some details of the sample close to the peak deviator stress and at the end of the test. It can be seen in these snap shots that the fragments generated as the product of particle crushing reorganized in an efficient way, so it is logical that the volume of the sample was significantly reduced as a consequence of crushing. On the other hand, the last three snap shots on Fig.5.19 show that after a vertical strain of 0.28, the sample experienced a very small amount of dilation as a consequence of the densification of the simulated material.

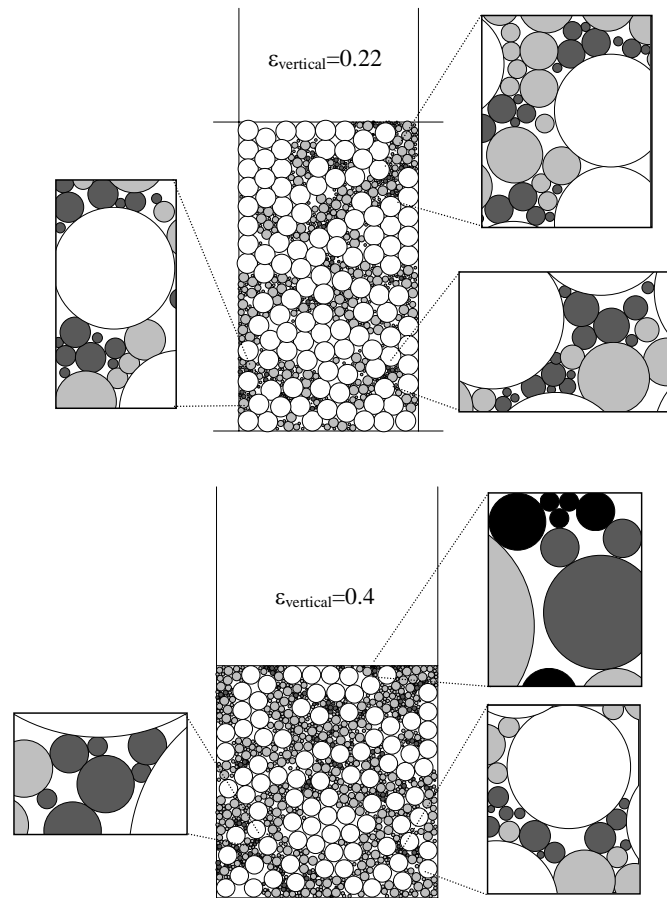


Figure 5.20 Details of the sample subjected to shearing at  $\sigma_3=5 \times 10^5$  Pa

The snap shots presented in Fig.5.19 and Fig.5.20 show how the simulated group of particles tended to evolve from a uniform granular material into a well graded mixture of sizes. Fig.5.21 shows the particle size distribution of the sample as a function of the induced vertical strain. It also includes the power regression line for the distribution obtained at the end of the simulation. The higher value obtained for the square of the correlation coefficient,  $R^2$ , in the power regression shows that the distribution obtained as a result of crushing is fractal in nature, as suggested by other authors (Chapter 2). However, it can be noted that the fragmentation fractal dimension obtained from this power regression is equal to 1. Even though the sample was evolving into a well distributed mixture of sizes, it was still being dominated by the original particles. Fig.5.21 also shows that granular crushing took place between a vertical strain of 0.28 and 0.4. As it was pointed out before from the volumetric strain results, the sample experienced a small amount of dilation during these values of vertical strain. Thus, the dilation due to the produced densification of the sample suppressed the contractive behavior due to the particle crushing.

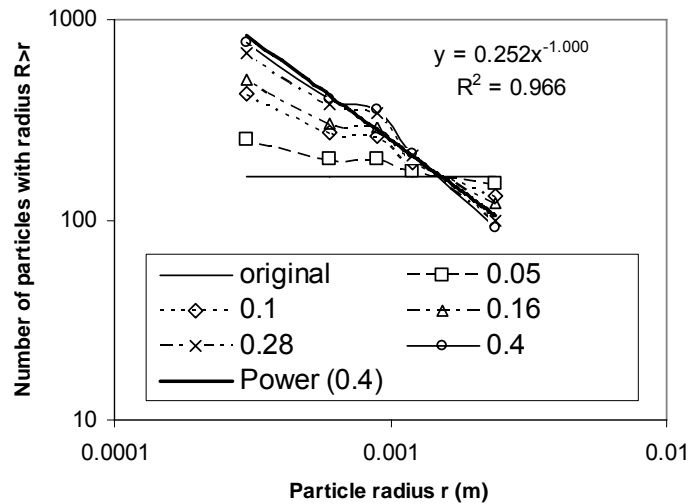


Figure 5.21 Evolution of the grain size distribution of the sample subjected to shearing at  $\sigma_3=5 \times 10^5$  Pa

#### 5.4.5 Shearing at $\sigma_3=10 \times 10^5$ Pa

A copy of the original sample subjected to the initial isotropic compression was recorded at a confining pressure of  $10 \times 10^5$  Pa. As shown on Fig.5.18, the sample presented some crushing as a result of this isotropic compression. A deviator stress was induced on the sample while  $\sigma_3$  remained constant. The values of the applied deviator stress and the induced vertical and volumetrical strains are presented in Fig.5.22. Snap shots of the sample at different values of vertical strain are also presented in this figure. Additionally, some details of the sample at vertical strains of 0.20 and 0.42 are provided in Fig.5.23.

It can be observed that a significant amount of particle breakage was produced due to the induced deviator stress. Particles representing a fourth generation of crushing were produced due to the severe crushing. Opposite to the sample sheared at  $\sigma_3=5 \times 10^5$  Pa, this sample exhibited a contractive behavior during all the simulation. This was expected since the confining pressure was significantly higher than the one previously used.

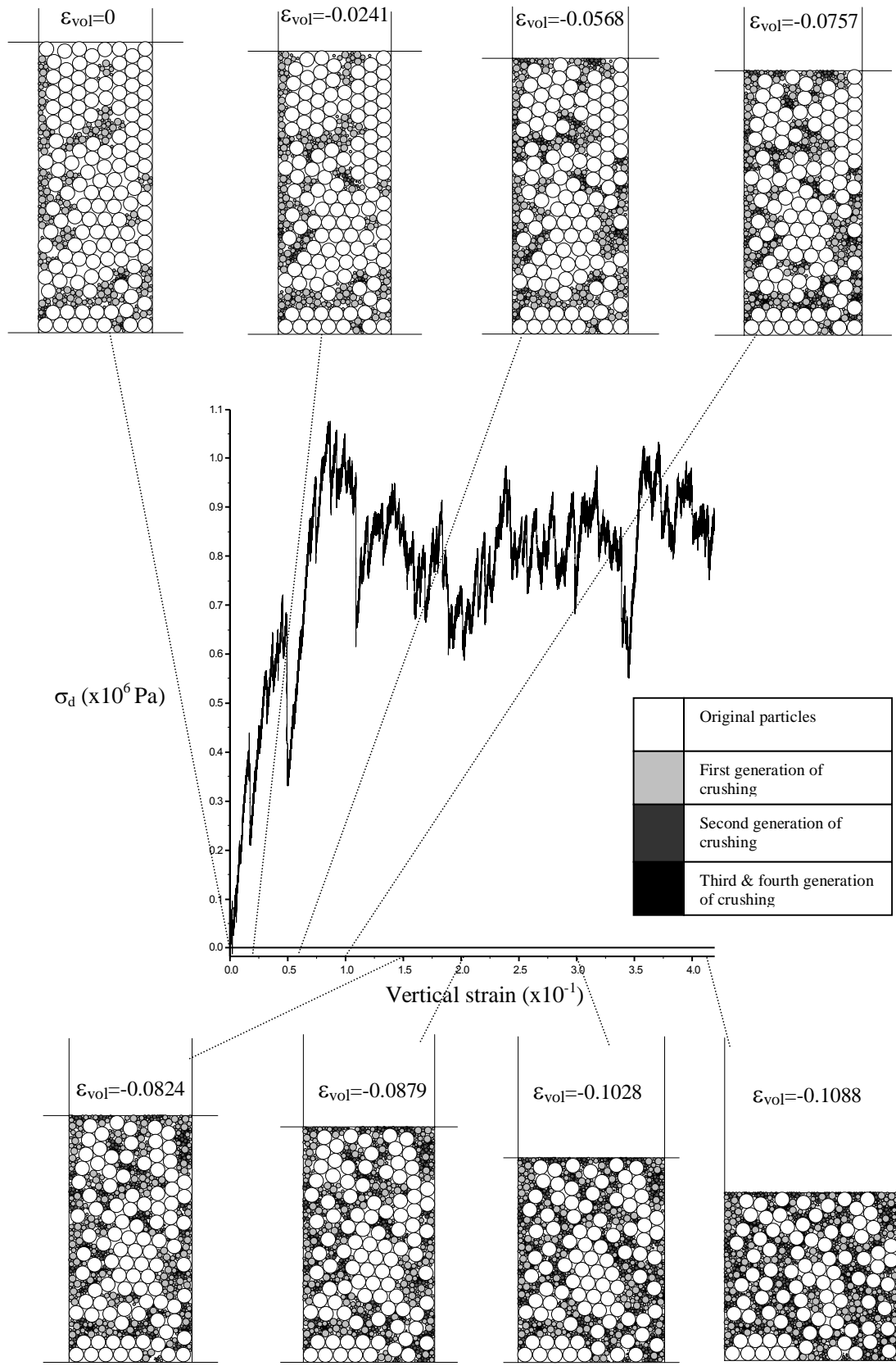


Figure 5.22 Evolution of granular crushing during the application of the deviator stress at  $\sigma_3 = 10 \times 10^5$  Pa

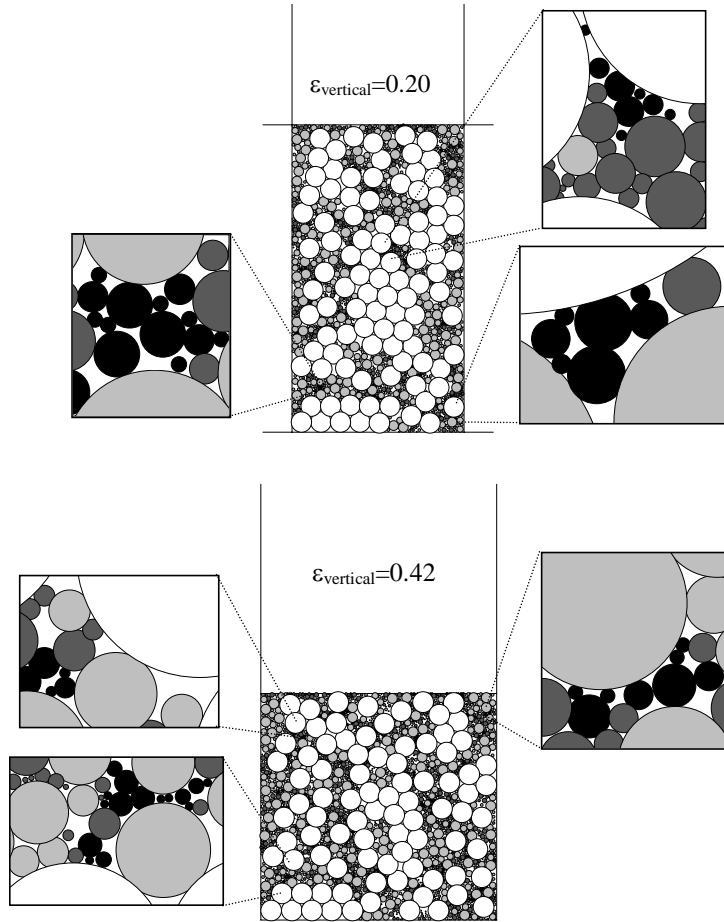


Figure 5.23 Details of the sample subjected to shearing at  $\sigma_3=10 \times 10^5$  Pa

The grain size distribution of the sample as a function of the induced vertical strain is presented in Fig.5.24. A power regression line was fitted to the grain size distribution of the sample at the end of the test. The higher value obtained for the square of the correlation,  $R^2$ , shows that the obtained distribution was fractal in nature. The obtained fragmentation fractal dimension at the end of the test was equal to 1.169. This value is higher than the one obtained after shearing the sample subjected to  $\sigma_3=5 \times 10^5$  Pa. This shows that more crushing was produced during the test with  $\sigma_3=10 \times 10^5$  Pa than during the test with  $\sigma_3=5 \times 10^5$  Pa. Nevertheless, as it can be observed in Fig.5.22 and Fig.5.23 the sample was still being

dominated by the original large particles. Thus, it was expected that the obtained fragmentation fractal dimension was smaller than the maximum value of 1.5 reported in the literature.

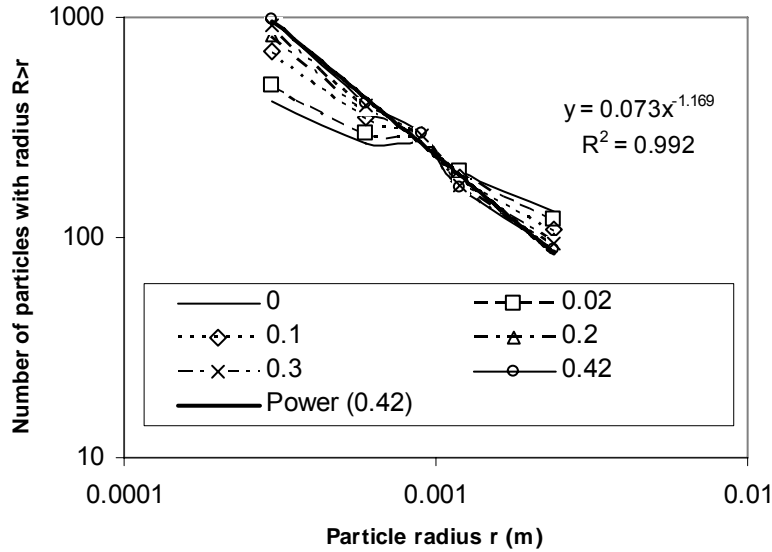


Figure 5.24 Evolution of the grain size distribution of the sample subjected to shearing at  $\sigma_3=10 \times 10^5$  Pa

#### 5.4.6 Change on the internal friction angle

The Mohr circles were plotted taking the peak values of deviator stress at each confining pressure. After this, a Mohr-Coulomb failure envelope was calculated independently for each circle. Fig.5.25 shows the obtained three circles, failure envelopes, and values for the internal friction angle  $\phi$ . The internal friction angle considerably reduced due to the generated particle crushing (from  $27^\circ$  to  $20.5^\circ$ ). Joining the failure points on the circles will result in a non-linear failure envelope. A possible explanation to this phenomenon lays on the advantage that the unbreakable particles have with respect to the transmission of forces inside the sample. If one of the particles transmitting the forces in the shearing zone is suddenly broken, the shear resistance of the sample will momentarily decrease as a result of the rearrangement of the particles. The neighbors of this broken particle may also fail since they will have to momentarily bear the forces that the broken particle used to bear. The decrement in shearing resistance as

a result of particle crushing seems to be a dominant factor over the increment in shear resistance that should take place as a result of the sample changing from a uniform to a somewhat well graded material.

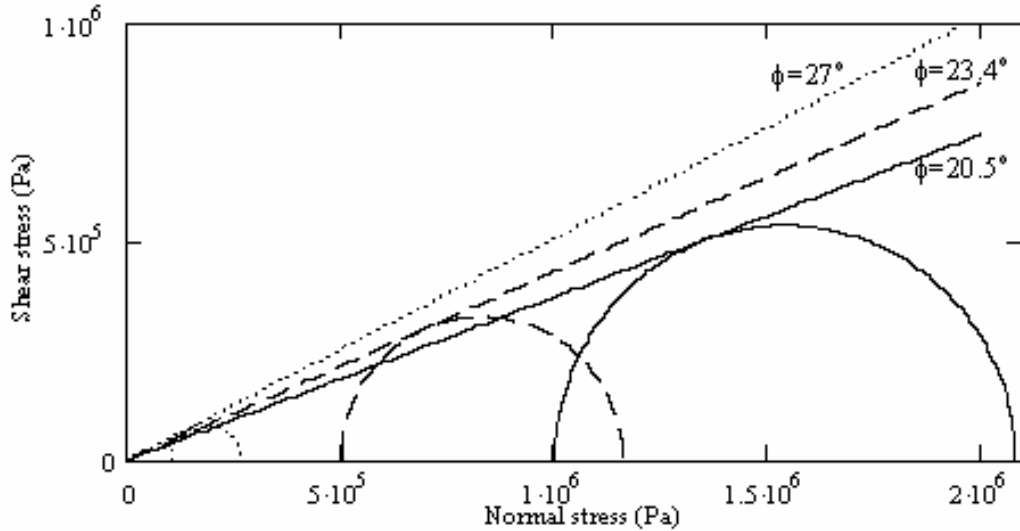


Figure 5.25 Mohr circles and failure envelopes for each test

### 5.5 CONCLUSIONS FROM THE SIMULATED LABORATORY TESTS

The results from the simulation of the confined uniaxial compression test indicate that crushing does not develop uniformly throughout the sample, but rather concentrates in certain regions. These observations agree with experimental results of uniaxial tests conducted on sand. Other results from the simulation such as the relationship between the applied vertical stress and the void ratio of the sample satisfactorily agree with experimental results previously reported in Chapter 3 and those reported by other researchers.

The results from the simulation of the direct shear test at a higher value of vertical force showed that most of the crushing took place at the middle of the shearing zone. This behavior is explained by the

fact that these particles had to transmit large loads due to the induced shear stress, and their coordination numbers were affected by the induced displacement. The induced displacement affected the coordination number of the particles in this zone since the moving particles experienced a momentary loss of contacts. It was found that the overall porosity of this sample did not significantly change even though the sample was undergoing particle breakage. The compressive behavior due to particle breakage was counteracted by the dilating behavior due to particle rearrangement. The evolution of the particle size distribution shows that the sample tended toward a fractal distribution. However, at the end of the simulation the grain size distribution of the sample was still being dominated by the original particles. The sample could experience more crushing if the compressive force is increased beyond the values used in this study. Finally, it was found that the peak friction coefficient of the simulated material was reduced as a consequence of granular crushing. All this is in agreement with the experimental results reported in Chapter 3 and those reported by other researchers.

The results from the simulated ring shear tests showed that the residual friction coefficient of the simulated material maintained a constant value regardless of the severe degradation of the particles. Moreover, it was found that the particle size distribution of the original uniform material evolved toward a fractal distribution of sizes. These results were consistent with those from the laboratory tests and provided also a visualization of the crushing evolution.

The results of the isotropic compression test showed that the simulated material resembled well the behavior of a real crushable material, presenting a yield stress and a well defined normal compression line. The tests with shearing stages at constant values of confining pressure showed that crushing evolved differently in the isotropic compression test and these tests. Not only more crushing was produced during the tests with deviator stresses, but also the regions where particle breakage concentrated were different. It was found that the samples at the end of both biaxial tests at  $\sigma_3=5 \times 10^5$  Pa and  $\sigma_3=10 \times 10^5$  Pa had a fractal grain size distribution dominated by the large original particles. More particle crushing was found at the end of the test at  $\sigma_3=10 \times 10^5$  Pa than at the end of the test at  $\sigma_3=5 \times 10^5$ . Finally, it was found that the

peak value of the internal friction angle of the simulated material was reduced as a consequence of granular crushing. These results were consistent with experimental results reported by other researchers, and satisfactorily agree with the results from the other simulated tests.

Because the results of the simulations satisfactorily agree with experimental results, it can be concluded that the proposed failure criterion is appropriate.

## **6.0 PRACTICAL APPLICATIONS**

The laboratory tests presented in Chapter 3 were used to understand how crushing influences the behavior of crushable granular materials. Moreover, the DEM simulations presented in Chapter 5 allowed a visualization of the evolution of crushing. Since the results of Chapter 5 were consistent with those previously obtained in the laboratory tests, the proposed particle breakage criterion introduced in Chapter 4 was validated. This chapter explores some practical applications where this model can be used to understand how crushing affects the behavior of engineering structures such as driven piles, footings, railtracks, and pavement structures.

### **6.1 DEM ANALYSIS OF CRUSHING AROUND DRIVEN PILES IN GRANULAR MATERIALS**

It is widely accepted that the capacity of driven piles in breakable weak sands such as calcareous sands is only a fraction of the capacity of driven piles in strong sands such as quartz sands [Gilchrist, 1985], [Murff, 1987]. This difference could be attributed initially to the reduction of the mobilized angle of shearing resistance that is associated with particle crushing in weak sands. Another explanation for the low bearing capacity of piles in weak sand is based on the stress relaxation that takes place on the sand located in the periphery of the pile [Bolton and Cheng, 2002], [Randolph, 2003], [White and Bolton, 2004]. This relaxation is the result of the migration of fines produced by crushing as well as by grain rearrangement.

The objective of this application is to give a better understanding and produce a visualization of the penetration resistance in driven piles. Two DEM simulations of a pile being driven into a previously

compacted uniform soil are presented. The two simulations used the same initial sample, but crushing was allowed during only one of the simulations. Even though the presented simulations have some constraints, such as considering only dry two dimensional uniform discs, the obtained results agree with experimental results obtained by other researchers and field observation reported in the literature.

### 6.1.1 Previous work

Modeling the effects of pile driving in granular soils is not a simple task. It is also complicated to do it with only standard laboratory tests. Previous researchers have used centrifuge tests and calibration chamber tests on carbonate sands in order to get a better understanding of what really occurs when driving a pile into weak sands [McDowell and Bolton, 2000], [Klotz and Coop, 2001], [Bolton and Cheng, 2002], [White and Bolton, 2004]. McDowell and Bolton [2000] showed that when driving a pile into calcareous sand, at certain shallow depth the point penetration resistance reaches a peak which is associated with the occurrence of particle breakage. Bolton and Cheng [2002] and White and Bolton [2004] showed that considerable stresses are induced ahead of the pile tip, generating crushing of the material in this zone and moving it to the sides. After the tip of the pile passed through the zone where crushing took place, the fragments coated the shaft of the simulated pile. Also, the granular material forming part of the pile-soil interface shear zone was observed to contract with continued pile penetration as a result of crushing and fines migration. This caused a decrease in shaft friction.

### 6.1.2 Configuration of the sample

The first step was the construction of a virtual container with a width of 40cm and a height of 80cm. The shear and normal stiffness of the walls forming the box were set to  $1 \times 10^9$  N/m. The walls were assumed to have a friction coefficient of 0.7. The granular material was simulated by 6500 discs having the same properties used for all the simulations presented in Chapter 5. The 6500 particles were generated

inside the virtual container and allowed to settle down due to the gravity forces. Their positions were randomly chosen by the program with the constraint of no overlaps between discs. Thus, the resulting sample had a loose structure.

After the generation of the sample, the top horizontal wall of the box was moved downwards until it made contact with the particles and induced compaction. This wall continued to move downwards until the forces generated inside the sample were approaching the values required to induce particle crushing. After this, the top wall was moved upwards until it separated from the particles. The friction coefficient of the particles and walls were temporarily set to zero and the top horizontal wall was again moved downwards inducing a second compaction until the generated forces approached the values required to induce particle crushing. The top wall was finally moved upwards unloading the sample, and deleted after it separated from the top of the sample. The friction coefficients of the particles and walls were set to their initial value (0.7).

A simulated pile was also created. It had a constant width of 3cm, and it was closed at the tip with two inclined planes forming an angle of  $45^\circ$  with the vertical. During the simulations the pile was driven with a vertical velocity of  $1 \times 10^{-6}$  m/step. The friction coefficient between the pile and the discs was set to a value equal to 0.7. The coefficients of normal and shear stiffness of the pile were equal to  $1 \times 10^9$  N/m. The ratio of pile width to the particle diameter was equal to 5. This may have had an effect on the results, as it is considerably smaller than the values between 10 and 20 suggested by other researchers for the accurate prediction of the load that a pile can resist [Lee, 1990], [Gui, 1995]. However, even with this shortcoming, the simulations helped in the visualization and understanding of what happens to a granular material when a simulated pile (or cone penetration test) is driven into it.

### 6.1.3 Results using an unbreakable granular material

Fig.6.1 shows the penetration resistance for the point and the shaft of the pile as a function of the vertical displacement. Also, some snap shots of the simulation are presented at different values of vertical

deformation. The simulated dense granular material developed tip and shaft resistance, although the shaft resistance was small compared to the tip resistance. Spike drops were generated in the tip and shaft resistance curves due to particle rearrangement as the pile was penetrating the simulated granular material. An average maximum point resistance equal to  $3.5 \times 10^4 \text{N}$  developed between penetrations of 35cm and 45 cm (45cm corresponds with 15 times the pile diameter). A temporarily maximum tip resistance equal to  $6.6 \times 10^4 \text{N}$  was also developed, but it was not considered to be a representative value as it was only a spike on the curve. A maximum average shaft resistance equal to  $0.75 \times 10^4 \text{N}$  also occurred between penetrations of 35cm and 45cm.

Fig.6.1 also shows the contact forces generated inside the granular material. The thickness of each line is proportional to the magnitude of the contact force. The maximum value of contact force at each moment is specified in each snap shot, and corresponds with the thicker line. Note how these contact forces concentrated at the tip of the pile.

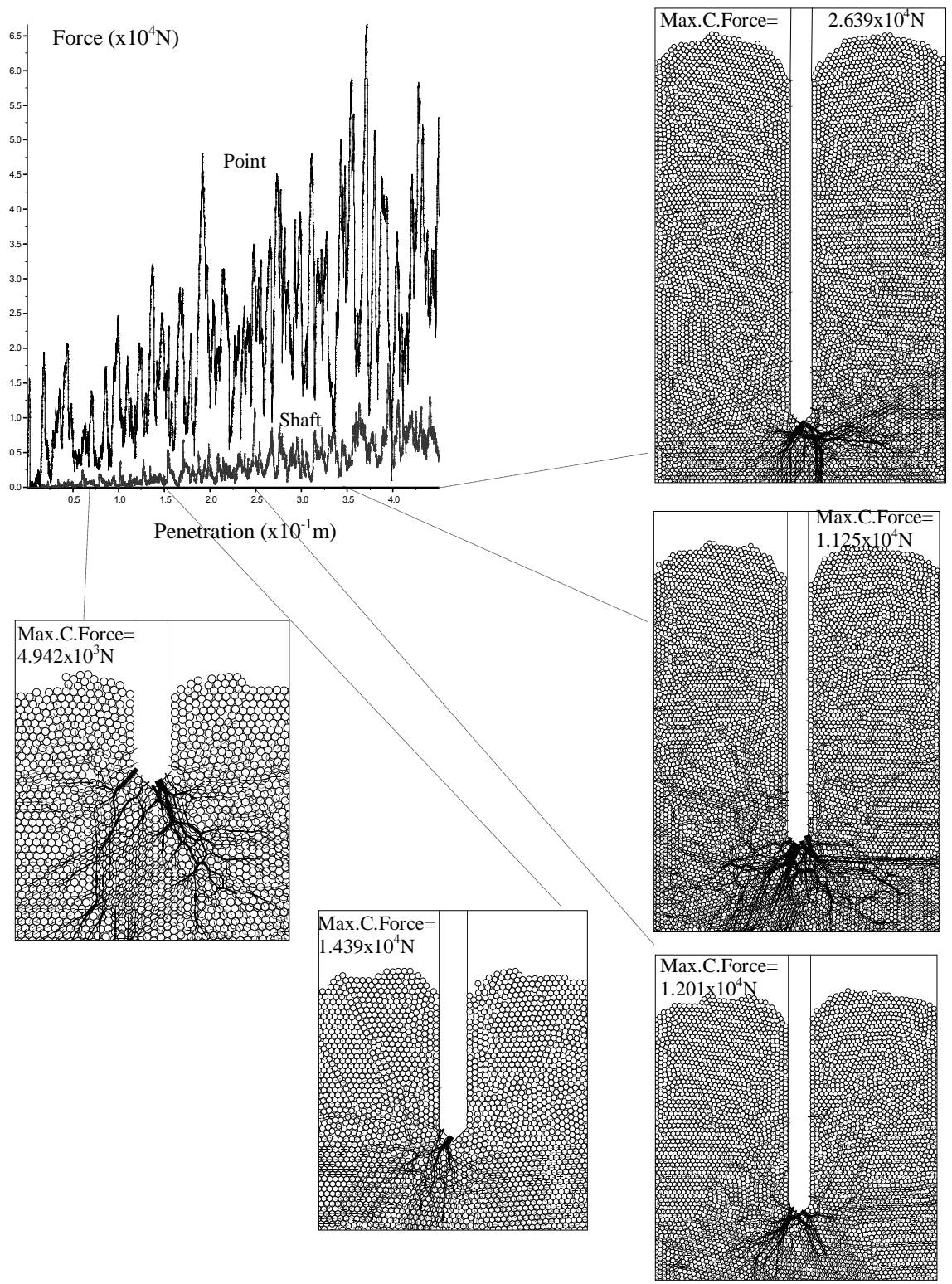


Figure 6.1 Penetration resistance, unbreakable granular material

#### 6.1.4 Results using a crushable granular material

Fig.6.2 shows the penetration resistance of the pile and some snap shots of the sample at different values of vertical displacement. Amplified details of the sample at a value of penetration equal to 45cm are shown in Fig.6.3. Fig.6.2 shows that crushing started and concentrated in the region below the tip of the pile. Four generations of crushing were identified during the simulation. As the pile passed through the zone below the tip where particle crushing took place, the generated fragment migrated to the sides and coated the shaft of the pile (Fig 6.3). Thus, crushing was never generated at the shaft even though the last snapshot shows several fragments surrounding the pile shaft (Figs.6.2 and 6.3). These results are in agreement with the experimental results discussed by Bolton and Cheng [2002] and White and Bolton [2004].

The simulated crushable granular material developed tip and shaft resistance, although the shaft resistance was again small compared to the tip resistance. Spike drops were generated in the tip resistance curve due to particle crushing and particle rearrangement as the pile was penetrating the simulated granular material (Fig.6.2). An average maximum value of tip resistance was equal to  $2.9 \times 10^4 \text{N}$ , and some spikes showed maximum values around  $4.4 \times 10^4 \text{N}$ . These values are considerably smaller than those obtained during the first simulation. The reduction in point resistance is associated with the generated particle crushing and particle rearrangement. An average maximum value of shaft resistance equal to  $0.6 \times 10^4 \text{N}$  was recorded during the final part of the simulated test. This value is lower than the one recorded during the first simulation. Thus, crushing also affected the shaft resistance of the pile.

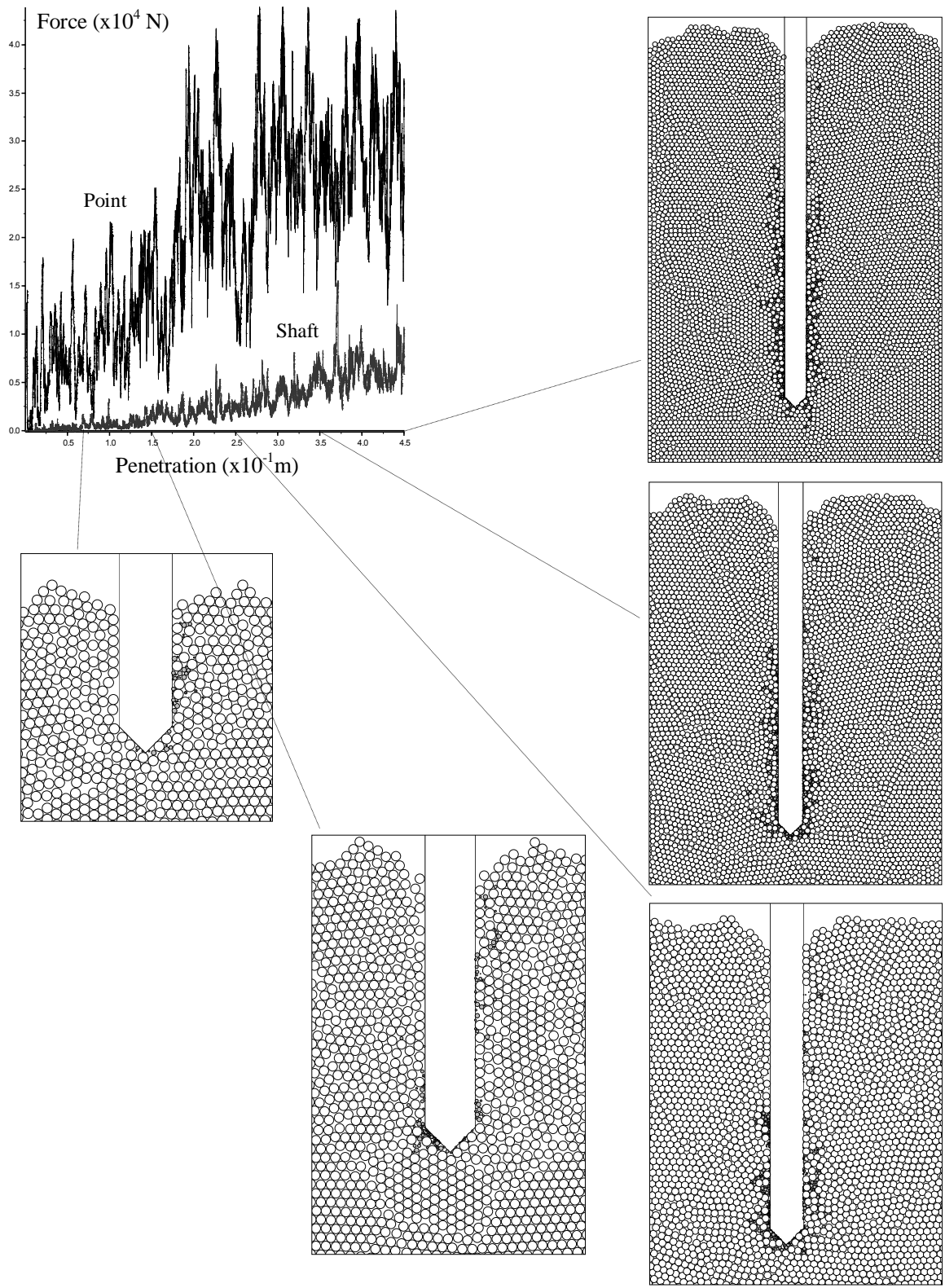


Figure 6.2 Penetration resistance, crushable granular material



composed of uncrushable particles. Breakage and particle rearrangement were observed to induce stress relaxation, and caused the broken granular material to develop a lower resistance to pile penetration.

It was found that the original DEM can be enhanced by including a simplified tensile failure criterion. Several phenomena related with the process of pile installation in granular materials can now be visualized and analyzed using this tool. This is something that is difficult to do with standard laboratory equipment or by the use of the finite element method.

## **6.2 EFFECT OF CRUSHING ON THE BEARING CAPACITY OF FOOTINGS**

Granular materials underneath footings are subjected to static and dynamic loads. As a result of these loads particle crushing may occur depending on the strength of the soil particles. Granular materials composed by hard quartz particles crush less than weak granular materials composed by calcareous sediments or volcanic sands. As mentioned before, particle crushing reduces the internal friction angle of the material as it is seen from the curvature of the Mohr-Coulomb failure envelope. Moreover, particle crushing produces settlements. Thus, the performance of an engineering structure supported on a crushable soil can be compromised due to granular crushing. This section presents the results of two simulations intended to study the effect of crushing on the bearing capacity of a simulated dense granular material. Even though the two simulations consider the same idealized material, crushing was allowed only in one simulation.

### **6.2.1 Previous work**

During the past few years a growing number of experimental and in-situ observations, and some plasticity models have been used trying to understand how crushing affects the bearing capacity of footings supported on crushable granular materials such as carbonate or volcanic sands [Kusakabe et al.,

1992], [Hagiwara et al., 1997], [Miyake and Kusakabe, 1997], [Byrne and Houlsby, 2001], [Cassidy et al., 2002], [Cassidy et al., 2005]. In particular, Kusakabe and his colleagues have shown that granular crushing takes place directly underneath the footing and in the active zone of the produced failure surface. Crushing and volume contraction takes place at the failure surface only in the area located in the active zone since this zone is subjected to a considerable value of confining and shear stresses. On the other hand, the material located in the passive zone of the failure surface only experiences dilatancy since the confining stress in this region is very low.

### 6.2.2 Configuration of the simulated material and testing procedure

The first step was the generation of the simulated sample. A simulated box container having a width of 1.5m and a height of 0.5m was created. The coefficients of normal and shear stiffness of the walls forming this box were set to  $1 \times 10^9$  N/m, and their friction coefficients were set to 0.7. After this, 15000 particles (having the same properties used for the laboratory tests presented in the previous chapter) were randomly generated inside the box with the constraint of no overlaps between them. These particles were allowed to settle under a gravity field ( $9.8 \text{ m/s}^2$ ). After this, compaction was induced by vertically moving the upper horizontal wall with a velocity of  $1 \times 10^{-6}$  m/step. The friction coefficient of the particles was temporarily set to zero during this compaction in order to facilitate the rearrangement of the simulated granular material. This compaction continued until the maximum contact force in the material was approaching the value required to produce particle breakage. After this, the upper horizontal wall was moved upwards with a velocity of  $1 \times 10^{-6}$  m/step unloading the sample. This wall was deleted when it separated from the upper part of the simulated granular material. After compaction the thickness of the artificial granular layer was equal to 32.5cm. The bulk unit weight of the material at this time was  $21.31 \text{ kN/m}^3$ . This was a very high density considering that the sample was in a dry state.

The simulated footing had a base width of 20cm and a base length of 1m. It was artificially embedded 5cm inside the soil by deleting 323 particles. The friction coefficient and the coefficients of

normal and shear stiffness of this footing were equal to those used for the walls forming the box container. After the creation of the footing, the friction coefficient of the particles was reset to its original value of 0.7. Two different copies were recorded since it was the starting point for both simulations. In both cases the loading test started by moving the footing with a vertical velocity equal to  $5 \times 10^{-7}$  m/step. Fig.6.4 shows the initial state of the samples. This is the only figure in this application that shows the complete sample, since the following figures have been cut to the area of interest to allow a better visualization of the details.

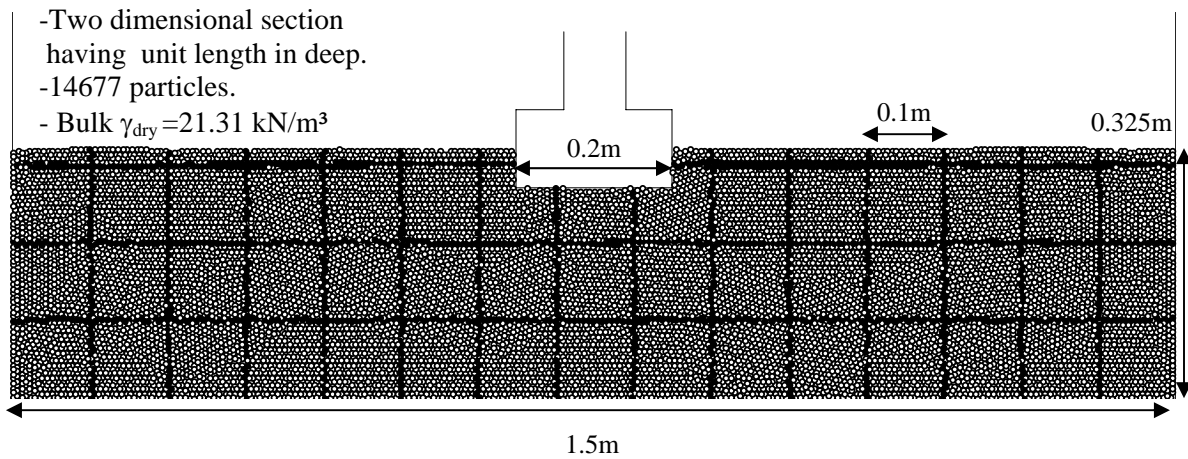


Figure 6.4. Initial configuration of the samples

During the first simulation particle crushing was not allowed. In order to visualize the deformation of the granular material during this simulation a square grid of 10cm size was made by coloring certain particles. On the other hand, during the second simulation particle crushing was allowed. The square grid was not used since the color of the particles changed depending on the generation of crushing that they represented. Thus, the original particles were white, the particles produced as a result of crushing of the original particles were light grey (first generation of crushing), the fragments coming from these fragments were dark grey (second generation of crushing), and finally the fragments produced from the breaking of these second generation fragments were colored black (third generation of crushing).

No more than a third generation of crushing was found inside the sample at the end of the simulation even though the adopted failure criterion did not have a breaking size limit.

### 6.2.3 Results of the simulation without crushing

Fig.6.5 shows the vertical displacement vs. applied vertical force curve of the first simulation. As mentioned before crushing was not allowed during this simulation. The maximum applied vertical force was equal to  $1.7 \times 10^5$  N and took place at a vertical displacement of 0.8cm (4% of the base width). This was considered to be the bearing capacity of the footing since this point clearly represented the failure of the material. The behavior exhibited in Fig.6.5 is consistent with the fact that the material was in a very dense state at the beginning of the test.

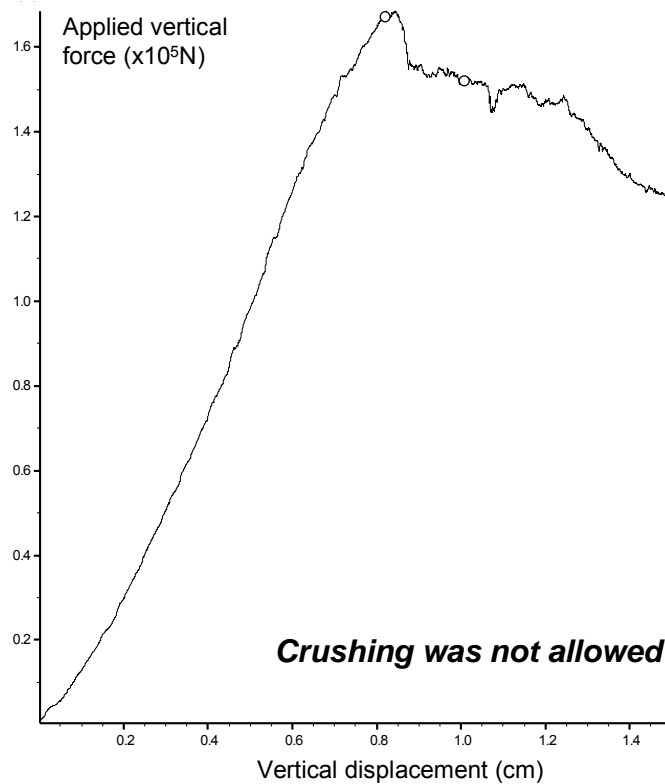


Figure 6.5. Vertical displacement of the footing vs. applied vertical force; no crushing allowed.

Fig.6.6 shows the state of the sample at the point of failure ( $dv=8\text{mm}$ ): Fig.6.6.a shows the deformation of the sample, Fig.6.6.b shows the velocity vectors of the particles, and Fig.6.6.c shows the contact forces developed inside the granular material. Fig.6.6.a and Fig.6.6.b allow a visualization of the symmetric failure surfaces developed inside the material. These symmetric failure surfaces correspond with what is expected to occur in a dense granular material. It must be noted that even though the velocity vectors clearly show the localization of the failure surface, the snap shot of the particles (Fig.6.6.a) does not show severe discontinuities inside the material. This means that the movement was just starting. The velocity vectors shown in Fig.6.6.b show that besides the movement that occurred at the failure surface, other regions of the sample below the failure surfaces started also to mobilize. However, the velocity vectors at these regions are very small compared to those obtained at the failure surfaces. Fig.6.6.c shows the formation of vertical force chains. The load transmitted from the footing to the granular material

concentrated in vertical columns. Thus, concentration of stresses occurred in the region in contact with the footing.

Fig.6.7 shows the state of the sample at a vertical displacement of 1.5cm: Fig.6.7.a shows the deformation of the sample, Fig.6.7.b shows the velocity vectors, and Fig.6.7.c shows the contact forces. At this point significant shearing at the failure surfaces had occurred. Fig.6.7.a shows that some regions of the sample were severely disturbed as is seen in the shape of the original squares formed by the colored particles. Moreover, some discontinuities in these lines can be appreciated. Some circles have been drawn in Fig.6.7.a to highlight some of these discontinuities. Fig.6.7.b shows that the upper and lower failure surfaces were mobilized and the sample was failing at various points. Fig.6.7.a and Fig.6.7.b also allow a visualization of the dilatancy that took place at the failure surfaces. As is seen in Fig.6.7.a some voids were located at the failure surfaces (surfaces identified from Fig.6.7.b). These voids were the result of the particle rearrangement produced after shearing the original dense material.

In general the behavior exhibited in the previous figures accurately represents the failure mechanism expected to occur in dense sands. The next section shows the results obtained during a similar test allowing particle breakage.

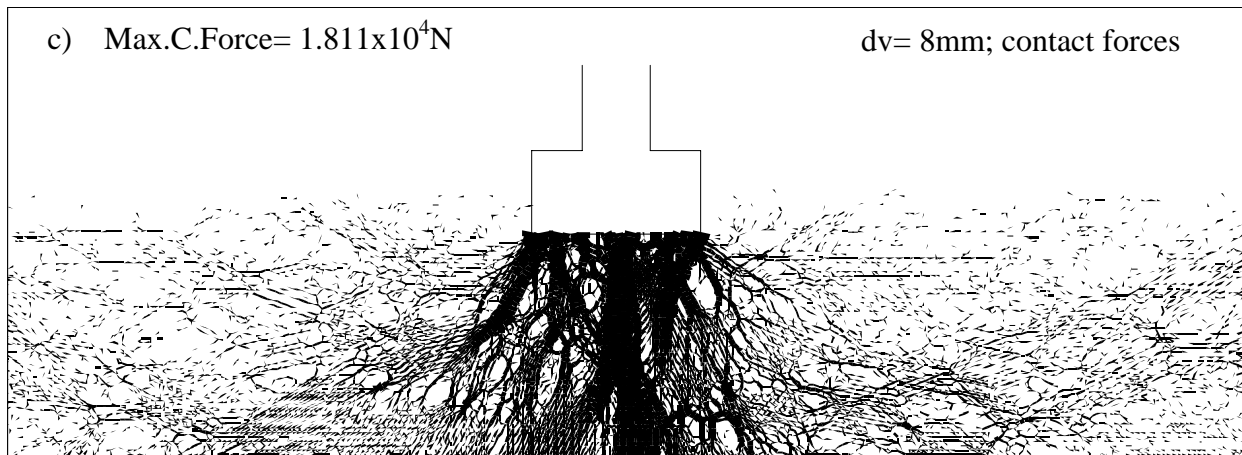
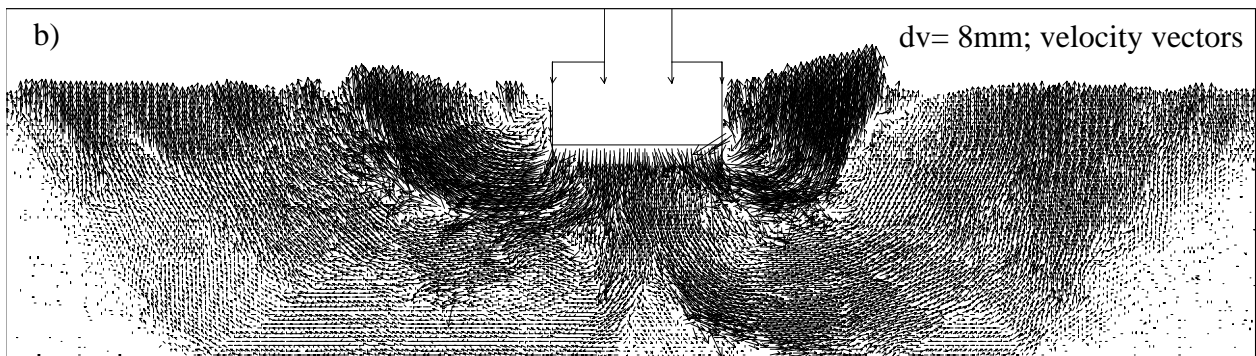
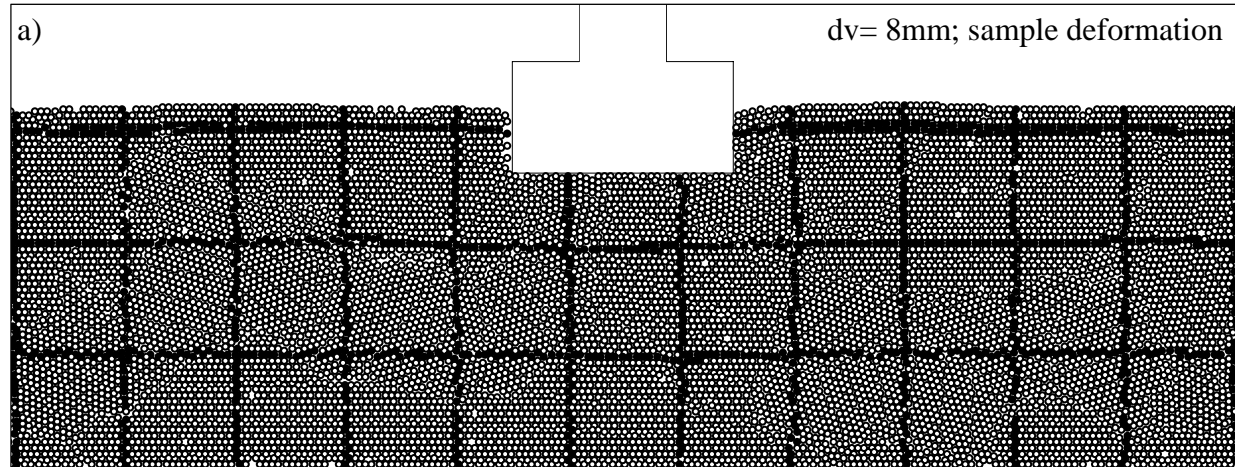


Figure 6.6 Uncrushable sample at the moment of failure, dv=0.8cm.

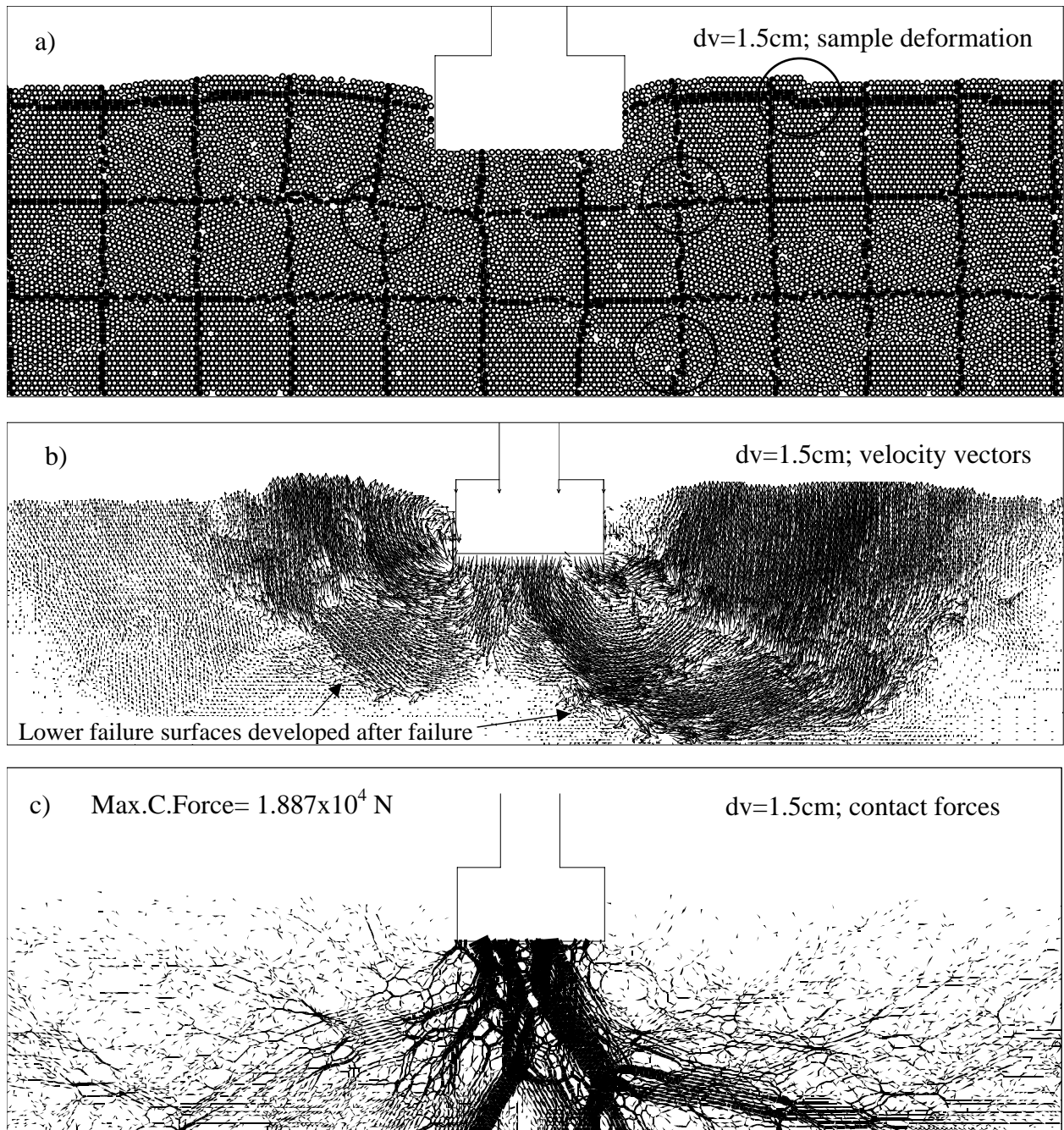


Figure 6.7 Uncrushable sample at  $dv=1.5\text{cm}$ .

#### 6.2.4 Results of the simulation considering crushing

Fig.6.8 shows the vertical displacement vs. applied load curve and some snap shots of the regions that exhibited crushing during the simulation. The exhibited trend on the curve is different from the one observed in the previous case. The maximum value of applied force was equal to  $1.35 \times 10^5$  N and took place at two different values of vertical displacement: 0.65cm and 1.25cm. This bearing capacity was 21% less than the bearing capacity recorded for the uncrushable case. Nevertheless, it can be appreciated from the snap shots that only a moderate amount of crushing took place.

The first snap shot shows that crushing started before the first peak. The first broken particles were located at the contact with the footing and near the corners. At the first peak, most of the crushing was found directly underneath the footing. Thus, the first failure of the material was due to punching rather than plastic deformation at the shearing surfaces. However, some crushing occurred at the locations of the failure surfaces identified in the first simulation, including the shallow primary failure surfaces and the deep secondary failure surfaces. As the sample continued to be loaded, more crushing developed directly underneath the footing but specially at the primary and secondary failure surfaces. The last snap shot shows how the produced fragments allow a visualization of the path of these failure surfaces. Thus, the second failure of the material can be attributed to the crushing produced at these surfaces and the punching generated due to the particle crushing near the base of the footing. As a result of crushing, contraction of the material took place at the failure surfaces. This is consistent with the observations reported by Kusakabe and his colleagues.

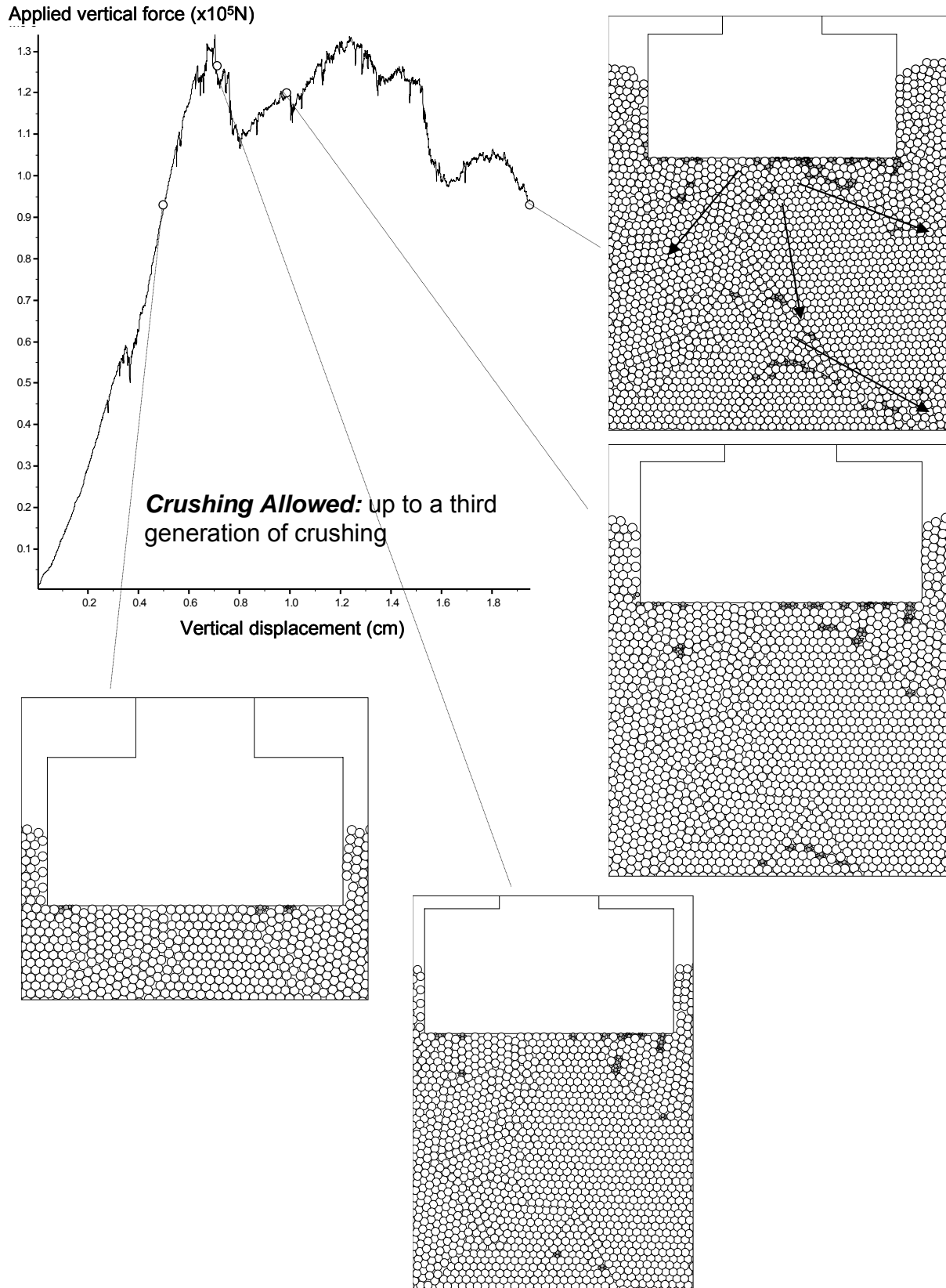


Figure 6.8 Vertical displacement of the footing vs. applied vertical force; crushing allowed.

Fig. 6.9 shows the velocity vectors of the soil particles at different moments of the simulation. Fig.6.9.a shows that at the beginning of the simulation the particles started to move following the primary failure surfaces identified during the first simulation. Up to this point the sample exhibited a behavior very similar to the one observed previously. Fig.6.9.b shows that at the moment of the first peak, the maximum velocities took place at the interface between the footing and the soil. Particle crushing was taking place at this time, and the produced fragments were traveling at high speeds. This caused a relaxation of the soil in this region and ultimately the first failure due to punching. Fig.6.9.c and Fig.6.9.d show that as the simulation continued the particles located at the shearing zones (identified during the first simulation) moved following the path of the failure surfaces. The breakage of some of the particles located in these regions can be observed in the velocity vectors of some particles traveling at high speeds and deviating from the traveling path of their neighbors. The results observed on Fig.6.9 validate the hypothesis of a first failure due to punching and a second failure due to crushing underneath the footing and a combination of mobilization and crushing at the shearing surfaces.

Fig.6.10 shows the contact forces between particles at different moments of the simulation. As observed during the first simulation, the load imposed by the footing was transmitted mainly through vertical force chains.

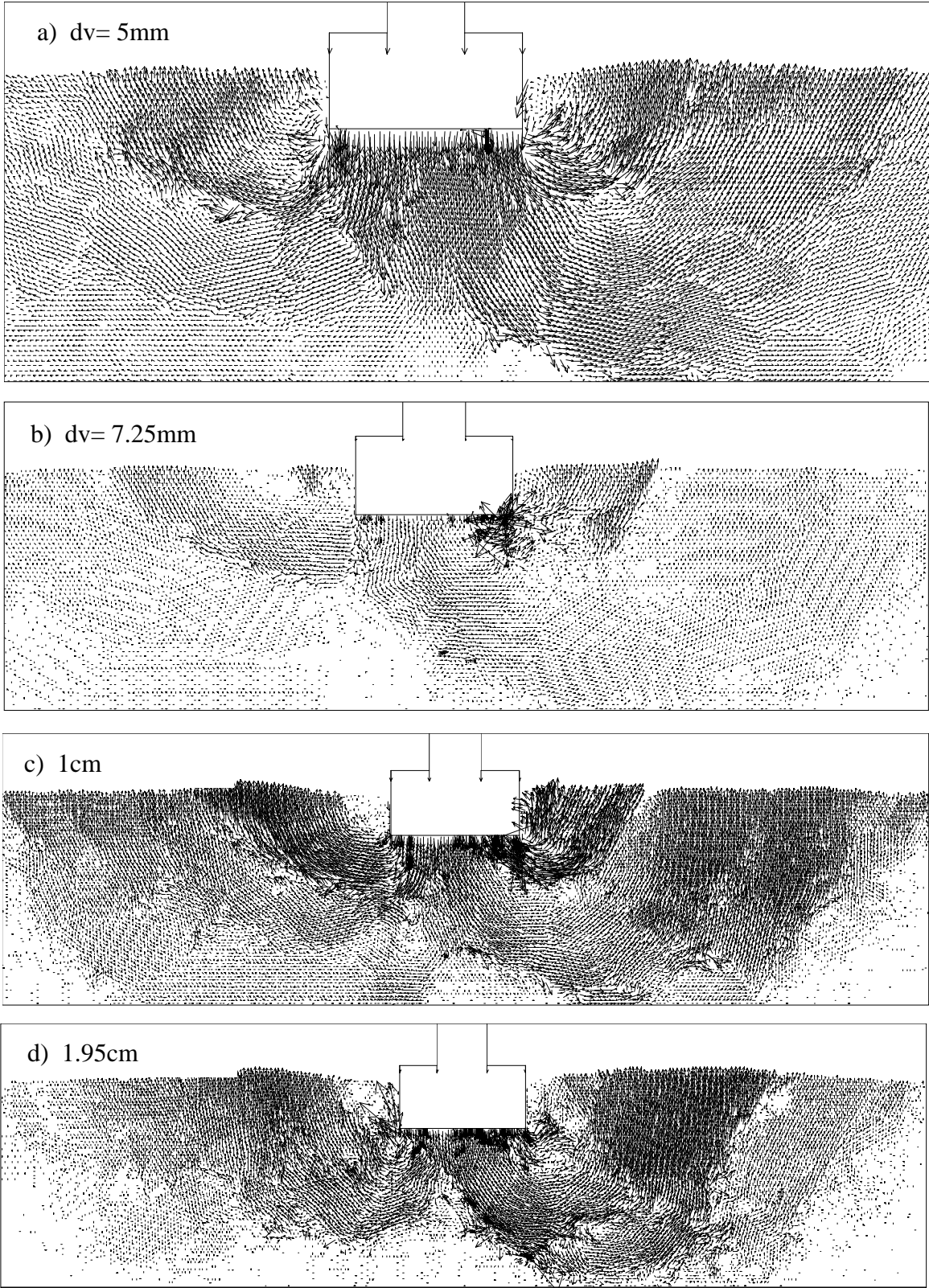


Figure 6.9 Velocity vectors of the particles at different moments of the simulation; crushing allowed.

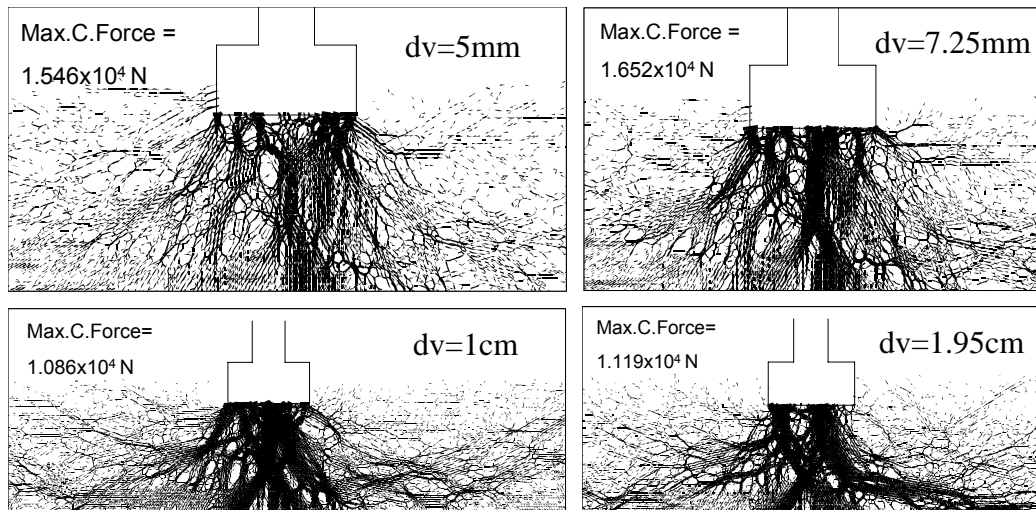


Figure 6.10. Contact forces between particles; crushing allowed

### 6.2.5 Discussion of the results and comparison with the theoretical bearing capacity equation

The results obtained during the DEM simulations showed that the bearing capacity of a dense crushable soil is strongly reduced due to particle crushing. Moreover, the failure mechanism changed from the general shear failure to a combination of this failure mechanism and punching failure. It was found that the dilatancy that is commonly observed when shearing a dense granular material was suppressed by the contracting behavior due to the rearrangement of the original particles and the fragments produced by crushing.

The results observed during the simulation without crushing correspond with the typical behavior of dense sands. Thus, the author was interested in finding out if the obtained results agree with those predicted by the theoretical general equation for bearing capacity. A back calculation was performed using Eq.(6.1) [Das, 1999] to calculate the internal friction angle of the simulated material. Eq.(6.1) does not consider the terms associated with soil cohesion and embedment (the embedment was only 5cm):

$$q_u = (0.5)(\gamma)(B)(N_\gamma)(F_{\gamma s})(F_{\gamma d}) \quad (6.1)$$

$q_u$  is the ultimate bearing capacity calculated as the maximum applied load divided by the area of the footing:  $1.7 \times 10^5 \text{ N} / (0.2\text{m})(1\text{m}) = 850 \text{ kN/m}^2$ ;  $\gamma$  is the unit weight of the soil =  $21.31 \text{ kN/m}^3$ ;  $B$  is the width of the footing =  $0.20\text{m}$ ;  $N_\gamma$  is the non dimensional bearing capacity factor that is only a function of the internal friction angle;  $F_{\gamma_s}$  is a correction factor due to the shape of the footing:  $1 - 0.4(B/L) = 0.92$ ; and  $F_{\gamma_d}$  is a correction factor due to embedment of the footing that is equal to 1 since the ratio between the embedment and the width of the footing was less than 1. Eq.(6.1) was solved for  $N_\gamma$  since all the other terms were known; thus, a value equal to 433.8 was obtained. This value of  $N_\gamma$  corresponds with an internal friction angle close to  $47^\circ$ .

As presented by Bolton [1986], the peak internal friction angle of a granular material can be separated into two independent components: the interparticle friction angle (estimated with the critical state frictional angle) and the component associated with the dilatancy of the material. In the simulated case the term associated with the dilatant component can be calculated since the total internal friction angle ( $47^\circ$ ) and the interparticle friction angle ( $35^\circ$ , the friction between particles was set to 0.7) are known. Thus, a component equal to  $12^\circ$  is associated with the dilatancy that took place during the simulation. These three numbers are in the range of typical values measured in the laboratory for dense sands [Bolton, 1986]. It can be concluded that the bearing capacity measured during the first simulation is in agreement with the general equation for bearing capacity that is widely used in geotechnical applications.

The reduction on the bearing capacity of the simulated crushable granular material was a combined effect of the different failure mechanisms and a reduction on the dilatant component of the internal friction angle (the interparticle friction angle is not affected by crushing). However, is difficult to estimate to what extent each of these factors was responsible for the drop in bearing capacity.

### 6.2.6 Significance of the application

The obtained results showed that the bearing capacity of a dense crushable soil strongly reduces due to particle crushing. The failure mechanism changed from the general shear failure in the case considering unbreakable particles, to a combination of this failure mechanism and punching failure when considering particle crushing. It was found that the dilatancy that is commonly observed when shearing a dense granular material was suppressed by the contracting behavior due to particle crushing. The obtained results from the simulation considering unbreakable particles agree well with the behavior predicted by the theoretical bearing capacity equation. The obtained results from the simulation considering crushable particles agree well with insitu observations previously reported by other researchers.

## **6.3 ANALYSIS OF RAILTRACK BALLAST DEGRADATION DURING CYCLIC LOADING**

Ballast materials forming part of railway structures are subjected to cyclic loads. As a result of these loads, ballast densification, aggregate degradation, and lateral spread of the ballast material underneath the ties takes place inducing permanent deformations on the railways [Raymond and Bathurst, 1987]. As reported by Indraratna et al. [1998], maintenance and rehabilitation costs of railtracks due to problems related with ballast performance are substantial, and millions of dollars are annually spent around the world in these activities. Understanding the crushable behavior of railtrack ballast could lead to the design of better railways that will reduce these costs.

This section presents the results of two DEM simulations intended to study the effect of crushing on the behavior of a simulated ballast material forming part of a simulated track section. Even though the two simulations consider the same idealized material, crushing was allowed only in one simulation. The simulated track sections were subjected to a cyclic load, and the values of permanent deformation as a

function of the number of cycles were recorded. Moreover, snap shots of the track sections are presented allowing a visualization of the evolution of crushing.

### 6.3.1 Selection of railtrack ballast

Rail track ballast should be crushed rock, nickel slag or crushed gravel composed by strong and durable particles with sizes typically between 0.25in (6.4mm) and 2.5in (64mm). In order to select a specific track ballast, economic factors such as production, transportation, placement, and maintenance costs need to be considered [Klassen et al., 1987]. Moreover, the material properties need to be evaluated and compared with standards. Typical specifications for track ballast include ranges of acceptable values of bulk specific gravity, gradation, percentage of fractured particles, resistance to weathering (Magnesium soundness, absorption), and resistance to degradation (Los Angeles abrasion, mill abrasion) [CP Rail specifications for ballast, 1987].

During the past few years, special attention has been placed on the resistance to degradation tests. The LA abrasion test and the mill abrasion test have been the standard in North America while the Deval abrasion test has been the British standard [Selig and Boucher, 1990]. All these tests consist on placing a specific amount of material inside a drum, and subjecting the drum to a specific number of rotations. After the test, the material is sieved and its degradation is measured as the percentage of mass that became finer than certain size (smaller than the initial one). Due to the nature of the tests, the LA abrasion test (steel balls are added to the drum) gives a measure of resistance to particle fragmentation while the mill abrasion test and the Deval test give a measure of resistance to abrasion.

As pointed out by McDowell et al. [2003], none of the traditional resistance to degradation tests physically represents the conditions that the material will experience at the track. On the other hand, the Aggregate Crushing Value (ACV) test, which is commonly used in the U.K., gives a better representation of the track conditions since the sample is subjected to a confined one-dimensional compression. The ACV is calculated as the percentage by mass passing the 2.36mm sieve after the test. However, this test

has the disadvantage that needs to be performed on particles with sizes between 10mm and 14mm, which are considerably smaller than real ballast particles [McDowell et al., 2003]. As pointed out by previous researchers, there is a relationship between ballast particle size and particle strength. By measuring the strength of individual ballast particles subjected to a diametrical compression test, McDowell et al. [2003] and Lim et al. [2004] showed that particle strength reduces when increasing particle size. Moreover, Selig and Boucher [1990] showed that the amount of abrasion increases in the mill and Deval tests when increasing the size of the ballast particles. Thus, there is a need to developed better standard tests that represent track conditions more closely.

Computer simulations of railtrack ballast being subjected to track conditions can help to understand the causes and consequences of ballast degradation. Even though computer simulations are idealizations of real conditions, they can be used to study where particle degradation starts, how evolves, and how affects the permanent deformation of railtracks. Understanding this could help to produce better standard tests and better ballast specifications.

### 6.3.2 Application of DEM to simulate ballast degradation during cyclic loading

Laboratory tests and computer simulations are two different approaches that can be used to study the effects of ballast degradation during simulated track conditions. Large-scale laboratory testing is an important tool that has been used in the past to study ballast degradation during simulated track conditions [Raymond and Bathurst, 1987], [Boucher and Selig, 1987]. However, it does not provide a simple way to visualize the evolution of this phenomenon. On the other hand, computer simulations in the form of DEM provide this visualization and allow to compare the different results obtained by modifying the properties of the simulated material.

A pioneer work presented by Lim and McDowell [2005] showed that it is possible to simulate cyclic loading in a simulated three-dimensional DEM box test, where railtrack ballast is loaded by a simulated single sleeper (cross tie). However, due to the high computational time required to simulate

ballast degradation, they did not allow particle crushing to occur. This study tries to expand the application validated by Lim and McDowell [2005] by using a two-dimensional model that allows ballast degradation. The fact that this is a 2D model and particles are replaced by fragments when satisfying a failure criterion considerably reduces the computational time, allowing to simulate 200 load cycles in a track segment covering 3 sleepers.

### 6.3.3 Configuration of the simulated material and testing procedure

The first step was the generation of the simulated sample. A simulated box container with a width of 2.1m, and a height of 0.6m was created. The coefficients of normal and shear stiffness of the walls forming this box were set to  $1 \times 10^9$  N/m, and their friction coefficients were set to 0.7. After this, 681 particles having a radius of 2cm were randomly generated inside the box with the constraint of no overlaps between them. The density of these particles was set to  $2500 \text{ kg/m}^3$ , and their coefficients of normal and shear stiffness were set to  $1 \times 10^8$  N/m. Their friction coefficient was also set to 0.7. These particles were allowed to settle under a gravity field ( $9.81 \text{ m/s}^2$ ). After this, compaction was induced by vertically moving the upper horizontal wall with a velocity of  $1 \times 10^{-7}$  m/step. This compaction continued until the maximum contact force in the material was approaching the value required to produce particle breakage. After this, the upper horizontal wall was moved upwards with a velocity of  $1 \times 10^{-7}$  m/step unloading the sample. This wall was deleted when it separated from the upper part of the simulated ballast material.

The simulated 3 sleepers had a width of 30cm, a height of 15cm, and a length of 1m. The separation between the sleepers was equal to 30cm. Also, the distance between the sleepers and the vertical boundaries of the container was equal to 30cm. The sleepers were placed over a 45cm ballast bed. They were artificially embedded inside the ballast by deleting some particles. The final sample was composed by 639 ballast particles. The friction coefficient and the coefficients of normal and shear stiffness of the sleepers were equal to those used for the walls forming the box container. The 3 sleepers

were idealized as only one body since they were not allowed to have differential settlements. The seating of the sleepers was carried out by moving them at a vertical velocity of  $1 \times 10^{-7}$  m/step until the maximum contact force developed in the ballast was half the value required to produce particle breakage. After this, the sleepers were unloaded and the reference point for measuring permanent deformation was fixed. Two different copies were recorded since this was the starting point for both simulations.

A FISH function was programmed by the author to induce the cyclic loading. The programmed servo-mechanism vertically moved the 3 sleepers at a velocity equal to  $5 \times 10^{-7}$  m/step until the total applied force was equal to 62kN, then, the 3 sleepers were unloaded at the same velocity until no load was applied to them. This cyclic loading and unloading continued until 200 cycles were completed.

#### 6.3.4 Results of the simulation without crushing

Fig.6.11 shows the relationship for the 200 cycles of applied load and the induced vertical deformation of the uncrushable ballast bed. It can be noted that during the first load cycles the material presented elastic and permanent deformations, but as the number of cycles increased the non-recoverable component decreased. Thus, the right part of Fig.6.11 shows that during the last cycles the ballast material presented an almost perfect elastic behavior. The induced permanent deformation was the result of particle rearrangement, which was enhanced by the cyclic nature of the applied load.

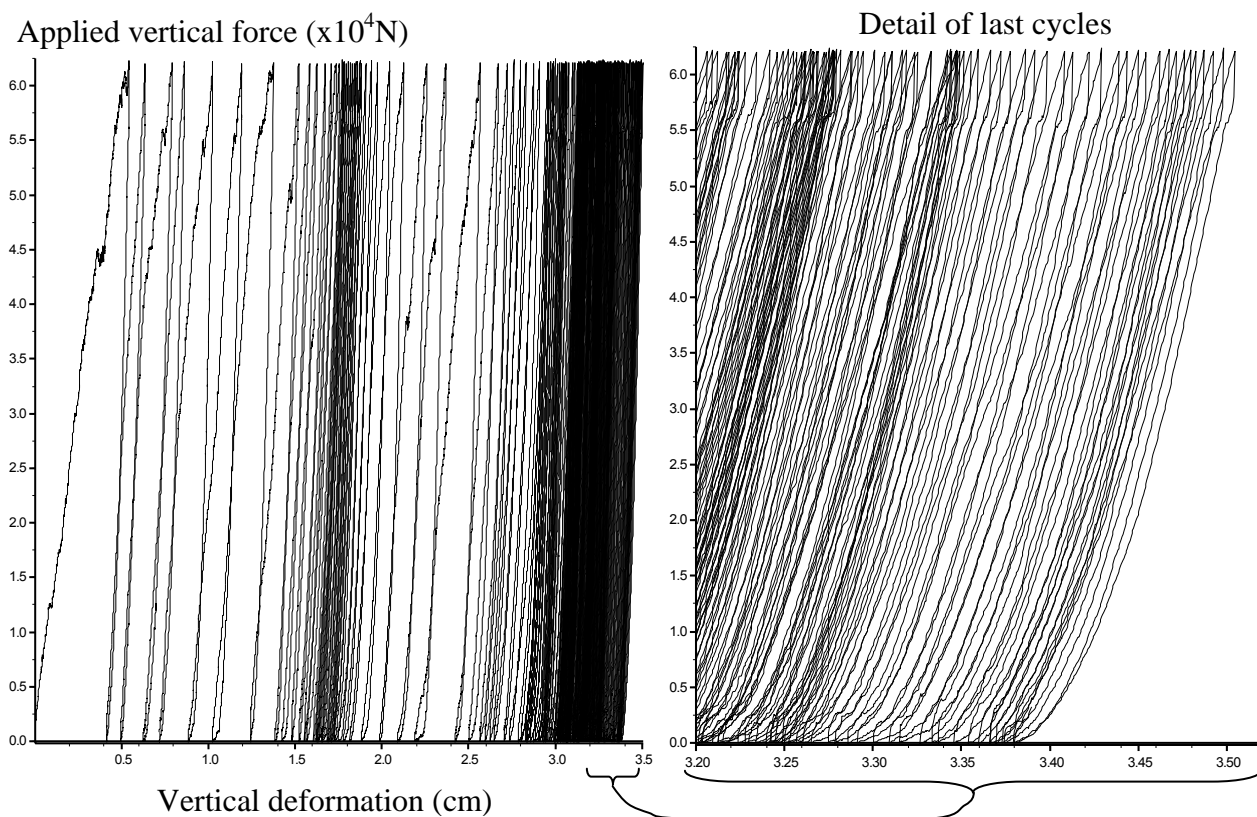


Figure 6.11. Load cycles, uncrushable ballast

Fig.6.12 shows the induced permanent deformation as a function of the number of applied cycles. The permanent deformation of the ballast bed tended to stabilize after the completion of almost 60 cycles, and it was equal to 3.38cm at the end of the 200 cycles. Fig.6.12 also shows some snapshots of the simulated track section at different number of cycles. The rail and connections to the sleepers shown in these snapshots were added to the figures after the simulations, they are shown only to help the reader to understand the configuration of the track section. The “invisible” real rigid connection between the three sleepers was programmed in the numerical model and does not appear in these figures.

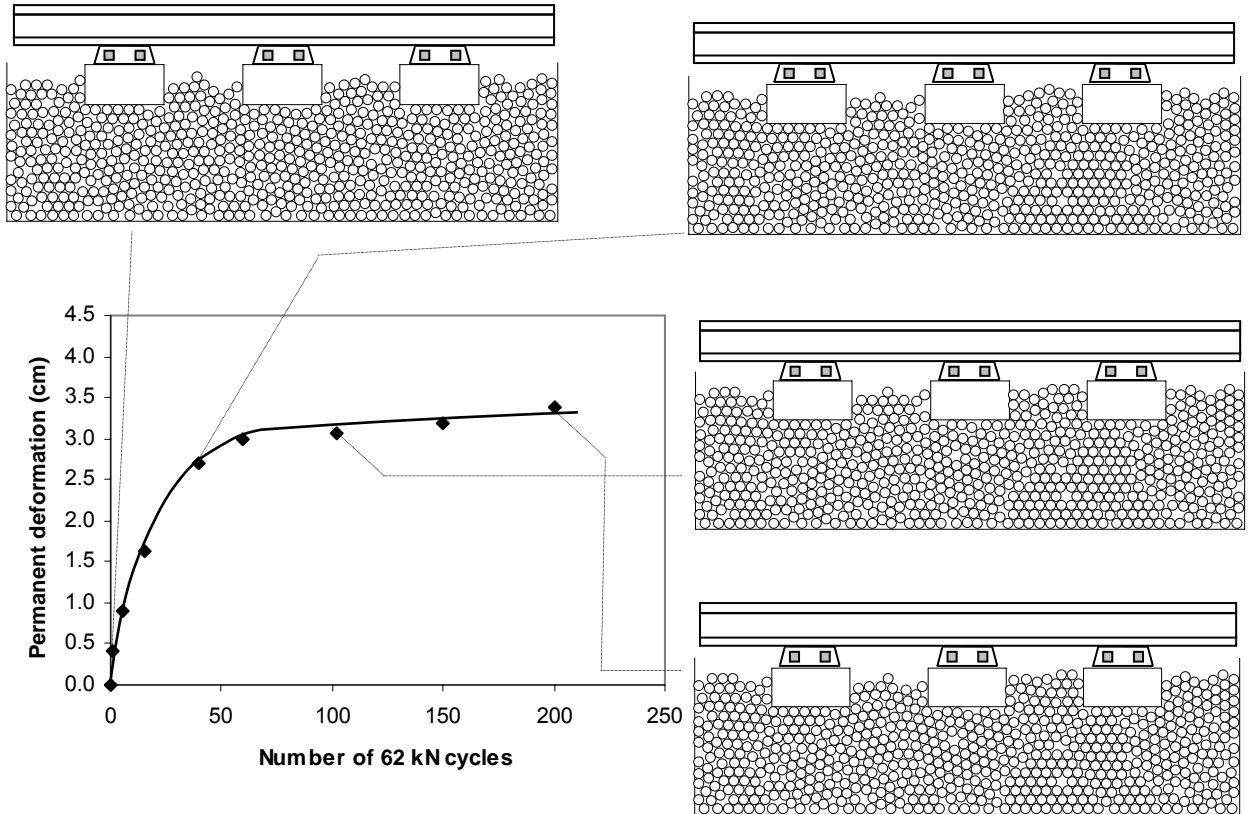


Figure 6.12. Permanent deformation of the ballast bed vs number of applied cycles, uncrushable ballast

Fig.6.13 shows the force chains that developed inside the ballast at two different stages of the simulation. As pointed out by Lim and McDowell [2005], the force chains are not uniformly distributed, and concentrate in those particles underneath the sleepers. Crushing could be expected to occur at these regions. On the other hand, it can be observed that the particles located on top of the ballast bed and between the sleepers do not take any load.

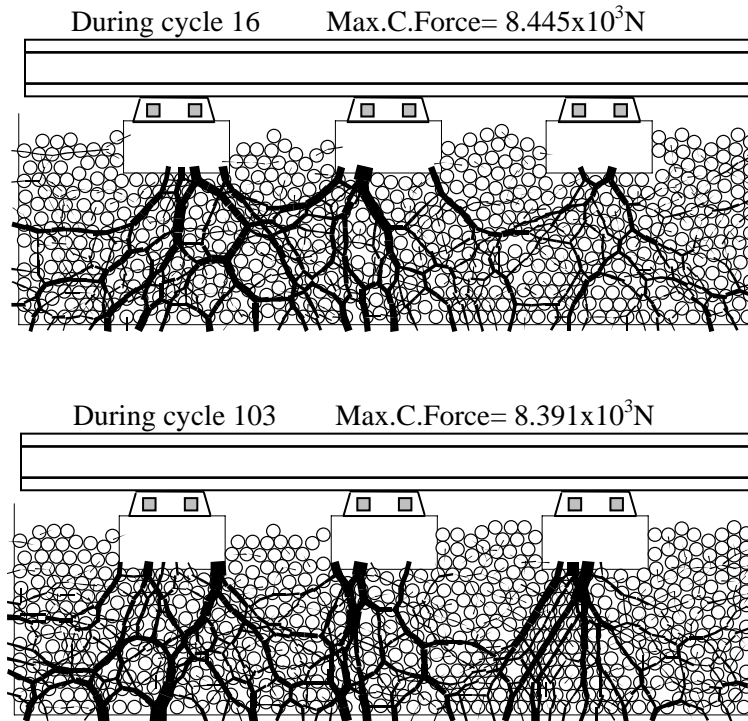


Figure 6.13. Development of force chains, uncrushable ballast

### 6.3.5 Results of the simulation considering crushing

Fig.6.14 shows the load cycles for the sample composed by crushable particles. The general trend is similar to the one observed for the case considering uncrushable particles: during the early cycles the permanent deformation rapidly increases but at the end of the test, the exhibited behavior is almost perfectly elastic. However, some of the first cycles present spike drops that were not observed during the first simulation. These spike drops correspond with the crushing of ballast particles. A sudden loss of stiffness was experienced by the sample when particle crushing took place. Nevertheless, the ballast material was always able to rearrange and regain its stiffness.

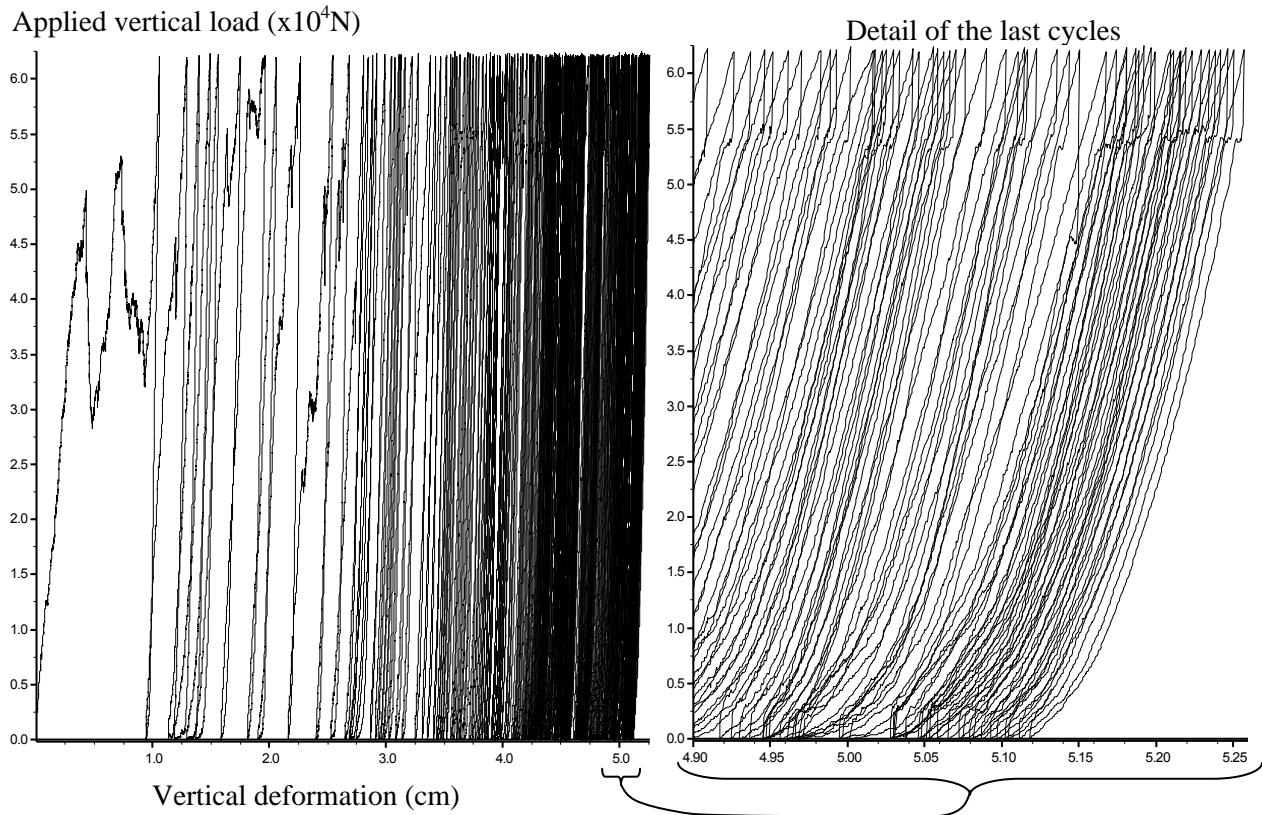


Figure 6.14. Load cycles, crushable ballast

Fig.6.15 shows the induced permanent deformation as a function of the load cycles. It can be observed that a permanent deformation of 5.12cm was measured at the end of the 200 cycles. This value is considerably higher than the one measured for the simulation with unbreakable particles. Fig.6.15 also shows some snap shots of the sample at different moments of the simulation. The original particles are shown as white particles, the particles produced as a result of crushing of the original particles are shown as light grey particles (first generation of crushing), the fragments coming from these fragments are shown as dark grey particles(second generation of crushing), and finally the fragments produced from the breaking of these second generation fragments are shown as black particles (third generation of crushing). No more than a third generation of crushing was found inside the sample at the end of the simulation even though the adopted failure criterion did not have a breakage size limit.

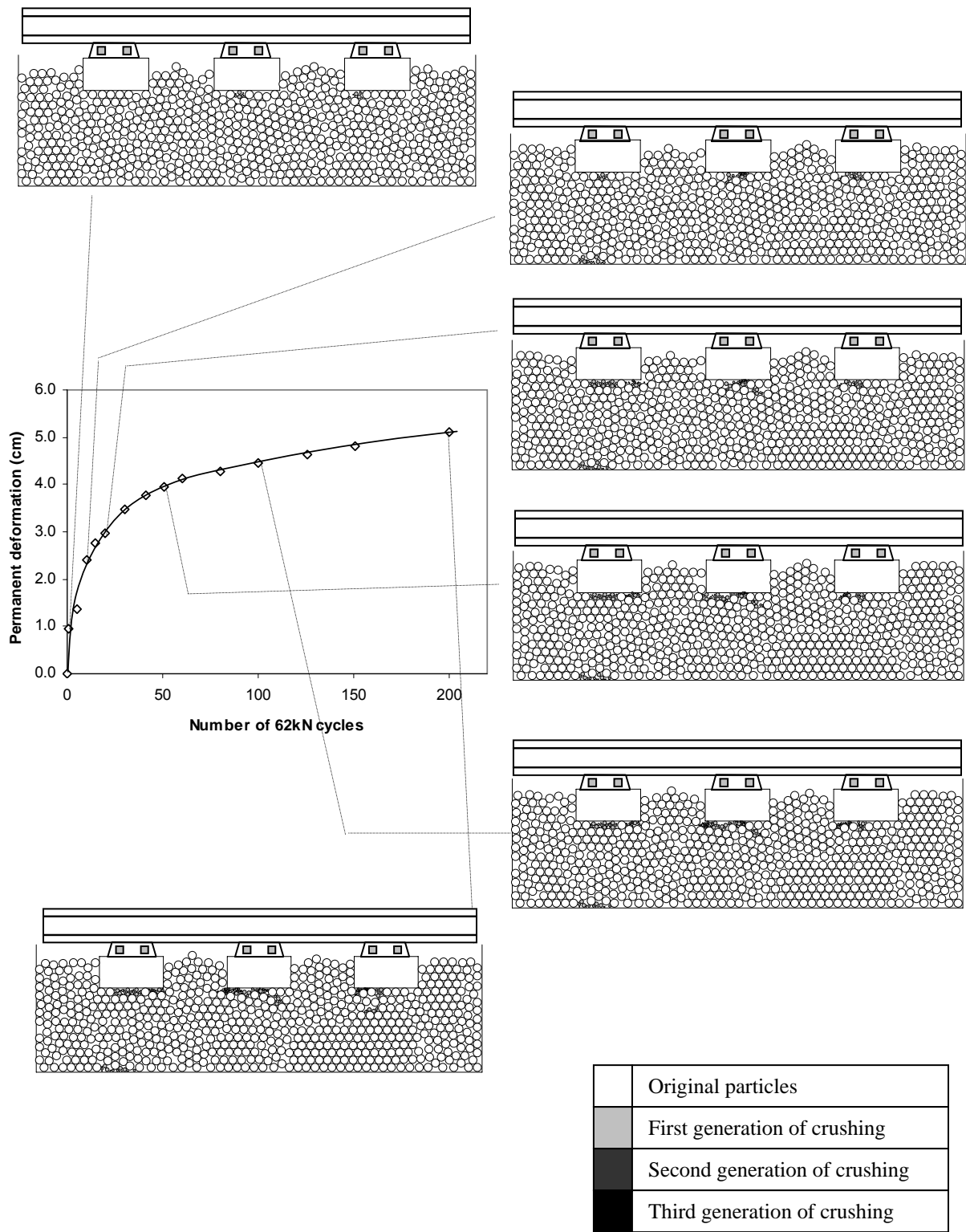


Figure 6.15 Permanent deformation of the ballast bed vs. number of applied cycles, crushable ballast

The snap shots on Fig.6.15 show that crushing took place mostly during the initial cycles. Moreover, it concentrated underneath the sleepers. A striking feature of Fig.6.15 is that even though the permanent deformation was considerably higher than for the uncrushable case (5.12cm vs. 3.38cm), only a few particles were crushed. Fig.6.16 shows amplified details of the unloaded sample after the completion of the 200 cycles. It can be observed how the different generations of crushing interacted with each other. The significant permanent deformation observed in Fig.6.15 was the product of the rearrangement between the unbroken particles and the fragments produced as a result of crushing.

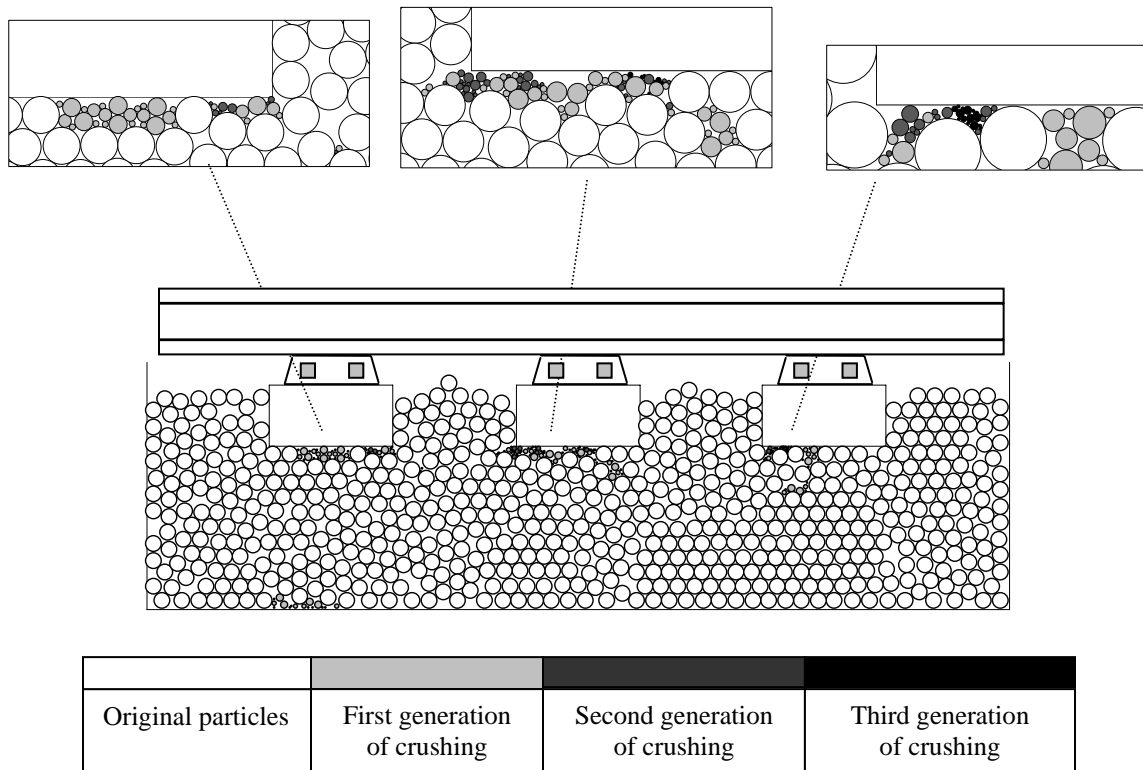


Figure 6.16 Details of the unloaded sample after 200 cycles, crushable ballast

### 6.3.6 Discussion of the results

The numerical simulations presented before have many idealizations such as considering dry circular ballast particles and considering only one magnitude for the applied cyclic load. It is well known that rounded particles are not the best possible ballast, and should be avoided when possible [Raymond, 2000]. Moreover, real traffic loads have different magnitudes. Nevertheless, the obtained results can be used to analyze the effects of crushing. Crushing concentrates directly underneath the sleepers, and produces an important increment on permanent deformation even though only a few particles are crushed. Moreover, the fragments produced as a result of crushing continue to break until they form a structure that is able to withstand the induced loads. It is expected that the ballast material will present a reduction of hydraulic conductivity since the unbroken particles and the produced fragments rearrange forming a dense structure. Thus, detrimental effects are associated with the occurrence of crushing.

The results from the first simulation showed that permanent deformation takes place even in the absence of crushing. As shown on Fig.6.12, the sample experienced particle rearrangement and an important increment on permanent deformation during the first 60 cycles. This permanent deformation could be avoided by providing a better seating of the sleepers. Rather than inducing a high static vertical stress, dynamic compaction could be used to induce as much cycles as possible to prevent future permanent deformation.

The obtained results can be used to highlight the importance of using standard tests that include the features observed during the simulations. As pointed out by McDowell et al. [2003], is important to consider the fact that the material at the track is constrained of movement and can not freely move as it does inside a drum. Since the strength of the ballast particles is a function of size, is important to test particles that are actually used as ballast. Moreover, the conditions at the track are dynamic conditions and could be more critical than static conditions since they promote particle rearrangement. Finally, is important to perform complete petrographic analyses before selecting a ballast material. These analyses allow to identify the occurrence of planes of weakness such as foliation and cleavage, and provide

important information regarding physical and chemical properties of the material that could be related to the possibility of ballast degradation.

## **6.4 DEGRADATION OF A GRANULAR BASE UNDER A FLEXIBLE PAVEMENT**

A typical flexible pavement is composed by an asphalt concrete layer (sometimes referred as the asphalt layer), a granular base layer, a granular subbase layer, and a natural subgrade. The granular materials forming part of the granular layers are subjected to static and dynamic loads during their engineering life. As a result of these loads particle crushing may occur depending on the strength of the particles. Changes on the grain size distribution of a granular material as a result of crushing are associated with negative effects such as a reduction of hydraulic conductivity and settlements. The results of a DEM simulation are presented in order to provide a visualization of the evolution of crushing in a simulated granular base layer forming part of a simulated pavement structure. This simulation provides a possible explanation about how, when, and where particle crushing is expected to occur.

It must be noted that particle crushing may only take place under unfavorable circumstances such as having a weak granular material as a granular layer or having exceptionally high traffic loads. Moreover, environmental effects such as weathering can contribute to reduce the resistance to degradation of the base material. Therefore, the results presented in this section can be used to understand the behavior of only certain pavements where particle crushing is expected to occur.

### **6.4.1 Typical structure of a flexible pavement**

Most Flexible pavements consist of a granular base on top of a compacted subgrade, with an asphalt concrete layer placed on top of the granular base. The combination of the asphalt layer and

granular layer provides a structural bond which makes it capable of withstanding repeated loads such as those that occur from vehicular traffic. A geotextile fabric or a subbase layer are sometimes used on top of the existing subgrade for additional strength. The granular layers in a pavement structure serve different purposes: (a) to provide the structural strength, (b) to drain out the water that enters to the pavement structure, and (c) to safely reduce the total cost of the pavement structure. The gradation of the granular base is typically well-graded so that good compaction can be obtained minimizing the content of voids. However, the fines content should be controlled so the pavement structure will still be able to provide adequate drainage. Detrimental consequences are associated with inadequate drainage such as excessive deformations due to a reduction on the strength of the materials forming the pavement, and stripping of the asphalt binder.

#### 6.4.2 Simulating a pavement section

Although DEM has been extensively used to simulate the behavior of granular materials such as those used in a granular base layer, there have been only a few studies reporting the use of DEM to simulate the behavior of an asphalt material. Pioneering studies reported by Chang and Meegoda [1997], Buttlar and You [2001], and Collop et al. [2004] have shown that DEM can be satisfactorily used to simulate the behavior of an asphalt mixture. However, the previous research has only focus on simulating the behavior of small specimens and not the complete layer used in a pavement structure. The author is not aware of any research study intended to simulate the combined behavior of the complete pavement structure using DEM.

Simulating the behavior of the asphalt concrete layer and the base layer is a complicated task and requires the adoption of some assumptions. The first assumption was to consider a two dimensional section of the pavement. This two dimensional section of study had a length equal to 30cm, and a height that included the asphalt layer, and the top 13cm of the granular base layer. This section of study was subjected to several applications of a loaded wheel that induced a constant vertical force equal to 75 kN

while traveling at a speed of  $1 \times 10^{-5}$  m/step. The radius of the wheel was equal to 3cm, its density was equal to  $2500 \text{ kg/m}^3$ , its normal and shear stiffness were equal to  $1 \times 10^8 \text{ N/m}$ , and its friction coefficient was equal to 0.7. This rolling wheel was applied from the left of the study section to the right, and when it was approaching the right boundary it was automatically deleted and generated again at the starting left point. This was automatically controlled by a subroutine programmed using the FISH language.

The asphalt concrete layer was modeled as a continuum bonding 446 discs in 9 rows. Each particle (with the exception of those located at the boundaries) had six neighbors. The radius of the discs was equal to 3mm. The value of the maximum force resisted by each bond was selected such as no breakage of the bonds was observed during the simulation. The density of the disks was equal to  $2500 \text{ kg/m}^3$ , and their coefficients of normal and shear stiffness were equal to  $1 \times 10^8 \text{ N/m}$ . The base layer was modeled with 1000 unbounded discs having a radius of 3mm and a friction coefficient of 0.7. Their density and coefficients of normal and shear stiffness were similar to those used for the bonded discs forming the asphalt layer. Crushing was allowed to occur only in the base layer.

The intention of the author was to develop a simple simulation that allowed a visualization of the general features during the evolution of crushing at the base layer rather than produce a complex model able to consider all the variables involved that may not have a significant effect on the final outcome. Moreover, the simulated model only applies to those pavements where crushing is expected to occur as a result of unfavorable conditions (weak materials, weathering, high loads).

#### 6.4.3 Simulating the construction process and the application of the moving wheel

The construction process was simulated by generating the base material, inducing compaction, and placing the asphalt layer. First, the base material was generated inside the studied section and was allowed to settle under the action of a gravity field ( $g = 9.8 \text{ m/s}^2$ ). After this, a horizontal rigid wall was temporarily created on top of the material in order to compact the base layer and produce a flat surface. This wall moved vertically at a slow velocity of  $1 \times 10^{-7}$  m/step, loading the base layer until three particles

broke down. Then, the wall was moved upward at the same velocity until it separated from the top of the base layer. After this, the temporary wall was deleted. The asphalt concrete layer was generated on top of the granular base, and after being placed, the simulated wheel completed one pass over the finished surface. This first pass only applied a vertical force of 30kN and it was not counted as one of the load applications.

The pavement section was subjected to 17 passes of the 75kN loaded wheel. It was stopped at that point since severe granular crushing developed at the base layer and significant plastic deformations were transmitted to the surface of the asphalt layer.

#### 6.4.4 Results of the simulation

Fig.6.17 shows typical examples of how the asphalt concrete layer and the base layer distributed the forces induced by the moving wheel. Fig.6.17.a shows the stressed zones developed inside the asphalt concrete layer. The contact bonds between the particles forming the asphalt layer were not plotted in this figure to allow a better visualization of the forces developed inside the layer. Very high compressive forces developed at the contact with the wheel while tensile forces developed at the bottom of the asphalt layer. Other tensile forces concentrated at the top of the asphalt layer at some horizontal distance from the wheel. As the wheel continued its movement, new zones developed compressive or tensile forces. This behavior is similar to the one observed on real flexible pavements.

Fig.6.17.b shows a typical example of how the forces transmitted by the asphalt concrete layer to the base material were spread through force chains. It can be noted that some particles did not transmit any load while other particles concentrated very high forces. However, as the wheel continued to roll these chains moved and some of the idle particles became loaded particles.

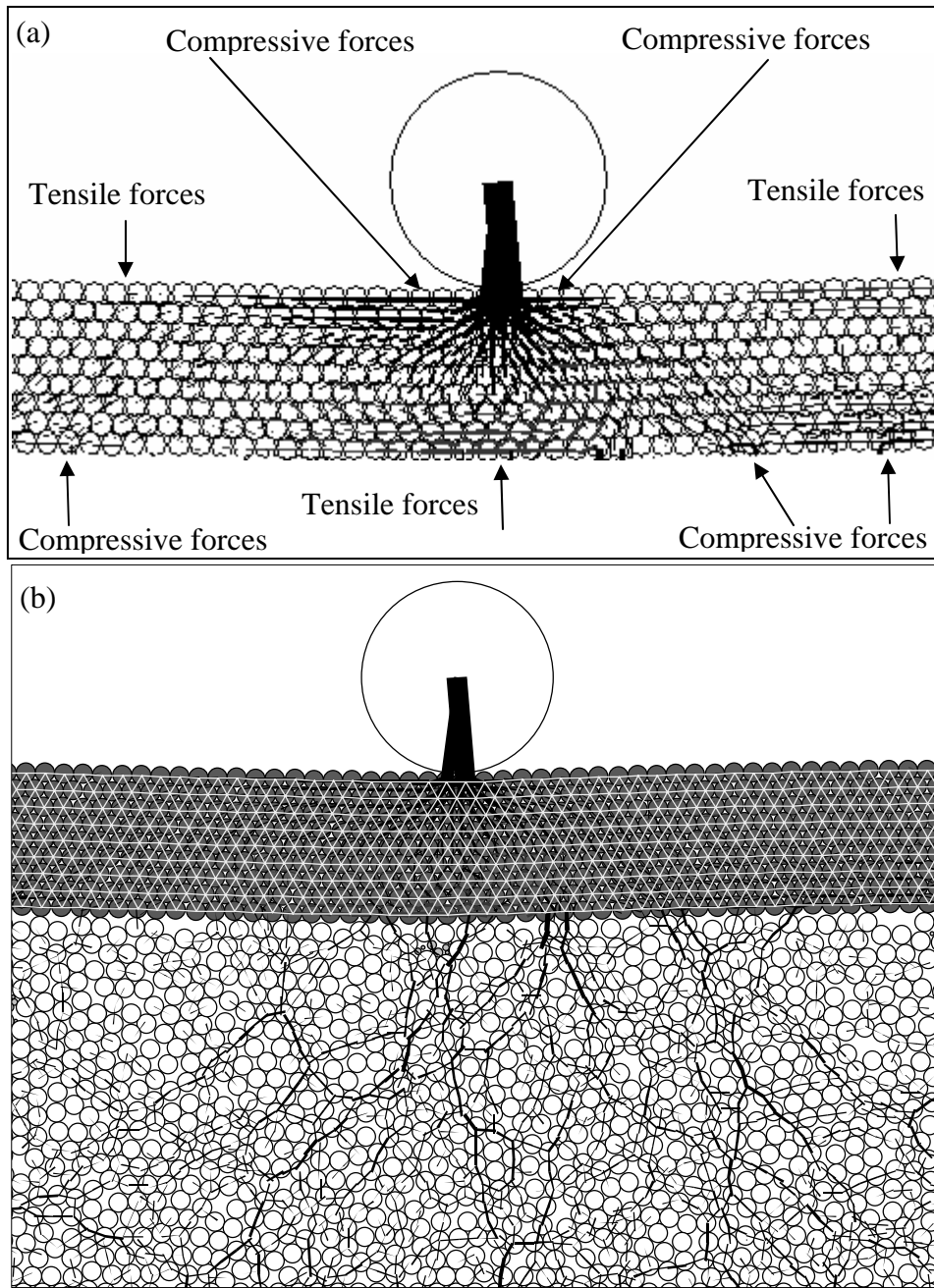


Figure 6.17 Forces developed inside the asphalt concrete layer and the granular base layer

Fig.6.18 shows the studied section of the pavement after different number of completed passes,  $N$ , of the rolling wheel. Fig.6.19 shows amplified details of the base layer at  $N=16$ . A significant amount of crushing took place during the first 5 passes while only a moderate amount of crushing took place between  $N=5$  and  $N=11$ . Moreover, only a very small amount of crushing occurred between  $N=11$  and  $N=16$ . This can be explained because after some crushing took place the unbroken particles reorganized with each other and the produced fragments forming a denser structure. Particle crushing started to stop since the particles transmitting the main forces (located at the force chains) had higher coordination numbers and were protected against tensile stresses. The only negative effects of the increment in density are the reduction on hydraulic conductivity of the base layer and the irrecoverable deformation transmitted to the top of the asphalt concrete layer.

Crushing started and concentrated at the top of the base layer, but as the number of load applications increased, crushing started to spread down into the middle and bottom of the base layer. This trend can be explained because particles located at the interface had to transmit large values of force and were prone to be broken first. Even though the adopted breakage criterion did not restrict crushing of the already fragmented particles, no more than a second generation of crushing was observed during the simulation.

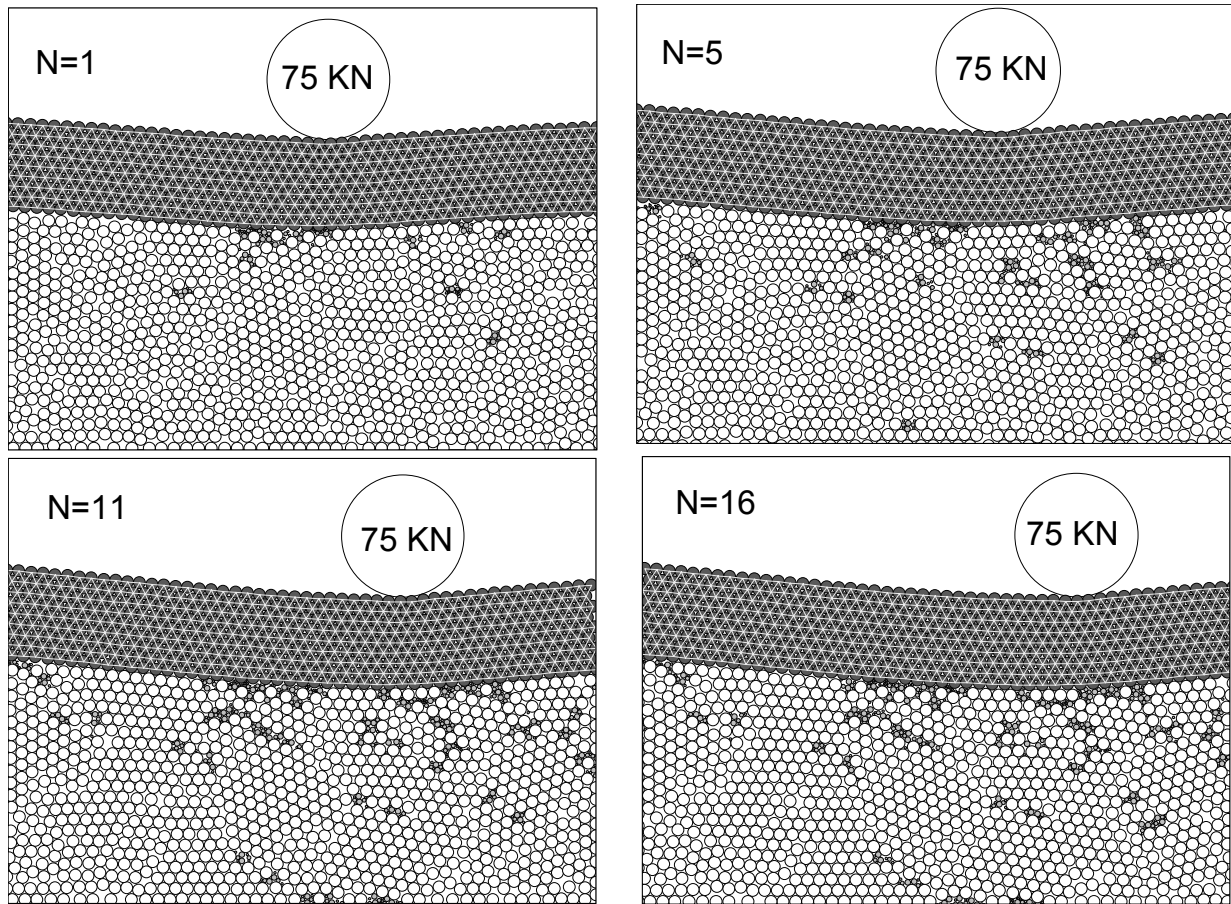


Figure 6.18 Snap shots of the pavement section being subjected to a different number of completed passes of a moving wheel

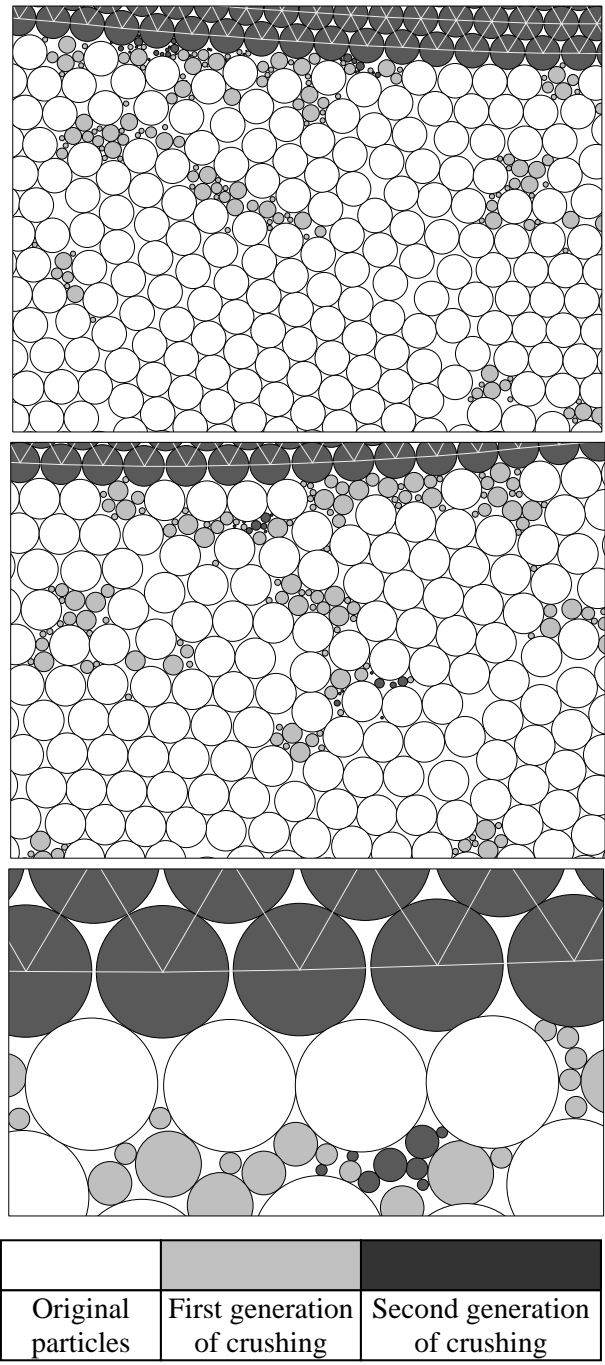


Figure 6.19 Details of the base layer at N=16

#### 6.4.5 Application of the findings and limitations of the DEM simulation

Based on the results from the DEM simulation it can be concluded that under unfavorable conditions particle crushing in the base layer is expected to occur during the first significant load applications. Crushing continues to occur at a decreasing rate, and starts to spread from the interface with the asphalt layer to the bottom of the base layer. Even though several properties such as elastic modulus are known to be improved with compaction, some detrimental effects such as reduction of hydraulic conductivity and the settlements produced at the top of the pavement structure will compromise the performance of the pavement. Special consideration should be given to the interface between the asphalt layer and the base layer in order to reduce the occurrence of crushing.

Even though the presented simulation provides a very useful visualization of the evolution of crushing in flexible pavements under unfavorable conditions, there are some limitations that need to be addressed prior to reach further conclusions. For example, the simulation did not consider the role of particle abrasion. Also, a uniform material was used in the base layer rather than a well graded material, and the asphalt layer was modeled in a very simple way without considering creep of the asphalt binder.

## 7.0 CONCLUSIONS

It was found that sugar is a weak granular material that can be used to study the evolution of crushing. This material breaks under low values of stress, allowing the use of standard laboratory tests. Based on the results of the laboratory tests conducted on this material and the results of previous research, it can be concluded that particle crushing is a detrimental phenomenon that causes settlements, and produces a reduction on the hydraulic conductivity and the peak shear strength of the material. However, it was found that the residual shear strength is not affected by the occurrence of crushing. The grain size distribution of the original material evolved towards a fractal distribution as a result of crushing during all the laboratory tests. The fractal distribution at the end of each test was found to depend on the conditions of stress and strain experienced by the samples.

Even though DEM does not normally consider particle breakage, it was possible to simulate crushing by replacing the particles that failed in tension with a combination of many particles of different sizes. In this way, by using a simplified failure criterion developed by the author, DEM was used to visualize and understand the evolution of granular crushing. This enhanced DEM was used to simulate the laboratory tests conducted on the sugar samples. The obtained results were in agreement with those from the experimental tests. Moreover, they allowed a visualization of the crushing evolution under different combinations of stress and strain.

The developed breakage model was used to study the evolution of crushing on practical geotechnical applications: driven piles, footings, pavements, and railtrack structures. The obtained results showed the negative consequences produced by particle crushing, such as reduction of strength and excessive values of plastic deformation.

## BIBLIOGRAPHY

- 1 Ashby, M.F., Jones, R.H. (1998). *Engineering Materials 2: an Introduction to Microstructures, Processing and Design*, Butterworth-Heinemann, Oxford: pp.178-182.
- 2 Astrom, J.A., Herrmann, H.J. (1998). "Fragmentation of grains in a two-dimensional packing", *The European Physical Journal B*, 5, pp. 551-554.
- 3 Bardet, J.P., Proubet, J. (1991). "A numerical investigation of the structure of persistent shear bands in granular media", *Geotechnique*, 41(4), pp.599-613.
- 4 Billam, J. (1971). "Some aspects of the behaviour of granular materials at high pressures", *Stress-strain Behaviour of Soils: Proceedings of the Roscoe Memorial Symposium*, Cambridge University, pp. 69- 80.
- 5 Bishop, A.W. (1966). "The strength of soils as engineering materials", *Geotechnique*, 16, pp. 89-130.
- 6 Bolton, M.D. (1986). "The strength and dilatancy of sands", *Geotechnique*, 36(1), pp. 65-78.
- 7 Bolton, M.D., McDowell, G.R. (1997). "Clastic mechanics", *IUTAM Symposium on Mechanics of Granular and Porous Materials*, pp. 35-46.
- 8 Bolton, M.D, Cheng, Y.P. (2002). "Micro-geomechanics", *Proceedings of the Workshop on Constitutive and Centrifuge Modelling: Two extremes*, Monte Verita, Switzerland, pp. 59-71.
- 9 Boucher, D.L., Selig, E.T. (1987). "Application of petrographic analysis to ballast performance evaluation", *Transportation Research Record*, 1131, pp. 15-25.
- 10 Buttlar, W.G., You, Z. (2001). "Discrete element modeling of asphalt concrete", *Transportation Research Record*, 1757, Paper No.01-3454, pp. 111-118.
- 11 Byrne, B.W., Houlsby, G.T. (2001). "Observations of footing behaviour on loose carbonate sands", *Geotechnique*, 51(5), pp. 463-466.
- 12 Cassidy, M.J., Byrne, B.W., Houlsby, G.T. (2002). "Modelling the behaviour of circular footings under combined loading on loose carbonate sand", *Geotechnique*, 52(10), pp. 705-712.
- 13 Cassidy, M.J., Airey, D.W., Carter, J.P. (2005). "Numerical modeling of circular footings subjected to monotonic inclined loading on uncemented and cemented calcareous sands", *ASCE Journal of Geotechnical and Geoenvironmental Engineering*, 131(1), pp. 52-63.

- 14 Chang, K.N.G., Meegoda, J.N. (1997). "Micromechanical simulation of hot mix asphalt", *Journal of Engineering Mechanics*, 123(5), pp. 495-503.
- 15 Chavez, C., Alonso, E.E. (2003). "A constitutive model for crushed granular aggregates which includes suction effects", *Soils and Foundations*, 43(4), pp. 215-227.
- 16 Cheng, Y.P., Nakata, Y., Bolton, M.D. (2003). "Discrete element simulation of crushable soil", *Geotechnique*, 53(7), pp. 633-641.
- 17 Collop, A.C., McDowell, G.R., Lee, Y. (2004). "Use of the distinct element method to model the deformation behavior of an idealized asphalt mixture", *The International Journal of Pavement Engineering*, 5(1), pp. 1-7.
- 18 Coop, M.R. (1990). "The mechanics of uncemented carbonate sands", *Geotechnique*, 40(4), pp. 607-626.
- 19 Coop, M.R., Sorensen, K.K., Bodas Freitas, T., Georgoutsos, G. (2004). "Particle breakage during shearing of a carbonate sand", *Geotechnique*, 54(3), pp.157-163.
- 20 Corriveau, D., Savage, S.B., Oger, L. (1997). "Internal friction angles: characterization using biaxial test simulations", *IUTAM Symposium on Mechanics of Granular and Porous Materials*, pp. 313-324.
- 21 CP Rail Specification for Ballast. (1987). *Appendix of the Transportation Research Record*, 1131, pp. 59-63.
- 22 Cundall, P.A., Strack, O.D.L. (1979). "A discrete numerical model for granular assemblies", *Geotechnique*, 29(1), pp. 47-65.
- 23 Das, B.M. (1999). "*Principles of foundation engineering*", fourth edition, PWS publishing: ITP, pp. 152-172.
- 24 Fedaa, J.(2002). "Notes on the effect of grain crushing on the granular soil behavior", *Engineering Geology*, 63, pp.93-98.
- 25 Gilchrist, J.M. (1985). "Load tests on tubular piles in coralline strata", *ASCE Journal of Geotechnical Engineering*, 111(5), pp. 641-655.
- 26 Gui, M.W. (1995). "Centrifuge and numerical modelling of pile and penetrometer in sand", PhD dissertation, University of Cambridge.
- 27 Hagerty, M.M., Hite, D.R., Ullrich, C.R., Hagerty, D.J. (1993). "One dimensional high pressure compression of granular media", *ASCE Journal of Geotechnical Engineering*, 119(1), pp.1-18.
- 28 Hagiwara, T., Ohuchi, M., Kusakabe, O., Maeda, Y. (1997). "Observations of shear bands in natural deposits", *Deformation and Progressive Failure in Geomechanics (IS-NAGOYA'97)*, pp. 473-478
- 29 Hardin, B.O. (1985). "Crushing of soil particles", *ASCE Journal of Geotechnical Engineering*, 111(10), pp. 1177-1192.

- 30 Harireche, O., McDowell, G.R. (2003). "Discrete element modelling of cyclic loading of crushable aggregates", *Granular Matter*, 5, pp. 147-151.
- 31 Indraratna, B., Ionescu, D., Christie, H.D. (1998). "Shear behavior of railway ballast based on large-scale triaxial tests", *ASCE Journal of Geotechnical and Geoenvironmental Engineering*, 124(5), pp. 439-449.
- 32 Itasca Consulting Group, Inc. (2002). *PFC<sup>2D</sup> (Particle Flow Code in Two Dimensions) version 3.0: Theory and Background*.
- 33 Itasca Consulting Group, Inc. (2002). *PFC<sup>2D</sup> (Particle Flow Code in Two Dimensions) version 3.0: FISH in PFC*.
- 34 Itasca Consulting Group, Inc. (2002). *PFC<sup>2D</sup> (Particle Flow Code in Two Dimensions) version 3.0: User's Guide*.
- 35 Iwashita, K., Oda, M. (1998). "Rolling resistance at contacts in simulation of shear band development by DEM", *ASCE Journal of Engineering Mechanics*, 124(3), pp. 285-292.
- 36 Jensen, R.P., Bosscher, P.J., Plesha, M.E., Edil, T.B. (1999). "DEM simulation of granular media – structure interface: effects of surface roughness and particle shape", *International Journal for Numerical and Analytical Methods in Geomechanics*, 23, pp. 531-547.
- 37 Jensen, R.P., Plesha, M.E., Edil, T.B., Bosscher, P.J., Kahla, N.B. (2001). "DEM simulation of particle damage in granular media – structure interfaces", *The International Journal of Geomechanics*, 1(1), pp. 21-39.
- 38 Klassen, M.J., Clifton, A.W., Watters, B.R. (1987). "Track evaluation and ballast performance specifications", *Transportation Research Record*, 1131, pp. 35-44.
- 39 Klotz, E.U., Coop, M.R. (2001). "An investigation of the effect of soil state on the capacity of driven piles in sands", *Geotechnique*, 51(9), pp. 733-751.
- 40 Kusakabe, O., Maeda, Y., Ohuchi, M. (1992). "Large-scale loading tests of shallow footings in pneumatic caisson", *ASCE Journal of Geotechnical Engineering*, 118(11), pp. 1681-1695.
- 41 Lade, P.V., Yamamuro, J.A., Bopp, P.A. (1996). "Significance of particle crushing in granular materials", *ASCE Journal of Geotechnical Engineering*, 122(4), pp. 309-316.
- 42 Lang, R.A. (2002). *Numerical simulation of comminution in granular materials with an application to fault gouge evolution*, unpublished Master of Science Thesis, Texas A&M University, pp. 1-62.
- 43 Lee, K.L., Farhoomand, I. (1967). "Compressibility and crushing of granular soil in anisotropic triaxial compression", *Canadian Geotechnical Journal*, 4(1), pp. 68-86.
- 44 Lee, S.Y. (1990). "Centrifuge modelling of cone penetration testing in cohesionless soils", PhD dissertation, University of Cambridge.
- 45 Leung, C.F., Lee, F.H., Yet, N.S. (1996). "The role of particle breakage in pile creep in sand", *Canadian Geotechnical Journal*, 33, pp. 888-898.

- 46 Lim, W.L., McDowell, G.R., Collop, A.C. (2004). "The application of Weibull statistics to the strength of railway ballast", *Granular Matter*, 6, pp. 229-237.
- 47 Lim, W.L., McDowell, G.R. (2005). "Discrete element modelling of railway ballast", *Granular Matter*, 7, pp.19-29.
- 48 Lin, X., Ng, T.T. (1997). "A three-dimensional discrete element model using arrays of ellipsoids", *Geotechnique*, 47(2), pp. 319-329.
- 49 Luzzani, L., Coop, M.R. (2002). "On the relationship between particle breakage and the critical state of sands", *Soils and Foundations*, 42(2), pp. 71-82.
- 50 Mandl, G., Jong, L.N.J., Maltha, A. (1977). "Shear zones in granular material", *Rock Mechanics*, 9, pp. 95-144.
- 51 McDowell, G.R., Bolton, M.D., Robertson, D. (1996). "The fractal crushing of granular materials", *Journal of the Mechanics and Physics of Solids*, 44(12), pp. 2079-2102.
- 52 McDowell, G.R., Bolton, M.D. (1998). "On the micromechanics of crushable aggregates", *Geotechnique*, 48(5), pp. 667-679.
- 53 McDowell, G.R., Amon, A. (2000). "The application of Weibull statistics to the fracture of soil particles", *Soils and Foundations*, 40(5), pp.133-141.
- 54 McDowell, G.R., Bolton, M.D. (2000). "Effect of particle size distribution on pile tip resistance in calcareous sand in the geotechnical centrifuge", *Granular Matter*, 2, pp.179-187.
- 55 McDowell, G.R. (2001). "Statistics of soil particle strength", *Geotechnique*, 51(10), pp. 897-900.
- 56 McDowell, G.R., Daniell, C.M. (2001). "Fractal compression of soil", *Geotechnique*, 51(2), pp. 173-176.
- 57 McDowell, G.R. (2002). "On the yielding and plastic compression of sand", *Soils and Foundations*, 42(1), pp. 139-145.
- 58 McDowell, G.R., Harireche, O. (2002). "Discrete element modelling of yielding and normal compression of sand", *Geotechnique*, 52(4), pp. 299-304.
- 59 McDowell, G.R., Humphreys, A. (2002). "Yielding of granular materials", *Granular Matter*, 4, pp.1-8.
- 60 McDowell, G.R., Khan, J.J. (2003). "Creep of granular materials", *Granular Matter*, 5, pp. 115-120.
- 61 McDowell, G.R., Lim, W.L., Collop, A.C. (2003). "Measuring the strength of railway ballast", *Ground Engineering*, 36(1), pp. 25-28.
- 62 Miura, N., Yamanouchi, T. (1975). "Effect of water on the behavior of a quartz-rich sand under high stresses", *Soils and Foundations*, 15(4), pp. 23-34.

- 63 Miura, N., O-Hara, S. (1979). "Particle-crushing of a decomposed granite soil under shear stresses", *Soils and Foundations*, 19(3), pp. 1-14.
- 64 Miyake, M., Kusakabe, O. (1997). "Shear band observed in loading tests", *Deformation and Progressive Failure in Geomechanics (IS-NAGOYA '97)*, pp. 887-898.
- 65 Mora, P., Place, D. (1994). "Simulation of the frictional stick-slip instability", *Pure and Applied Geophysics*, 143(1/2/3), pp. 61-87.
- 66 Morgan, J.K., Boettcher, M.S. (1999). "Numerical simulations of granular shear zones using the distinct element method; 1. Shear zone kinematics and the micromechanics of localization", *Journal of Geophysical Research*, 104(No.B2), pp. 2703-2719.
- 67 Morgan, J.K. (1999). "Numerical simulations of granular shear zones using the distinct element method; 2. Effects of particle size distribution and interparticle friction on mechanical behavior", *Journal of Geophysical Research*, 104(No.B2), pp.2721-2732.
- 68 Morgan, J.K. (2004). "Particle dynamics simulations of rate-and state-dependent frictional sliding of granular fault gouge", *Pure and Applied Geophysics*, 161, pp.1877-1891.
- 69 Murff, J.D. (1987). "Pile capacity in calcareous sands: state of the art", *ASCE Journal of Geotechnical Engineering*, 113(5), pp. 490-507.
- 70 Nakata, Y., Hyde, A.F.L., Hyodo, M., Murata, H. (1999). "A probabilistic approach to sand particle crushing in the triaxial test", *Geotechnique*, 49(5), pp.567-583.
- 71 Nakata, Y., Hyodo, M., Hyde, A.F.L., Kato, Y., Murata, H. (2001a). "Microscopic particle crushing of sand subjected to high pressure one-dimensional compression", *Soils and Foundations*, 41(1), pp.69-82.
- 72 Nakata, Y., Kato, Y., Hyodo, M., Hyde, A.F.L., Murata, H. (2001b). "One-dimensional compression behaviour of uniformly graded sand related to single particle crushing strength", *Soils and Foundations*, 41(2), pp. 39-51.
- 73 Oda, M., Iwashita, K., Kazama, H. (1997). "Micro-structure developed in shear bands of dense granular soils and its computer simulation – mechanism of dilatancy and failure-. *IUTAM Symposium on Mechanics of Granular and Porous Materials*, pp. 353-364.
- 74 Oda, M., Kazama, H. (1998). "Microstructure of shear bands and its relation to the mechanisms of dilatancy and failure of dense granular soils", *Geotechnique*, 48(4), pp. 465-481.
- 75 Pestana, J.M., Whittle, A.J. (1995). "Compression model for cohesionless soils", *Geotechnique*, 45(4), pp. 611-631.
- 76 Place, D., Mora, P. (2000). "Numerical simulation of localisation phenomena in a fault zone", *Pure and Applied Geophysics*, 157, pp. 1821-1845.
- 77 Randolph, M.F. (2003). "Science and empiricism in pile foundation design", *Geotechnique*, 53(10), pp. 847-875.

- 78 Raymond, G.P., Bathurst, R.J. (1987). "Performance of large-scale model single tie-ballast systems", *Transportation Research Record*, 1131, pp.7-14.
- 79 Raymond, G.P. (2000). "Track and support rehabilitation for a mine company railroad", *Canadian Geotechnical Journal*, 37, pp. 318- 332.
- 80 Sammis, C.G. (1997). "Fractal fragmentation and frictional stability in granular materials", *IUTAM Symposium on Mechanics of Granular and Porous Materials*, pp. 23-34.
- 81 Selig, E.T., Boucher, D.L. (1990). "Abrasion tests for railroad ballast", *Geotechnical Testing Journal*, 13(4), pp. 301-311.
- 82 Skinner, A.E. (1969). "A note on the influence of interparticle friction on the shearing strength of a random assembly of spherical particles", *Geotechnique*, 19(1), pp. 150-157.
- 83 Takei, M., Kusakabe, O., Hayashi, T. (2001). "Time-dependent behavior of crushable materials in one-dimensional compression tests", *Soils and Foundations*, 41(1), pp. 97-121.
- 84 Terzaghi, C., Peck, R. (1948). *Soil mechanics in engineering practice*, (New York: Ed Jhon Wiley & sons.), pp. 56-61.
- 85 Tsoungui, O., Vallet, D., Charmet, J.C. (1999). "Numerical model of crushing of grains inside two-dimensional granular materials", *Powder Technology*, 105, pp. 190-198.
- 86 Turcotte, D.L. (1986). "Fractals and fragmentation", *Journal of Geophysical Research*, 91(B2), pp. 1921-1926.
- 87 Tyler, S.W., Wheatcraft, S.W. (1992). "Fractal scaling of soil particle-size distribution analysis and limitations", *Soil Science Society of America Journal*, 56(2), pp.47-67.
- 88 Vallejo, L.E. (2003). "Crushing of granular bases: fractal and laboratory analyses", *Proceedings of the I Iberoamerican Symposium of Pavement Engineering / XIV Colombian Symposium of Pavement Engineering*, Popayan Colombia: June 11-14, CD-ROM.
- 89 White, D.J. Bolton, M.D. (2004). "Displacement and strain paths during plane-strain model pile installation in sand", *Geotechnique*, 54(6), pp.375-397.